Piezoelectric Energy Harvesting for Powering Wireless Monitoring Systems

Feng Qian

Dissertation submitted to the Faculty of the
Virginia Polytechnic Institute and State University
in partial fulfillment of the requirements for the degree of

Doctor of Philosophy
in
Mechanical Engineering

Lei Zuo, Chair
Muhammad R. Hajj
Robert G. Parker
Nicole T. Abaid

May 14, 2020
Blacksburg, Virginia

Keywords: Energy harvesting, Wireless monitoring, Piezoelectric, Human walking, Torsional vibration, Bio-inspired design, Bi-stable nonlinear vibration

Piezoelectric Energy Harvesting for Powering Wireless Monitoring Systems

Feng Qian

ABSTRACT

The urgent need for a clean and sustainable power supply for wireless sensor nodes and low-power electronics in various monitoring systems and the Internet of Things has led to an explosion of research in substitute energy technologies. Traditional batteries are still the most widely used power source for these applications currently but have been blamed for chemical pollution, high maintenance cost, bulky volume, and limited energy capacity. Ambient energy in different forms such as vibration, movement, heat, wind, and waves otherwise wasted can be converted into usable electricity using proper transduction mechanisms to power sensors and low-power devices or charge rechargeable batteries. This dissertation focuses on the design, modeling, optimization, prototype, and testing of novel piezoelectric energy harvesters for extracting energy from human walking, bio-inspired bi-stable motion, and torsional vibration as an alternative power supply for wireless monitoring systems.

To provide a sustainable power supply for health care monitoring systems, a piezoelectric footwear harvester is developed and embedded inside a shoe heel for scavenging energy from human walking. The harvester comprises of multiple 33-mode piezoelectric stacks within single-stage force amplification frames sandwiched between two heel-shaped aluminum plates taking and reallocating the dynamic force at the heel. The single-stage force amplification frame is designed and optimized to transmit, redirect, and amplify the heel-strike force to the inner piezoelectric stack. An analytical model is developed and validated to predict precisely the electromechanical coupling behavior of the harvester. A symmetric finite element model

is established to facilitate the mesh of the transducer unit based on a material equivalent model that simplifies the multilayered piezoelectric stack into a bulk. The symmetric FE model is experimentally validated and used for parametric analysis of the single-stage force amplification frame for a large force amplification factor and power output. The results show that an average power output of 9.3 mW/shoe and a peak power output of 84.8 mW are experimentally achieved at the walking speed of 3.0 mph (4.8 km/h). To further improve the power output, a two-stage force amplification compliant mechanism is designed and incorporated into the footwear energy harvester, which could amplify the dynamic force at the heel twice before applied to the inner piezoelectric stacks. An average power of 34.3 mW and a peak power of 110.2 mW were obtained under the dynamic force with the amplitude of 500 N and frequency of 3 Hz. A comparison study demonstrated that the proposed two-stage piezoelectric harvester has a much larger power output than the state-of-the-art results in the literature.

A novel bi-stable piezoelectric energy harvester inspired by the rapid shape transition of the Venus flytrap leaves is proposed, modeled and experimentally tested for the purpose of energy harvesting from broadband frequency vibrations. The harvester consists of a piezoelectric macro fiber composite (MFC) transducer, a tip mass, and two sub-beams with bending and twisting deformations created by in-plane pre-displacement constraints using rigid tip-mass blocks. Different from traditional ways to realize bi-stability using nonlinear magnetic forces or residual stress in laminate composites, the proposed bio-inspired bi-stable piezoelectric energy harvester takes advantage of the mutual self-constraint at the free ends of the two cantilever sub-beams with a pre-displacement. This mutual pre-displacement constraint bi-directionally curves the two sub-beams in two directions inducing higher mechanical potential energy. The nonlinear dynamics of the bio-inspired bi-stable piezoelectric energy harvester is investigated under sweeping frequency and harmonic excitations. The results show that the sub-beams of the harvester experience local vibrations, including broadband frequency

components during the snap-through, which is desirable for large power output. An average power output of 0.193 mW for a load resistance of 8.2 kΩ is harvested at the excitation frequency of 10 Hz and amplitude of 4.0 g.

Torsional vibration widely exists in mechanical engineering but has not yet been well exploited for energy harvesting to provide a sustainable power supply for structural health monitoring systems. A torsional vibration energy harvesting system comprised of a shaft and a shear mode piezoelectric transducer is developed in this dissertation to look into the feasibility of harvesting energy from oil drilling shaft for powering downhole sensors. A theoretical model of the torsional vibration piezoelectric energy harvester is derived and experimentally verified to be capable of characterizing the electromechanical coupling system and predicting the electrical responses. The position of the piezoelectric transducer on the surface of the shaft is parameterized by two variables that are optimized to maximize the power output. Approximate expressions of the voltage and power are derived by simplifying the theoretical model, which gives predictions in good agreement with analytical solutions. Based on the derived approximate expression, physical interpretations of the implicit relationship between the power output and the position parameters of the piezoelectric transducer are given.

Piezoelectric Energy Harvesting for Powering Wireless Monitoring Systems

Feng Qian

GENERAL AUDIENCE ABSTRACT

Wireless monitoring systems with embedded wireless sensor nodes have been widely applied in human health care, structural health monitoring, home security, environment assessment, and wild animal tracking. One distinctive advantage of wireless monitoring systems is to provide unremitting, wireless monitoring of interesting parameters, and data transmission for timely decision making. However, most of these systems are powered by traditional batteries with finite energy capacity, which need periodic replacement or recharge, resulting in high maintenance costs, interruption of service, and potential environmental pollution. On the other hand, abundant energy in different forms such as solar, wind, heat, and vibrations, diffusely exists in ambient environments surrounding wireless monitoring systems which would be otherwise wasted could be converted into usable electricity by proper energy transduction mechanisms.

Energy harvesting, also referred to as energy scavenging and energy conversion, is a technology that uses different energy transduction mechanisms, including electromagnetic, photovoltaic, piezoelectric, electrostatic, triboelectric, and thermoelectric, to convert ambient energy into electricity. Compared with traditional batteries, energy harvesting could provide a continuous and sustainable power supply or directly recharge storage devices like batteries and capacitors without interrupting operation. Among these energy transduction mechanisms, piezoelectric materials have been extensively explored for small-size and low-power generation due to their merits of easy shaping, high energy density, flexible design,

and low maintenance cost. Piezoelectric transducers convert mechanical energy induced by dynamic strain into electrical charges through the piezoelectric effect.

This dissertation presents novel piezoelectric energy harvesters, including design, modeling, prototyping, and experimental tests for energy harvesting from human walking, broadband bi-stable nonlinear vibrations, and torsional vibrations for powering wireless monitoring systems. A piezoelectric footwear energy harvester is developed and embedded inside a shoe heel for scavenging energy from heel striking during human walking to provide a power supply for wearable sensors embedded in health monitoring systems. The footwear energy harvester consists of multiple piezoelectric stacks, force amplifiers, and two heel-shaped metal plates taking dynamic forces at the heel. The force amplifiers are designed and optimized to redirect and amplify the dynamic force transferred from the heel-shaped plates and then applied to the inner piezoelectric stacks for large power output. An analytical model and a finite model were developed to simulate the electromechanical responses of the harvester. The footwear harvester was tested on a treadmill under different walking speeds to validate the numerical models and evaluate the energy generation performance. An average power output of 9.3 mW/shoe and a peak power output of 84.8 mW are experimentally achieved at the walking speed of 3.0 mph (4.8 km/h). A two-stage force amplifier is designed later to improve the power output further. The dynamic force at the heel is amplified twice by the two-stage force amplifiers before applied to the piezoelectric stacks. An average power output of 34.3 mW and a peak power output of 110.2 mW were obtained from the harvester with the two-stage force amplifiers.

A bio-inspired bi-stable piezoelectric energy harvester is designed, prototyped, and tested to harvest energy from broadband vibrations induced by animal motions and fluid flowing for the potential applications of self-powered fish telemetry tags and bird tags. The harvester consists of a piezoelectric macro fiber composite (MFC) transducer, a tip mass, and two sub-beams constrained at the free ends by in-plane pre-displacement, which bends and twists

the two sub-beams and consequently creates curvatures in both length and width directions. The bi-direction curvature design makes the cantilever beam have two stable states and one unstable state, which is inspired by the Venus flytrap that could rapidly change its leaves from the open state to the close state to trap agile insects. This rapid shape transition of the Venus flytrap, similar to the vibration of the harvester from one stable state to the other, is accompanied by a large energy release that could be harvested. Detailed design steps and principles are introduced, and a prototype is fabricated to demonstrate and validate the concept. The energy harvesting performance of the harvester is evaluated at different excitation levels.

Finally, a piezoelectric energy harvester is developed, analytically modeled, and validated for harvesting energy from the rotation of an oil drilling shaft to seek a continuous power supply for downhole sensors in oil drilling monitoring systems. The position of the piezoelectric transducer on the surface of the shaft is parameterized by two variables that are optimized to obtain the maximum power output. Approximate expressions of voltage and power of the torsional vibration piezoelectric energy harvester are derived from the theoretical model. The implicit relationship between the power output and the two position parameters of the transducer is revealed and physically interpreted based on the approximate power expression. Those findings offer a good reference for the practical design of the torsional vibration energy harvesting system.

Acknowledgments

I will forever be grateful to those who have helped and supported me in this endeavor. Without their support and encouragement, I wouldn't survive in this full of challenging journey and finish this dissertation.

I am particularly appreciative of my adviser, Professor Lei Zuo, for his generous support and guidance over the years. His enthusiasm and dedication to the research inspired me to work hard and finally decided to continue my career in academia. His vision and knowledge enhanced my capacity to formulate and solve the problem in my projects. He gave me the freedom to explore the areas I am interested in and never discouraged "naive" ideas I ever had. His attitude to work will also continue to affect my future life.

I thank my dissertation committee members, Professor Muhammad R. Hajj, Professor Robert G. Parker, and Professor Nicole T. Abaid, not only for their time and extreme patience in helping me but also for their intellectual contributions to my development as a researcher. Without the inspiration from their lectures, research, and achievements, I may not have ever pursued the challenging area of nonlinear dynamics, let alone writing papers and finishing this dissertation. Their comments, discussion, and feedback have been greatly helpful in improving the quality of this dissertation. I want to thank my former adviser, Professor Jianguo Wang, who initially led and guided me in the study of smart structures and vibrations. He is always helpful and supportive at every turning point in my life.

I also would like to thank our collaborators, Professor Tian-Bing Xu at Old Dominion University, Professor Haifeng Zhang at the University of North Texas, and Dr. Denial Deng at Pacific Northwest National Laboratory. I especially appreciate the support from all members of the Energy Harvesting and Mechatronics Research Laboratory and the NSF Center for Energy Harvesting Materials and Systems at Virginia Tech.

I am indebted too much to my families for their love and support. Not enough words could describe how thankful I am to my parents for their endless amounts of love, even if they never directly expressed that in words. Their diligence, kindness, and simplicity shaped my life attitude and are being undoubtedly passed on to the next generation. Thank them for working so hard to be able to send me to college for giving me the support that I needed to build a dream to chase after. Studying abroad and being apart from them have made me realize how much my parents mean to me. I felt terrible guilt towards my parents because I cannot be around them and repay their upbringing at the time that I should do. I deeply realize that they really want me to stay with them although they never said out this, especially after my father retired. I am also deeply grateful to my sister Liying Qian and my younger brother Chao Qian for their all the way support in materials and emotion.

My study at Virginia Tech would have been impossible without the devoted love and understanding from my wife, Dongjing Wang. She selflessly dedicates to take care of our family so that I could concentrate on my research. Finally, I would like to give my special thanks to my daughter Jiayi Qian and my son Michael Qian for the happiness and joy they have brought to my life.

Finally, I would like to thank the National Science Foundation grants #CMMI-152984, ECCS-1508862, ECCS-1935951, DOE grant DE-NE0008591, Virgninia Center for Innovative Technology (CIT) via National Institute of Aerospace #X16-9349-VT, and the AbbVie Inc for their generous funding for the research conducted in this dissertation.

Contents

List of Figures

List of Tables

Chapter 1

Introduction and Background

The growing worldwide demand and overexploitation for fossil energy and the consequent environmental impact are at the base of a very probable energy crisis in the near future, which has greatly motivated the exploration in renewable energy sources, such as vibrations, bio-energy, wind energy, and thermal energy, as the substitutions of traditional fossil fuel [1]. Various energy-generating techniques have been developed to convert these ubiquitously available ambient energy sources into usable electricity. Energy harvesting, also referred to as energy scavenging and energy conversion, uses different energy transduction mechanisms, including but not limited to electromagnetic [2, 3, 4, 5], piezoelectric [6, 7, 8], electrostatic [9], triboelectric [10], and thermoelectric [11], to capture, convert, and store the wasted energy into usable electricity to provide a sustainable power supply or recharge storage devices like batteries and capacitors. Since this technology could potentially avoid chemical waste and environmental pollution by replacing traditional batteries and gain monetary benefits by reducing maintenance cost, an explosion of academic research and industrial efforts have been devoted in this field. A review on the brief history of energy harvesting techniques, power conversion, power management, and battery charging could be found in [12].

Kinetic energy is ubiquitous typically presenting in the form of vibrations, random displacements, or forces that can be converted into electrical energy using electromagnetic, piezoelectric, or electrostatic mechanisms. Vibration energy harvesting has been extensively studied from micro-system level [13] to large scale level [14] for wireless sensor network applications, such as structural health monitoring. Comprehensive reviews on vibration energy harvesting principle, design, modeling, as well as applications in wireless sensor networks could be found in [15, 16, 17]. Vibration energy harvesting technology involves multidisciplinary scientific problems, including mechanics, advanced material science, electrical circuitry, and engineering design. The principle behind this technology is the realization of endless energy transmission from vibrational systems to transducers based on the electromechanical coupling effect of energy conversion materials. In vibration energy harvesting systems, the energy flowing out of the vibrating mechanical system is usually reflected by the added damping characterized by the externally connected electrical resistance in the modeling [18]. In other words, it is equivalent to provide a damping force or mechanical resistance for the vibrating mechanical systems as the embedded harvester extracts and converts the kinetic energy into electricity that is delivered to external electrical devices or storages. This is because the resistive loads of the powered devices dissipate the generated electrical energy extracted from the mechanical system. From this point of view, energy harvesting technology can also be integrated into vibration control systems, which consequently achieves both energy harvesting and vibration mitigation synchronously [19, 20, 21]. Taking the energy out of mechanical systems leads to a reduction in vibration. Therefore, energy harvesters that meanwhile plays the role of dynamics control are also referred as energy harvesting vibration absorbers [22, 23], energy harvesting damper [24], or energy harvesting sinker [25, 26].

1.1 Piezoelectric energy harvesting

Among various energy conversion mechanisms, piezoelectric materials are particularly favorable for small-size and low-power energy harvesting applications owing to their versatile features of easy shaping, high power density, flexible design, and low maintenance cost. Piezoelectric materials are the ideal transducers converting dynamic strain energy in mechanical components into electric charges as the response to the external excitations. This mechanical-to-electrical energy conversion ability is attributed to the direct piezoelectric effect, i.e., the electromechanical coupling phenomenon of piezoelectric materials, which creates electric charges under the applied dynamic stress. This unique mechanical-to-electrical energy conversion property enables piezoelectric transducers to be capable of harvesting energy from both base and dynamics force excitations. Piezoelectric materials can work in different modes based on the polarization direction and applied load direction, which are characterized by the piezoelectric constant d_{ij}, where the subscripts i and j denote the polarization direction and the applied force direction, respectively [27]. The most used modes are d_{31}, d_{33}, and d_{15}, which are corresponding to the shear, normal, and torsional stresses in mechanical domain, as illustrated in Fig. 1.1 [28]. It's worth mentioning that piezoelectric materials also exhibit an inverse piezoelectric effect that creates mechanical strain or force as a response to applied electric potential. This property makes piezoelectric materials be widely used as actuators commercially available in markets.

The associated research interests in piezoelectric energy harvesting include but not limited to the development of advanced piezoelectric materials, theoretical characterizations at both material and harvester levels, design of novel transducers, potentially convertible energy sources, rectifying circuits, and applications in different areas. Piezoelectric materials used for the purpose of energy harvesting are generally categorized into polyvinylidene fluoride (PVDF), piezoelectric macro fiber composite (MFC), lead zirconate titanate (PZT), and

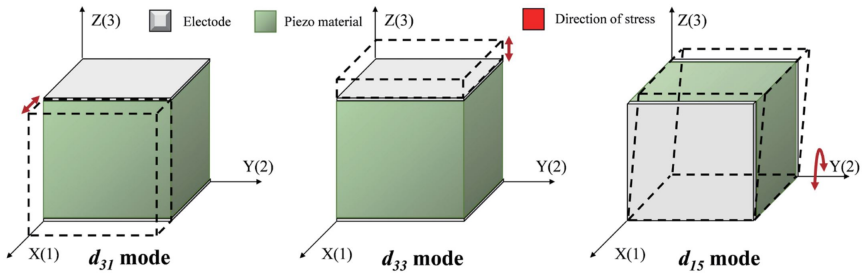

Figure 1.1: Working modes of piezoelectric materials (a) d_{31} mode, (b) d_{33} mode, and (c) d_{15} mode [28].

piezoelectric crystals. Theoretical models, including mechanical and electrical equations and variables, are developed to characterize the electromechanical coupling behavior of different piezoelectric materials and to predict power-generation performance under various ambient excitations. Ambient energy sources that could induce dynamic strain in surrounding structures and objects can be harvested using properly designed piezoelectric energy harvesters, such as mechanical and civil structural vibrations, fluid flow, pressure fluctuations, ocean waves and currents, human and animal motions, or even heart beating. An overall roadmap of piezoelectric energy harvesting consisting of materials, various harvesters, and potential applications are given in Fig. 1.2 [29]. The energy harvesting circuits rectify the generated irregular voltages could be found in [30, 31].

1.2 Piezoelectric energy harvesting from human walking

Wearable devices with integrated sensors have been well developed and applied in daily life with the purposes of living assistance, health/fitness status promotion, human-machine interactions, and rehabilitation. Human walking offers sufficiently harvestable, convertible, and continuous energy sources. Sue et al. [32] conducted a comprehensive investigation of the potentially harvestable energy sources in the human body and reviewed the operation

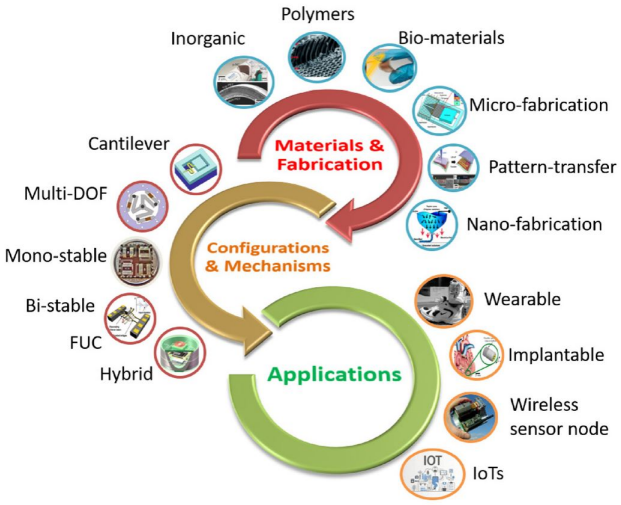

Figure 1.2: A roadmap of piezoelectric energy harvesting from materials to applications [29].

principle and performance of the harvesters for energy harvesting from the human body. Energy harvesting from human motion has proven to be a convenient and promising way to continuously power wearable sensors and low-power electronic devices [3, 6], such as wireless transceivers [4], healthcare watches [33], smart band, pacemakers, and cell phones [34]. Various mechanisms including but not limited to electromagnetic [3, 4, 35], piezoelectric [7, 36, 37, 38, 39], and triboelectric [10, 40], have been exploited to convert human-generated mechanical energy to electrical energy. Among them, piezoelectric materials show special potentials and therefore are the most extensively investigated for their high power density and large force capacity with a small displacement [41, 42]. Piezoelectric materials have also been used to convert biomechanical energy, like human muscle-movement of a finger, into usable electricity [43].

Among the available energy sources in human motions, footstep energy is recognized as the largest one [44]. Foot motion exhibits multiple convertible energy sources, including acceleration induced by leg swing, acceleration pulse [6], and large force upon heel strike [3, 45]. A PVDF insole stave and a thunder PZT plate were integrated into shoes to scavenge energy from footfalls and generated an average power output of 1.1 mW and 1.8 mW,

respectively [46]. A rotary electromagnetic shoe generator was also studied in [46] for comparison, which showed a much larger power output of 0.23 W. However, the electromagnetic shoe generator was blamed for being awkward in volume and the large stroke which could discomfort wearers. A curved PZT dimorph (3-1 mode) with metal mid-plate was mounted in a heel that harvested an average power of 8.4 mW across the optimal resistance of 500 $k\Omega$ at the strike frequency of 0.9 Hz [47]. The advantages and disadvantages of different piezoelectric film benders were evaluated based on their suitability and performance for shoe insert harvesters [48]. A piezoelectric cantilever magnetically coupled with a ferromagnetic ball and a crossbeam was mounted in a shoe heel that had a power output ranging from 0.03 mW to 0.35 mW over the walking speeds from 2 km/h to 8 km/h [49]. A shoe-mounted piezoelectric cantilever with a proof mass harvested an average power of 0.40 mW from heel accelerations [6]. A footwear energy harvester with a sandwiched piezoelectric transducer in the flex end-caps was designed and tested, which could generate an average power of 2.5 mW at the walking speed of 4.8 km/h [50]. Recently, a PVDF transducer was integrated into a slipper to harvest the bending energy without a heel counter, which produced a maximum power of 15 nW at the walking speed of 6 km/h [51]. An average power output of 1 mW was generated by the shoe-embedded multi-layer PVDF harvester sandwiched in two wavy plates [8]. A similar design was implemented in a self-powered insole that can harvest energy from foot pressure and was demonstrated to be capable of powering a wearable watch and smart band [8]. An additional benefit of the energy harvesting insole is that the generated electric waveform signals can also be used to track human movement patterns and thus monitor human health. These pioneer studies have accumulated very valuable experience and inspired many scholars to further explore more in energy harvesting from human walking.

A great challenge of piezoelectric footwear harvesters is the small power output due to the low excitation level and frequency. Most of the proposed harvesters could provide the

power of several milliwatts. Nevertheless, typical low-power electrical devices require a few tens of milliwatts. For instance, a common Bluetooth needs an average power of 18 $\sim$ 27 mW for a typical user profile [52]. Therefore, a large gap still needs to be filled by generating adequate power for typical low-power electronic devices to realize the application of energy harvesting in wearable devices and sensors for health care monitoring.

1.3 Piezoelectric energy harvesting from torsional vibration

Harvesting energy from ubiquitous vibrations has received increasing attention in the past decade [53, 54, 55, 56, 57], especially, those based on bending vibrations of beam and plate structures [58, 59, 60]. Torsional vibration frequently happens in various engineering applications, such as oil and gas drilling systems [61], wind turbines [62], combustion engines of vehicles and helicopters [63]. Nevertheless, very few investigations have been conducted on torsional vibration energy harvesting, which may have promising applications in structural health monitoring. As well known, various sensors have been extensively utilized in oil and gas drilling for the measurements of depth, pressure, temperature, direction, etc. These sensors usually operate in a harsh down-hole environment and experience high shock impact as well as high temperatures. Powering these sensors using traditional batteries in such a harsh environment can be very challenging. Furthermore, the replacement of batteries results in frequent interruption of the drilling process, low efficiency, and high cost. Harvesting energy from the torsional vibration of a drill shaft (or pipe) could provide an alternative and continuous power source for those sensors. The harvested vibration energy can be used as either a direct replacement or an augment of traditional batteries, thereby prolonging the service life of sensors in use [64, 65].

In a typical vibration energy harvesting system, the transducer for mechanical-to-electrical energy conversion is pivotal. Piezoelectric transducers have received extensive attention due to their footprint, which makes it much more desirable for harvesting energy from the oil drill shaft due to the very limited space [66]. Most available piezoelectric transducers are designed to harvest energy using the longitudinal mode d_{33} and transverse mode d_{31}. Nevertheless, the shear-mode d_{15} is also worthy of attention, which is greater than d_{33} and d_{31} for most piezoelectric materials. Musgrave et al. [67] proposed the concept of torsional vibration energy harvesting using a piezoelectric transducer in d_{31} mode. Ren et al. [68] investigated the piezoelectric energy harvesting using PMN-PT material and found that the d_{15} mode harvester produced the largest power density of 10.67 $\mathrm{mW/cm^3}$ compared with the other two modes. Kulkarni [66] developed a shear-mode piezoelectric device to harvest energy from torsional stresses. Abdelkefi et al. [69] reported a 30% increase in the harvested power using piezoelectric cantilever beams undergoing coupled bending-torsion vibrations compared to the case of bending beams only. Chen et al. [70] derived analytical expressions and numerical results of voltage, current, power output, and the efficiency of a circular piezoelectric generator mounted on a rotationally vibrating base. Kim [71] studied a piezoelectric cantilever beam transducer for harvesting energy from torsional vibration induced by internal combustion engines. Recently, Zheng et al. [72] and Zhu et al. [73] developed an analytical model of a d_{15} mode piezoelectric cantilever harvester based on the Timoshenko beam theory. To the best of the authors' knowledge, harvesting energy from the torsional vibration of a drilling shaft to charge in-service sensors has not yet been sufficiently explored. A theoretical model is needed to predict the harvestable power from the rotational shaft and to conduct parameter analysis. Furthermore, the optimal position of the transducer on the shaft is needed to be identified to generate the maximum energy.

1.4 Broadband bi-stable piezoelectric energy harvesting

The linear piezoelectric cantilever is the most widely studied energy transduction device for mechanical-to-electrical energy conversion because of its simplicity [35]. However, linear piezoelectric energy harvesters can only effectively harvest energy at or very close to resonance, which leads to significant efficiency reduction at frequencies slightly away from the resonant frequency [7, 74]. Various approaches have been developed to broaden the operational frequency range of piezoelectric harvesters, such as frequency-up conversion [75], multiple resonator arrays [76], and exploitation of nonlinear responses [77]. Among the latter, nonlinear bi-stability has exhibited versatile features in harvesting energy from broadband vibrations due to the large power outputs associated with the global snap-through dynamics.

Bi-stable piezoelectric energy harvesters can be realized through different mechanisms, including mechanical preloading, magnetic interaction, or residual thermal stress in composite laminates. Extensive reviews on bi-stable energy harvesting by exploiting different bi-stability mechanisms and transductions were published in [78, 79]. Cottone et al. [80] used an axially loaded beam to form a buckled bi-stable piezoelectric vibration energy harvester that produced up to an order of magnitude more power than the unbuckled case. Ando et al. [81] and Qian et al. [82] exploited the bi-stable response of an axially pre-loaded clamped-clamped beam to the transverse excitations for piezoelectric energy harvesting over a wide frequency bandwidth. Harne et al. [83] developed a bi-stable energy harvesting device using an inertial mass connected to a translational slide bearing and a pre-compressed spring. The axial load leads to a negative stiffness that is sufficient to overcome the positive stiffness of the system and induces bifurcation via buckling. However, exerting a mechanical preload to a system usually involves additional constraints making the system clumsy. In comparison, magnetic interaction allows a more flexible design of bi-stable systems because of the contactless repulsive or attractive magnetic forces. The repulsive magnetic force be-

tween a fixed magnet and another one at the free end of a cantilever piezoelectric beam induces negative stiffness into the system and results in a bi-stable harvester [84, 85]. Zhou et al.[86] used two tilted magnets and a cantilever beam with another tip magnet to build a bi-stable piezoelectric harvester. The inclination angle of the magnets was shown to play a vital role in broadening the operating bandwidth and enables rich nonlinear characteristics [87]. A magnetically coupled two-DOF bi-stable energy harvester consisting of two rotary piezoelectric cantilevers with tip magnets was investigated for energy harvesting from rotational motions of multiple frequency bands [88]. One disadvantage of magnet-based energy harvesters is that the magnetic field could interact with electronics and sensors to be powered. Bi-stability can also be realized by laminated composites where the residual thermal stress difference causes curvatures after the curing procedure from a high temperature to room temperature due to the differing thermal expansion coefficients in different layers [89, 90]. Syta et al. [91, 92] investigated experimentally nonlinear dynamics of a bi-stable piezoelectric laminate plate and examined the modal response using Fourier spectrum based on the generated voltage time series. Pan et al [93] investigated the influence of the layout of the hybrid symmetric laminates on the energy harvesting performance and the dynamics via finite element numerical analysis and experimental validation [94]. In addition to the complicated manufacturing process and high cost, laminate composites are sensitive to environmental moisture and temperature, resulting in changes in material properties, especially for long-term services. Therefore, developing low-cost, magnet-free, bi-stable piezoelectric energy harvesters is highly desirable by exploring novel designs.

1.5 Objectives and contributions of the dissertation

This dissertation focuses on kinetic energy harvesting by developing novel piezoelectric transducers, which convert the kinetic energy in the form of mechanical vibrations, bio-inspired bi-stable motions, and human walking into electricity for powering wireless sensor nodes in oil drilling, health care monitoring, and animal tracking systems. Through analytical modeling, numerical simulations, and experimental validations, this research demonstrates that piezoelectric transducers working in different modes could be integrated into shoes, bio-inspired bi-stable structure, oil drilling shaft to scavenge kinetic energy surrounding these objects for a sustainable power supply. The innovations and contributions of this dissertation lie in the analytical modeling, optimization, ingenious mechanical design, bio-inspired design, and experimental verifications of footwear piezoelectric energy harvesters with force amplification mechanisms, a bio-inspired bi-stable piezoelectric energy harvester, and a torsional vibration piezoelectric energy harvester.

1.6 Dissertation organization

The rest of this dissertation is organized as follows: chapter two presents the design, analytical modeling, optimization, prototyping, and experimental results of a piezoelectric footwear energy harvester with a novel single-stage force amplifier. Specifically, the harvester consisting of several piezoelectric stacks in d_{33} mode is developed to harvest energy from the large dynamic force at a heel during human walking. The well-designed and optimized force amplification frames amplify and redirect the vertical dynamic forces before inputting to the horizontally deployed piezoelectric stacks for large power output. In chapter three, a material equivalent model is developed to simplify the multilayered piezoelectric stack into an equivalent bulk to address the mesh problem in FE modeling of the piezoelectric stack. The

piezoelectric films in the stack are of three hundred number of layers which are too thin to be modeled and meshed layer by layer or even if they can be meshed that will consequently result in a huge computational burden due to a large number of nodes and elements. A parameterized one-fourth FE model of the piezoelectric transducer unit including the piezoelectric stack and force amplification frame is established to expedite the dynamic analysis and experimentally validated by taking advantage of the symmetries in geometries, load, and boundary conditions. Chapter four introduces a two-stage force amplification mechanism for further amplifying the dynamic forces at the heel to improve the power output of the footwear energy harvester. The detailed design principle, experimental and numerical results are reported and discussed. In chapter five, a novel bi-stable piezoelectric energy harvester inspired by the rapid shape transition of the Venus flytrap leaves is developed, modeled, and experimentally validated for broadband vibration energy harvesting. A torsional piezoelectric vibration energy harvesting system is developed, modeled, and tested in chapter six for scavenging energy from oil drilling shaft to provide a continuous power supply for down-hole sensors. Finally, the conclusion and future directions are presented in chapter seven.

Chapter 2

Piezoelectric footwear energy harvester with a force amplifier

2.1 Chapter introduction

Multilayer piezoelectric stacks constituted of hundreds of thin piezoelectric films in d_{33} mode are capable of safely operating in large force environments. Hundreds of piezoelectric films could be mechanically layered together in series and electronically connected in parallel to increase its power density. Xu et al. [55, 95] systematically investigated the characteristics of a PZT-stack transducer, including the generated energy/power, the mechanical-to-electrical energy conversion efficiency, and the power delivered to an external electrical resistive load. The large force capacity of piezoelectric stacks enables them to be very suitable to harvest energy from a wide range of practical engineering environments [96, 97, 98, 99]. The piezoelectric stack is also an ideal transducer for harvesting energy from heel strike forces during human walking. Although the large force excitation at the heel has been utilized for a better energy source [47, 100] to harvest, the power output is usually very low, and there are very

few available research results of the dynamic force distribution over the heel, exclusively for energy harvesting purpose. To further enhance the mechanical-to-electrical energy conversion efficiency, force amplifiers have been designed to transmit and meanwhile amplify the input force to piezoelectric stacks [101, 102].

This chapter presents an embedded piezoelectric footwear energy harvester by exploring the dynamic force excitation in a heel. The harvester is constituted of multiple piezoelectric stacks integrated into the well-designed and optimized force amplification frames, which are sandwiched by two heel-shaped aluminum plates. A survey investigation is implemented to disclose the dynamic force distribution in the heel induced by body weight and heel-strike at different walking speeds. The measured dynamic forces are then used for the design and numerical simulation of the piezoelectric footwear harvester. A force amplification frame is designed, parameterized, and optimized to achieve a large force amplification factor and efficient energy transmission. Two prototypes of the proposed piezoelectric energy harvester, including a different number of piezoelectric stacks, are fabricated and tested on a treadmill. An analytical model only considering the piezoelectric stacks is developed and verified to be capable of precisely predicting the electrical outputs of the footwear harvester.

2.2 Measurement of the dynamic force at a heel

Piezoelectric stack transducers have larger load capacities [103] and therefore can survive under large force excitations. Generally, a large force excitation induces higher power output for a linear piezoelectric harvester. Different force amplification mechanisms have been developed to amplify the input force to piezoelectric stacks to improve the mechanical-to-electrical energy conversion efficiency. A compressive force amplification frame is designed in this study to amplify and transmit the vertical ground reaction force at a heel during human

walking to the piezoelectric stacks. Although human walking has been well recognized as a promising mechanical energy source for energy harvesting [104, 105], very few research results or data are available in the literature that could be directly used for the design and analysis of footwear energy harvesters.

In general, a well-designed footwear energy harvester is expected to fulfill both technical functionality and practical applicability. The former includes energy extraction, management, and storage, offering enough power for wearable low-power devices. The latter can be implantable, invisible, and durable without sacrificing comfort. The design of a functional footwear energy harvester is also subjected to the very limited space in a shoe except for the aforementioned functions. This study targets to place the harvester at the heel of a boot to make full use of the relatively large space and exploit the large vertical force available upon heel strikes. Research demonstrates that the ground reaction force over an entire sole exhibits a typical M-shape during human walking [106], which has two peaks in one gait cycle due to the body weight and the movement of the center of gravity. The first peak is the largest one at the heel. To determine the input force for the design of the force amplification frame, it is necessary to know the amplitude and distribution of the dynamic force at the heel. This section introduces a simple method to measure the dynamic force at a heel, which will be used as the input for the following numerical simulations.

The proposed footwear harvester consists of several piezoelectric stacks incorporated in the force amplification frames and two heel-shaped aluminum plates. The force amplification frames with inner piezoelectric stacks are fixed between the two aluminum plates by bolts. A hollow space is grooved in the boot heel to fit the harvester. During human walking, the vertical reaction force over the surfaces of the aluminum plates is approximately assumed to be equally allotted to the force amplification frames and ultimately amplified and transformed to the innermost piezoelectric stacks. Therefore, it is necessary to explore the force exerted

Figure 2.1: The force sensor,aluminum plates, and the installation location.

on the aluminum plates in order to design a reliable and effective force amplification frame for the energy harvester.

A straightforward way to measure the dynamic force undertaken by the aluminum plates is to sandwich a force sensor between the two aluminum plates and then put them into the heel, as shown in Fig. 2.1. In this study, two configurations, i.e., single force senor (PCB 208C03) and double sensors (PCB 208C02 and 208C03), are considered to measure the dynamic force amplitude and distribution on the aluminum plates. In the first configuration, a single sensor is placed at the central point of the plates, as shown in Fig. 2.2 (point P5), to measure the total dynamic force on the aluminum plates. In the second configuration, double sensors are deployed at a pair of points to detect the force distribution at different positions of the heel and meanwhile keep the two plates stable. Fig. 2.2 illustrates the considered potential position pairs for the placements of the double sensors. Three walking speeds, respectively, 2.5 miles per hour (mph) (4.0 km/h), 3.0 mph (4.8 km/h), and 3.5 mph (5.6 km/h), are covered in the test. The sensors are fixed between the two aluminum plates by four bolts, as shown in Fig. 2.1, which allow the plates to move toward each other. The device is installed into the heel of a hollowed boot (Belleville 790 ST, 790ST-9, TacticalGear.com). A Coco 80 dynamic analyzer is adopted to record the time history of the dynamic force. The experiments are conducted on a treadmill by a male subject with a bodyweight of 84 kg.

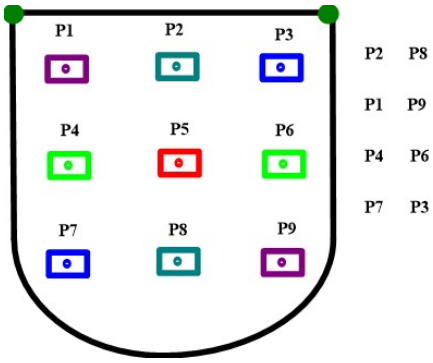

Figure 2.2: The measured positions.

Fig. 2.3 plots the measured dynamic forces on the aluminum plates under the three walking speeds from the signle sensor configuration. Only one peak of the reaction force at the heel can be observed in a gait period, which is different from the reported general M-shape ground reaction force consisting of double peaks at both the heel and forefoot [106]. The magnitude and frequency of the reaction force increase along with the increment of the walking speed. The maximum force amplitude is around $F_a = 600$ N at the walking speed of 3.5 mph (5.6 km/h). Only 3.0 mph (4.8 km/h) is tested in the double sensor configuration for simplicity since the general human walking speed is around 3.0 mph (4.8 km/h). The measured dynamic forces at different positions of the plates are presented in Fig. 2.4, which suggests that the dynamic forces are indeed slightly distinct at different positions of the plates. Fig. 2.4 also displays that the forces at the rear part of the heel (P7, P8, and P9) are larger than those at the front part (P1, P2, and P3), and the forces at the lateral side of the heel (P6 and P9) are larger than those at the medial side (P4 and P1). Nevertheless, the total peak values of the forces from the double sensors are almost the same at the four pairs of positions, which is around 600 N. The measured reaction forces on the plates are very useful for the design and optimization of the force amplification and the numerical simulations.

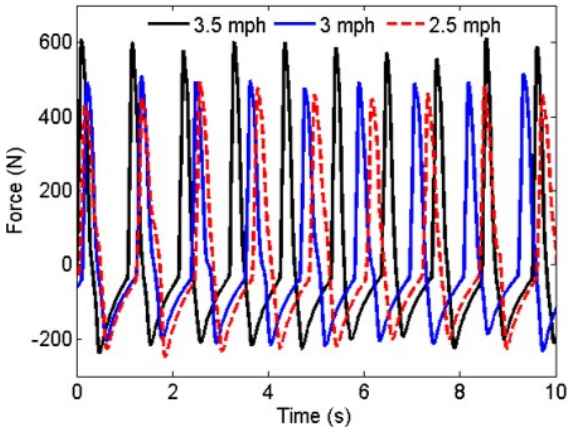

Figure 2.3: Measured dynamic forces at the walking speeds of 2.5 mph (4.0 km/h), 3.0 mph (4.8 km/h) and 3.5 mph (5.6 km/h) from single sensor.

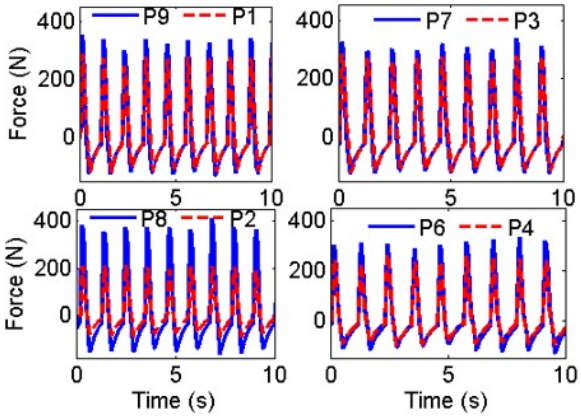

Figure 2.4: Measured dynamic forces at different positions at the walking speed of 3.0 mph (4.8 km/h).

2.3 Design of the embedded piezoelectric harvester

The proposed footwear energy harvester comprises multiple piezoelectric stacks in the force amplification frames and two heel-shaped aluminum plates. Therefore, its design essentially is to finalize the geometric sizes of both the aluminum plates and the force amplifier under the conditions of the limited space and large force input. The plates should be stiff enough to withstand the vertical dynamic force at the heel during walking and fully transfer the distributed force to the force amplification frames. This requires the aluminum plates to be thick enough to prevent undesired deformation, which could results in the energy stagnation in the plates in the form of strain energy. However, thick plates occupy more precious space in the heel, which is at the cost of sacrificing the potential space for force amplification frames. Furthermore, the plates are expected to cover the entire heel area to gather as much as possible the vertical distribution forces and fit the inside shape of the heel to achieve the embeddable and invisible features. Given the above analysis, the ultimate design of the plates fitting to a 9-size Belleville boot (26 cm in length) is illustrated in Fig. 2.5, which

depicts the detailed dimensions. The two reserved grooves in the plate are for the fixation of the force amplification frames.

The design of the compressive force amplification frame is of vital importance for the safety and energy generation performance of the harvester. One obligation of the frame is to transmit the mechanical motion and force in the vertical direction to the inner piezoelectric stacks deployed in the horizontal direction. This motion transmission allows the full use of the relatively larger space along the horizontal direction in the heel and therefore makes longer piezoelectric stacks possible to be integrated into the device. Longer piezoelectric stacks contain more piezoelectric films, which could produce more power at the same input excitation compared with shorter ones. The other function of the frame is to magnify the vertical force transferred from the aluminum plates so that the force applied to the piezoelectric stacks can be as large as possible within the material allowable stress to generate more power. In addition to these requirements, the frame also needs to have adequate safety capacity to survive in the large dynamic force environment.

The proposed force amplification frame to fulfill the functions stated above is shown in Fig. 2.6, which is made up of four identical thick beams that are hinged with two end blocks and two middle blocks through eight identical thin beams. The thin beams essentially play the role of hinges to release the bending constraints between the thick beams and blocks. The inner length of the frame is the same as the length of the selected piezoelectric stack. The piezoelectric stack contains n=300 PZT (Ceram Tec SP505) layers of 0.1mm and 301 layers of pure silver electrodes with the thickness of 0.1 µm [55]. The geometric sizes of a single piezoelectric layer are $a_p \times b_p \times t_p = 7.0$ mm $\times$ 7.0 mm $\times$ 0.1 mm, and the total length of the piezoelectric stack is L=32.34 mm. Stack holders at the insides of the end blocks are designed to keep the piezoelectric stack from falling out in the dynamic environment. Fillets are implemented at the corners and the connection positions between thick and thin

beams to reduce stress concentration due to sudden cross-section changes. An M3 thread in each middle block is to fix the frame to the aluminum plates and take the input force (F_{in}) transferred from the plates. The output force F_{out} of the frame is directly exerted to the inner piezoelectric stacks as shown in Fig. 2.6. Therefore, the force amplification factor of the frame can be calculated by $\alpha = \frac{F_{out}}{F_{in}}$. The beams have tilted an angle of θ to achieve the compressive force transmission. The hinges at corners partly release the bending constraints between blocks and thick beams, which can mitigate the stagnation of bending mechanical energy in the frame. In this way, mechanical energy generated from human walking can be efficiently transmitted to the inner piezoelectric stack with minimum loss. The frame is characterized by a set of parameters as defined in Fig. 2.6, which need to be determined and optimized under physical constraints.

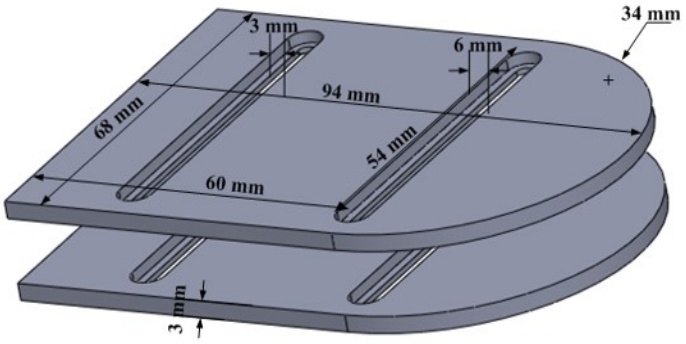

Figure 2.5: The heel-shaped aluminum plates.

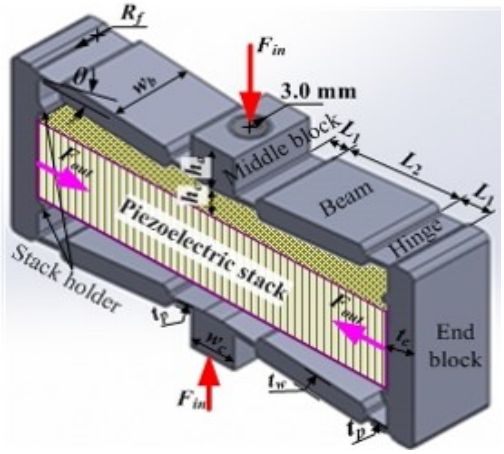

Figure 2.6: Design of the force amplification frame.

2.4 Optimization of the force amplification frame

To extract more power, the force amplification frame is expected to have a large force amplification factor so that it can offer as large as a possible force to the piezoelectric stack and

have enough safety capacity. In order to achieve such goals, an optimal frame model needs to be attained by optimizing the geometric parameters. The optimization is conducted in a combined and interactive environment of Ansys and Matlab. A parameterized finite element model (FEM) of the force amplification frame is developed and programmed using Ansys parametric design language (APDL) [107] to perform mechanical analysis under the input force F_{in}. The optimization algorithm is compiled and run in Matlab by reading the mechanical analysis results from Ansys. This section elaborates on the detailed procedure of the optimization.

2.4.1 Objective function

To determine the geometries of the force amplification frame, the applied force F_{in} to the frame needs to be specified first, which depends on the number of the force amplification frames in the harvester. Assume that n_s piezoelectric stacks are integrated into the harvester through n_s force amplification frames fixed between the two aluminum plates. The heel-strike force distributed over the plates is supposed to be equally transferred to each frame. The input force F_{in} to each frame can be calculated by $F_{in} = \frac{F_a}{n_s}$, where F_a is the force amplitude measured. Thus, the force applied to each piezoelectric stack is $F_{out} = \alpha F_{in} = \alpha \frac{F_a}{n_s}$, which is only determined by the force amplification factor α of the frame if both n_s and F_a are given. A large force amplification factor α is desired to get a high power output as analyzed previously. From the view of energy transmission, it is also expected that the mechanical energy from human walking could be transferred to the piezoelectric stack by the frame as much as possible. Therefore, the objective function of the minimization problem of the geometric parameters can be defined as

$$\Gamma_{obj} = min \left\{ \frac{1}{\chi \alpha \eta} \right\} \tag{2.1}$$

where $\eta = \frac{E_p}{(E_s+E_p)}$ is the energy transmission ratio, E_p and E_s are the strain energy in the piezoelectric stack and frame, respectively; χ is a penalty factor that is applied to the case when the candidate solution violates the constraint conditions. It can be seen from Eq.2.1 that the objective function has the minimum value when both the force amplification factor α and energy transmission η are maximum.

2.4.2 Optimization variables and constraint conditions

The selected optimization variables should be sensitive to the objective function. Some of the geometric dimensions of the frame that are evidently not very sensitive to the objective function are set to constants to make the optimization problem as simple as possible. For instance, the width of the frame is set to be the same with the width of the inner piezoelectric stack, i.e., $w_b = b_p$=7.0 mm. The height and width of the middle block are h_a=4 mm and w_c=5 mm, respectively. The optimization variables include the length and thickness of the thin beam L_1 and t_p, the tilt angle θ, the chamfer radii R_f, the thickness t_w of the thick beams and the thickness t_e of the end blocks. It is noted that the length of the thick beams L_2 is not an independent variable since it can be determined from the length of the thin beams and the tilt angle. Therefore, the dimension of the optimization problem is six.

The constraint conditions of the optimization problem come from the material strength and the geometrically compatible relation between the deformed frame and piezoelectric stack. The maximum stresses in both the force amplification frame and piezoelectric stack should be less than the allowable material stresses. The up and down headroom between the top surface of the piezoelectric stack and the bottom surface of the middle block should be greater than zero after the frame deforms to forestall the deformed frame to break the piezoelectric stack. Based on the above analysis, the constraint conditions can be expressed as follows.

- Stress constraint conditions: $\sigma^f_{max} \leq \sigma^f_a$; $\sigma^p_{max} \leq \sigma^p_a$;
- Geometric constraint condition: $h_c > 0$;

where σ^f_{max} and σ^p_{max} are the maximum stresses in the frame and the piezoelectric stack, respectively, while σ^f_a and σ^p_a are the material allowable stresses of the frame and the piezoelectric stack. h_c is the head room between the middle block and the piezoelectric stack.

2.4.3 Optimization procedure

Biogeography-based optimization (BBO) algorithm[108] is employed in this study to conduct the parameter optimization due to its easy implementation and high efficiency. The idea of BBO algorithm is inspired from the natural laws of evolution, migration, and extinction of species between different habitats in a regional ecological environment. In the BBO algorithm, each candidate solution $\mathbf{v}_i$, defined as a biogeography habitat, usually consists of a set of independent variables $\{v_{i1}, v_{i2}, \ldots, v_{ik}\}$ (i=1,..., N, and N is the population number of candidate solutions, k is the dimension of the optimization problem). In the current problem, k equals 6 and v_i is actually one of the combination of the optimization variables in the parameter space, i.e. $\{v_{i1}, v_{i2}, v_{i3}, v_{i4}, v_{i5}, v_{i6}\} = \{L_1, t_p, \theta, R_f, t_w, t_e\}$. Those independent variables represent the environmental features or suitability index variables (SIVs) in the biogeography habitat. The fitness of a candidate solution acts as the role of habitat suitability index (HSI), which can be evaluated from the comparison of its objective function value with summation of the objective function values of all candidate solutions in the population.

The evolution of a solution is accomplished by immigration, emigration, and mutation operators of its independent variables with different probabilities based on its fitness. A good solution for a minimum problem has a relatively small value of the objective function

and large fitness value, and thus, it has a high emigration rate λ and low immigration rate μ. The mutation operator is to simulate the natural mutation of natural species (environmental features or SIVs), which can bring in fresh information and maintain the diversity of species in the habitat. The main goal of mutation in the algorithm is to avert the population from converging to a locally suboptimal solution by probably changing one or more of its individual variables. The Gaussian mutation is adopted in this study. The mutation form of each probably selected independent variable v_{ij} in a candidate solution v_i can be obtained from the Gaussian distribution $\hat{v}_{ij} \sim N_i(v_{ij}, \tilde{\sigma}^2)$, in which $\tilde{\sigma}$ is the presetting variance to control mutation range. Readers interested in more about the biogeography-based optimization are referred to the Ref. [108].

The optimization is coded and conducted in Matlab. A parameterized FEM programmed in APDL, as shown in Fig. 2.7, is established in Ansys (R14.0) to evaluate the objective function of each candidate solution v_i by performing static mechanical analysis. It is worth mentioning that the piezoelectric effect is not considered in the static analysis. The tetrahedral solid element 72 is used to model both the frame and piezoelectric stack to smoothly mesh the irregular geometric shape at the corners of the frame. In the modeling, the equivalent node force is applied to the top surface of one of the middle blocks to simulate the input force F_a. The fixed boundary condition is applied to the bottom surface of the other middle block. The output force F_{out} of the frame, exerted on the piezoelectric stack, is obtained by integrating the normal stress over the cross-section, as shown in Fig. 2.8. The strain energy E_p and E_s in the piezoelectric stack and frame are respectively derived by summing the element strain energy.

Fig. 2.9 illustrates the diagram of the optimization procedure based on the interactive connection and data exchange between Matlab and Ansys. The algorithm parameters to be initialized include the optimization variable space, the number of the maximum generation

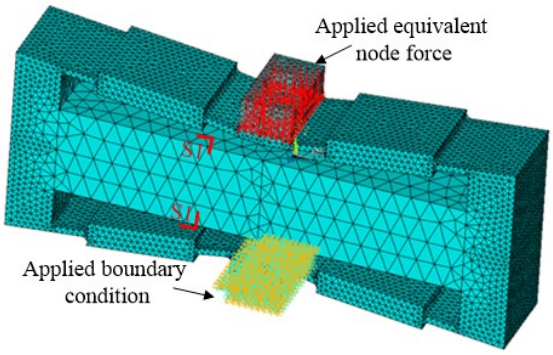

Figure 2.7: Finite elmement model of the force amplification frame with inner piezoelectric stack.

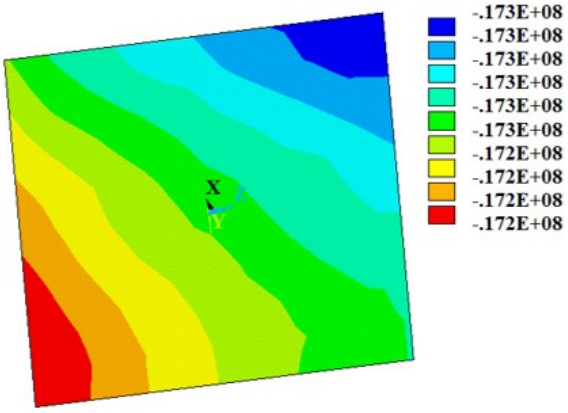

Figure 2.8: Normal stress distribution over the cross-section of the piezoelectric stack.

G, mutation probability, the capacity of the population, and the dimension of each solution in the population. In the algorithm, each candidate solution is generated in the Matlab and then written into a predefined file *variable.dat*. After that, the programmed Ansys APDL code of the parameterized FEM, which is saved in the file *Model.dat* is invoked. The Ansys program reads the values of the optimization variables from the file *variable.dat* to build the FEM for the current candidate solution and performs the mechanical analysis. The analysis results, including the force amplification factor α, energy transmission efficiency η, maximum stresses σ^f_{max}, and σ^p_{max}, and geometric constraint judgment condition h_c of the deformed frame, are then saved in the file *ansysresult.dat*. The objective function of the current solution is then evaluated in the Matlab by importing the results in *ansysresult.dat*. The objective function values of all the candidate solutions can be attained in a similar way, and the fitness of each solution can thus be computed to determine the corresponding emigration rate λ and immigration rate μ. The optimization algorithm steps into the next generation by the evolvement of the candidate solutions based on the emigration, immigration, and mutation operations and then go through the same procedure until it reaches the final generation G and outputs the optimal solution.

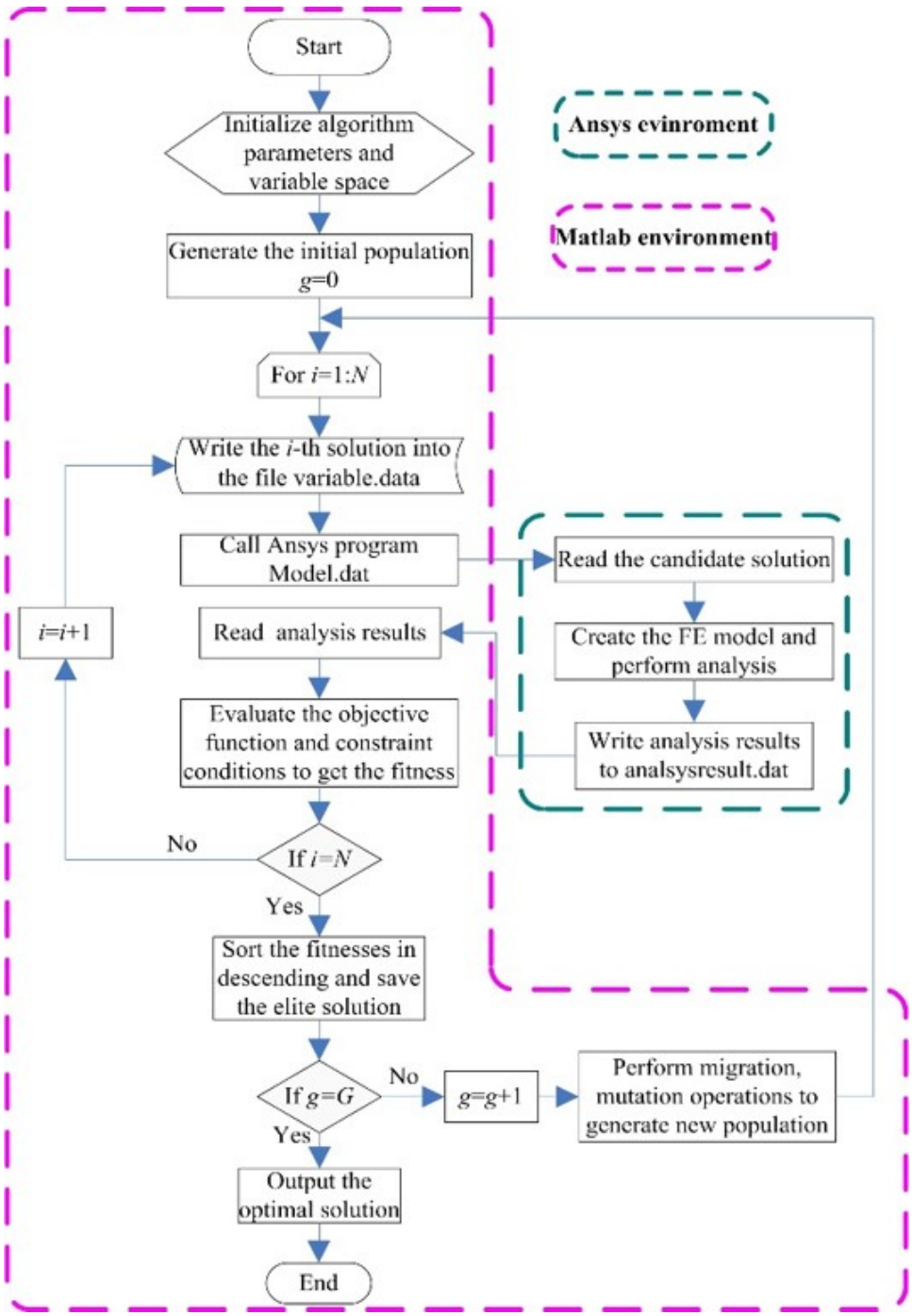

Figure 2.9: Diagram of the optimization procedure.

2.5 Dynamic modeling

Once the optimal parameters of the force amplification frame are obtained, the force amplification factor of the optimal model is known. Consequently, the dynamic force $F_{out}(t)$ applied to each piezoelectric stack can be obtained by

$$F_{out}(t) = \alpha \frac{F(t)}{n_s} \tag{2.2}$$

where $F(t)$ is the measured dynamic force over the aluminum plate during human walking, as plotted in Fig. 2.3. It should be emphasized that Eq.2.2 is only valid when the frequency of the excitation force $F(t)$ is much smaller than the natural frequency of the piezoelectric transducer unit consisting of both the piezoelectric stack and the force amplification frame. This is true for the ongoing study. Because the human walking frequency is very low, usually between 0.8 Hz and 1.2 Hz, depending on different motion speed and body geometries [3].

A single-degree-of-freedom (SDOF) model is presented in this section to characterize the electromechanical coupling behavior and predict the voltage and power output of the harvester with multiple piezoelectric stacks under human walking dynamic force. The detail structure of the multilayer piezoelectric stack is depicted in Fig. 2.10 (a), where L is the total length of the stack, and $v(t)$ is the voltage output. The red arrows indicate the polarization directions of the piezoelectric films electrically connected in parallel. The cross-sectional area of the stack is denoted by A, as shown in Fig. 2.10 (b). The free-body diagram of the simplified SDOF model is given in Fig. 2.10 (c), in which $x(t)$ is the displacement, m is the total mass of the stack, and $F_p(t)$ is the piezoelectric force. By balancing the force, the equation of motion of the simplified model can be written as

$$m\ddot{x}(t) = F_{out}(t) - F_p(t) \tag{2.3}$$

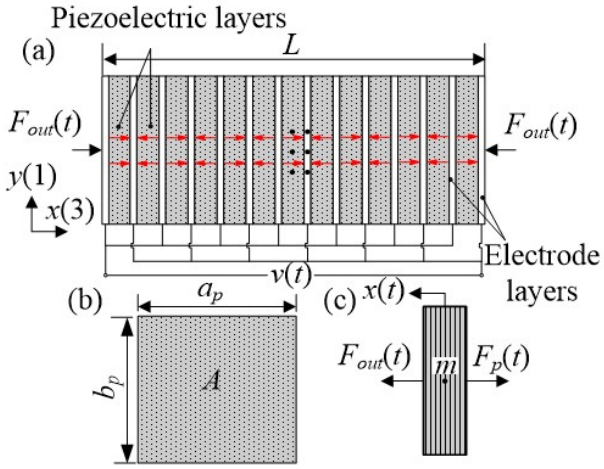

Figure 2.10: (a) Schematic of the piezoelectric films in a piezoelectric stack, (b) cross-section of the piezoelectric stack, and (c) simplified electro-mechanical coupling model

The piezoelectric force $F_p(t)$ can be derived from the constitutive equation of piezoelectric material as follows. Assume that $S_3(t)$ and $T_3(t)$ are the axial strain and stress in the piezoelectric stack under the applied force $F_{out}(t)$. The electric field density and electric displacement are denoted by $E_3(t)$ and $D_3(t)$, respectively. The linear constitutive equations of piezoelectric materials in d_{33} mode can be written as [109].

$$S_3(t) = s_{33}^E T_3(t) + d_{33} E_3(t) \tag{2.4}$$

$$D_3(t) = d_{33} T_3(t) + \varepsilon_{33}^T E_3(t) \tag{2.5}$$

where s_{33}^E, d_{33} and ε_{33}^T are the compliant constant, piezoelectric strain constant and dielectric constant. The superscripts E and T indicate that the corresponding parameters are measured at the constant electric field and constant stress, respectively. The strain, stress and electric field density can be related to the displacement $x(t)$, force $F_p(t)$, and the voltage $v(t)$ by $S_3(t) = \frac{x(t)}{L}$, $T_3(t) = \frac{F_{out}(t)}{A}$, $E_3(t) = -\frac{v(t)}{t_p}$. It is worth noting that the voltage across each piezoelectric film in the stack is reasonably deemed as identical with the one across the

external resistive load. This is because all the piezoelectric films are connected in parallel, and all the piezoelectric stacks in the harvesters are also connected in parallel with the external resistance. Assume the total electric charges over all the cross-sectional areas of the piezoelectric films in one stack is $q_3(t)$, then the electric displacement can be expressed as $D_3(t) = \frac{q_3(t)}{A}$. Substitution of these terms into the constitutive equations gives

$$x(t) = \frac{L}{EA}F_p(t) + d_{33}L\frac{v(t)}{t_p} \tag{2.6}$$

$$q_3(t) = nd_{33}F_{out}(t) + n\varepsilon_{33}^{T}A\frac{v(t)}{t_p} \tag{2.7}$$

where n is the number of piezoelectric layers in one stack and $E = \frac{1}{s_{33}^{E}}$ is the elastic Young's modulus of the piezoelectric material. Solving for $F_p(t)$ from Eq.2.6 and substituting it into Eq.2.3 yields

$$m\ddot{x}(t) + \frac{EA}{L}x(t) - d_{33}EA\frac{v(t)}{t_p} = \frac{\alpha}{n_s}F(t) \tag{2.8}$$

where the Eq. 2.2 has been used. The above equation can also be written as

$$m\ddot{x}(t) + \omega_n^2 x(t) - n\omega_n^2 d_{33}v(t) = \frac{\alpha}{mn_s}F(t) \tag{2.9}$$

where $\omega_n = \sqrt{\frac{EA}{mL}}$ is the natural frequency of the piezoelectric stack. For the proposed footwear energy harvester consisting of n_s piezoelectric stacks, the totally generated charge is

$$Q_3(t) = n_s q_3(t) = n_s\left(nd_{33}F_{out}(t) + n\varepsilon_{33}^{T}A\frac{v(t)}{t_p}\right) \tag{2.10}$$

Assuming no external electric field is exerted to the piezoelectric stack, the applied

force can be approximately related to the displacement by $F_{out}(t) = \frac{EA}{L}x(t)$. Thus, the above equation becomes

$$Q_3(t) = n_s n d_{33} m\omega_n^2 x(t) + n_s C_p v(t) \tag{2.11}$$

where $C_p = \frac{n\varepsilon_{33}^T A}{t_p}$ is the capacitance of one piezoelectric stack. Assume the harvester is connected to an external resistor R, then the current flowing in the resistor can be expressed as

$$\dot{Q}_3(t) = n_s n d_{33} m\omega_n^2 \dot{x}(t) + n_s C_p \dot{v}(t) = -\frac{v(t)}{R} \tag{2.12}$$

which can be written as

$$\dot{v}(t) + \frac{v(t)}{n_s R C_p} + \frac{nm\omega_n^2 d_{33}}{C_p}\dot{x}(t) = 0 \tag{2.13}$$

The equations of motion of the developed footwear harvester consist of the mechanical Eq.2.9 and electrical Eq.2.3. With the measured reaction force on the aluminum plate of the harvester during human walking, the voltage output can be attained by numerically integrating Eqs.2.9 and 2.14. The instantaneous power and average power output of the harvester can be then calculated by

$$P(t) = \frac{v^2(t)}{R} \tag{2.14}$$

$$\bar{P}(t) = \frac{1}{T_s}\int_0^{T_s} \frac{v^2(t)}{R} dt \tag{2.15}$$

where T_s is the total time span.

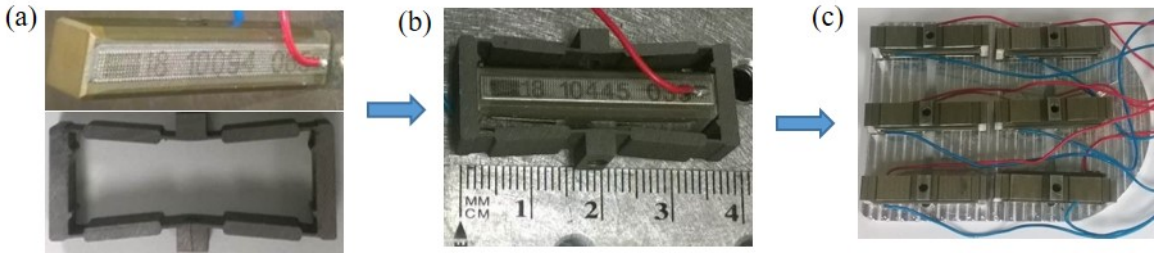

Figure 2.11: (a) Piezoelectric stack and fabricated force amplification frame, (b) integration of the stack and force amplification frame, and (c) assembled harvester with six piezoelectric transducers.

2.6 Prototype assemble and experimental setup

The force amplification frames with the optimal geometric parameters are manufactured by use of spring steel material, as shown in Fig. 2.11(a). The length and height of the force amplification frame are 37.34 mm and 14.83 mm, respectively. The piezoelectric stacks are then integrated into the force amplification frames, as depicted in Fig. 2.11(b). All the frames together with the piezoelectric stacks are fixed to the heel-shaped aluminum plates using bolts. As an example, Fig. 2.11(c) shows the assembled harvester, including six frames and piezoelectric stacks, in which only one of the aluminum plates is assembled to give an inside view of the harvester. Fig. 2.11(c) shows that there is still additional space for more frames and piezoelectric stacks between the plates. However, more frames to be included in the harvester will result in smaller force partaken by each frame and thus lower power output. The assembled harvester fits well to the hollowed boot heel, as shown in Fig. 2.12. The overall height and weight of the prototype are 24 mm and 226 g, respectively. The boot with the harvester weights 1086 g, which is 143 g more than the original boot. The embedded harvester is completely invisible from the outside of the boot.

Experiments are conducted on a treadmill by a subject with a bodyweight of 84 kg and a height of 172 cm. Different external resistive loads from 300 Ω to 15 kΩ are considered

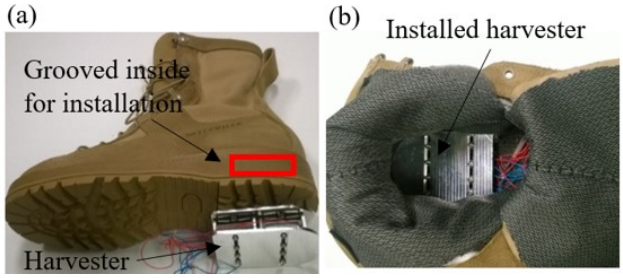

Figure 2.12: (a) Assembled harvester and the installation location, (b) installed harvester in the heel.

Figure 2.13: Experimental setup.

in the experiments to identify the optimal resistance that could yield the maximum power output. An oscilloscope records the time series of the voltage output at different external resistive loads. The experiment setup is shown in Fig. 2.13. Two harvesters, respectively, one with eight stacks and frames and the other with six stacks and frames, are tested in the experiments. Three different walking speeds, 2.5 mph (4.0 km/h), 3.0 mph (4.8 km/h), and 3.5 mph (5.6 km/h), are tested for the harvester with eight piezoelectric stacks and frames. While only the first two walking speeds are considered for the harvester with six piezoelectric stacks to prevent the frames from being broken by a large heel-strike force. This is because fewer stacks included in the harvester and larger walking speed will result in the large force input to each frame.

2.7 Results

2.7.1 Optimization results

The optimization of the force amplification frame is implemented for the harvester with six piezoelectric stacks. Therefore, the applied static force to the frame is F_{in} =100 N based on the measured maximum force amplitude F_a = 600 N. The spring steel of 60Si2CrVa is chosen to manufacture the prototype of the frame because this material has a higher yield strength of 1600 MPa [102]. The material properties of the force amplification frame and the piezoelectric stack are given in Table 2.1. Given the usable space between the two aluminum plates of the harvester, the optimization variable spaces assigned for all the variables are as the following: $L_1 \in [0.8\ 3]$mm, $\mathrm{t_p} \in [0.35\ 0.55]$mm, $\theta \in [5\ 10]$ degree, $R \in [0.15\ 0.3]$mm, $\mathrm{t_w} \in [1.2\ 1.8]$mm, $\mathrm{t_e} \in [0.5\ 2.5]$mm. The stress constraints are set to be σ_a^f=800 Mpa and σ_a^p=50 Mpa for the frame and piezoelectric stack from the safety point of view. The assigned penalty factor χ for artificially enlarging the value of the objective function of the solutions violating the geometric constraint is 0.01. The optimization algorithm control parameters are given as: the maximum generation G = 50, population size N=100 and mutation probability of 0.08.

The convergence of the objective function is presented in Fig. 2.14, which demonstrates that the objective function quickly decreases and approaches to the convergent solution. The obtained optimal values of the optimization variables are also presented in Table 2.1. The stress distribution of the optimal model is shown in Fig. 2.15, which shows that the maximum tensile stress is around 450 Mpa and locates in the thin beams. The force amplification factor of the optimal frame is found to be α=8.5 and will be used in the following numerical simulations.

Table 2.1: Geometric and material properties of the optimal force amplification frame and the piezoelectric stack:

Optimal dimensions of the FAF:		Spring steel material (60Si2CrVa)	
$L_1^{opt} = 1.66$ mm;	$R_f^{opt} = 0.29$ mm;	Yield strength: 1600 MPa;	
$t_1^{opt} = 0.41$ mm;	$t_w^{opt} = 1.79$ mm;	Young's modulus: 210 Gpa;	
$\theta^{opt} = 5^o$;	$t_e^{opt} = 2.50$ mm;	Poisson's ratio: 0.32;	
h_a=4 mm;	w_b=5 mm;	Piezoelectric material:	
Geometric dimensions of the stack:		$s_{33}^E = 24.0 \times 10^{-12}$ m^2/N;	$d_{33} = 475\ pC/N$;
a_p=b_p=7.0 mm;	L_p=32.34 mm	$\varepsilon_{33}^T/\varepsilon_0 = 1880$;	$\varepsilon_0 = 8.854pF/m$;

Note: s_{33}^E is the compliant constant of the FAF and ε_0 is the dielectric permittivity of the piezoelectric material in the free space.

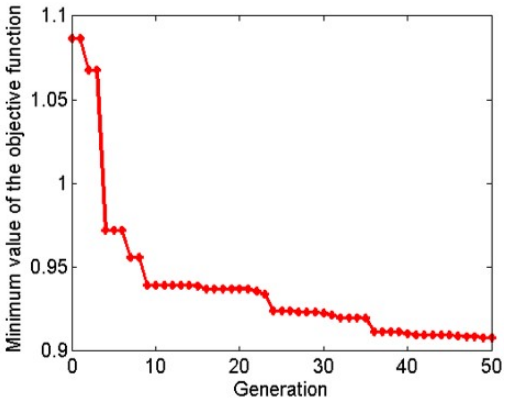

Figure 2.14: Convergence of the objective function.

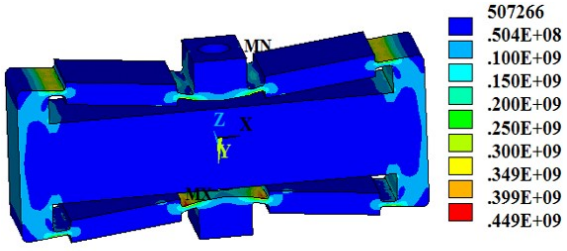

Figure 2.15: Stress distribution of the optimal frame (Pa).

2.7.2 Experimental and numerical results

As an example, Fig. 2.16 (a) presents the measured and simulated voltage output of the harvester with eight piezoelectric stacks and frames at walking speed of 3.0 mph (4.8 km/s) and the electrical resistance of 510 Ω. It can be seen that the amplitude of the voltage output is around 5.8 V, and the numerical prediction has a very good agreement with the treadmill test result. This demonstrates that the presented SDOF model is capable of reliably predicting the electric response of the harvester under the dynamic force measured from human walking. It should be noted that the input dynamic force to the SDOF model in the numerical simulation is measured from the single force sensor as plotted in Fig. 2.3. Fig. 2.16 (b) plots the corresponding instantaneous power output obtained by Eq.2.4, which shows that the maximum instantaneous power is around 57 mW. The measured and simulated voltage and power outputs of the harvester with eight piezoelectric stacks and frames for a large electrical resistance of 15 kΩ are displayed in Fig. 2.17 (a) and (b), respectively. Very good agreements between the measurements and simulations are observed from both the voltage and power plots again. The amplitudes of the instantaneous voltage and power are around 20 V and 28 mW. It should be emphasized that the resistance is not optimal, which would be expected to give a much larger transient power output.

To investigate the performance of the footwear energy harvester at different walking speeds, the root mean square (RSM) of the instantaneous voltage and average power outputs are calculated from the voltage responses over different resistive loads. The measured and simulated RMS voltage and average power of the harvester with eight piezoelectric stacks over varying resistance are presented in Fig. 2.18 (a), (b) and (c) at the walking speeds of 2.5 mph (4.0 km/h), 3.0 mph (4.8 km/h), and 3.5 mph (5.6 km/h). In order to quantitatively validate the proposed numerical model, the simulated RMS voltage and the experiment results at different walking speeds for the resistance of 510 Ω, 1.1 kΩ, 5.1 kΩ, 9 kΩ, and

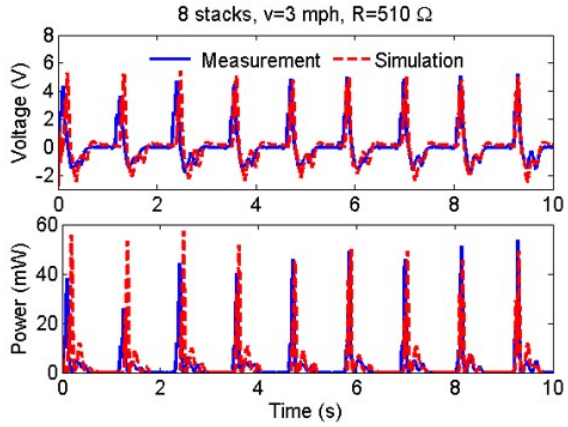

Figure 2.16: Measured and simulated voltage and power (8 stacks, v=3 mph (4.8 km/h), R=510 Ω)..

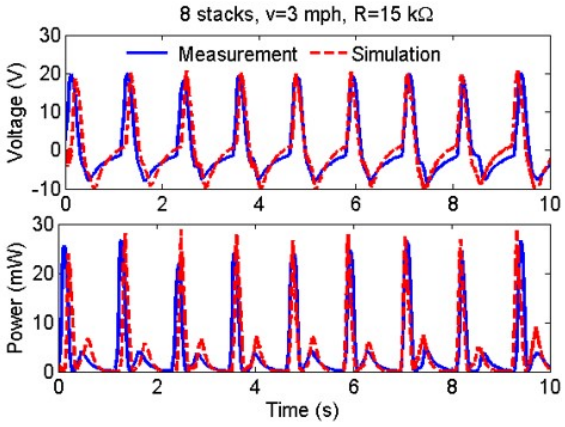

Figure 2.17: Measured and simulated voltage and power (8 stacks, v=3 mph (4.8 km/h), R=15 kΩ.

Table 2.2: Comparison between the measured and simulated RMS voltages

Resistance	Velocity					
	2.5 mph (4.0 km/h)		3.0 mph (4.8 km/h)		3.5 mph (5.6 km/h)	
	Ex. (V)	Sim. (V)	Ex. (V)	Sim. (V)	Ex. (V)	Sim. (V)
510 Ω	1.05	1.08	1.14	1.24	1.22	1.56
1100 Ω	2.09	2.06	2.40	2.32	2.26	2.90
5100 Ω	5.46	5.42	5.81	5.84	6.07	6.90
9000 Ω	6.01	6.57	6.41	6.94	7.50	8.01
150000 Ω	6.14	7.16	7.32	7.49	7.68	8.52

* Ex. and Sim. denote the experiment and simulation results, respectively.

15 kΩ are given in Table 2.2. It is observed that the simulations are in good accordance with the experiments for different walking speeds. The maximum average power outputs are around 6 mW, 7 mW, and 9 mW at the three walking speeds, respectively, which exhibits that the RMS voltage and average power augment as the walking speed increases. This is attributed to the fact that both the amplitude and frequency of the dynamic force on the aluminum plates of the harvester increase along with the walking speed. It is found that the optimal resistance corresponding to the maximum power output is around 3000 Ω, and there is no evident difference at the three walking speeds.

The measured and simulated instantaneous voltage and power outputs of the harvester

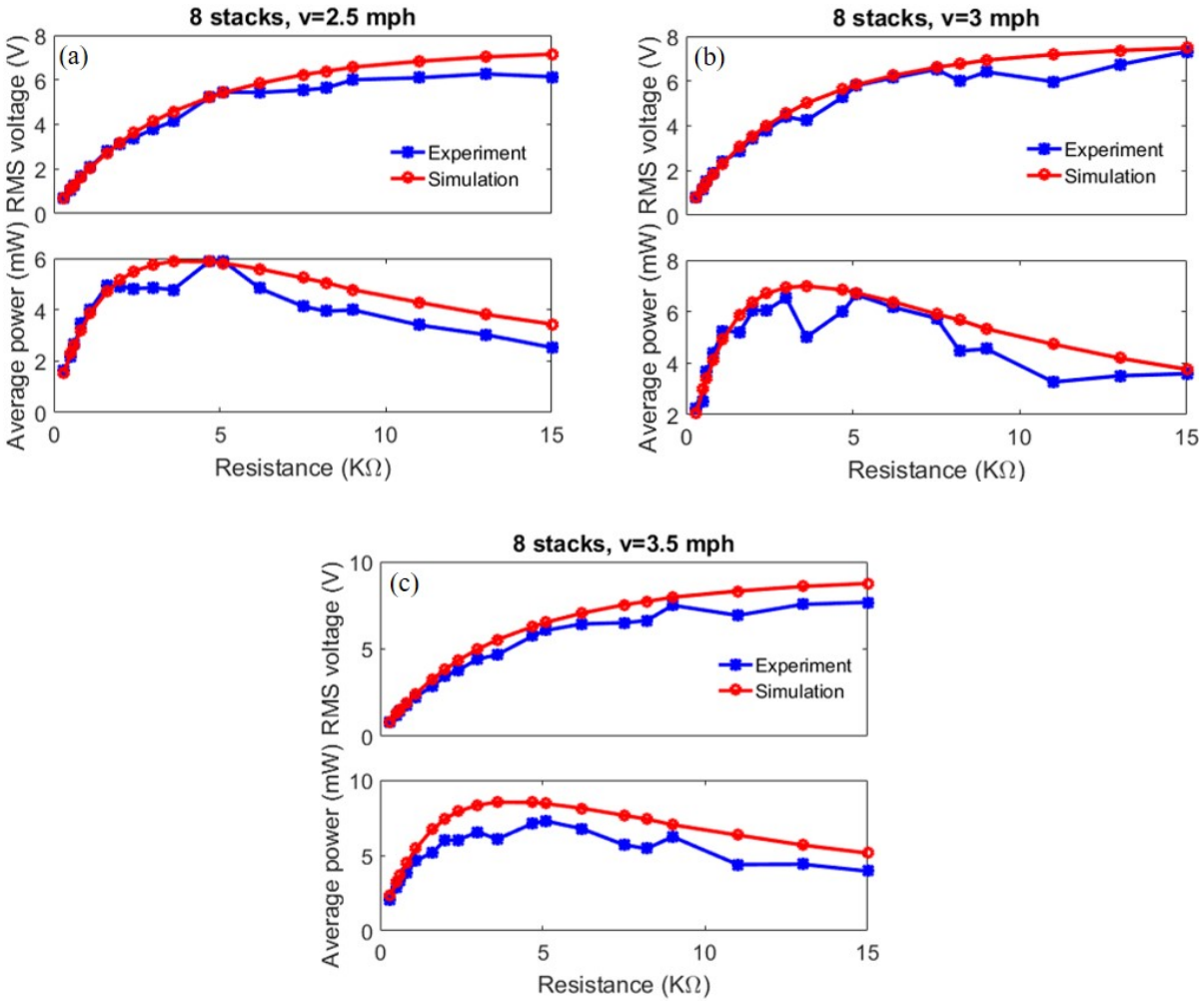

Figure 2.18: Measured and simulated RMS voltage and average power of the harvester with eight PZT stacks at walking speed of (a) 2.5 mph (4.0 km/h), (b) 3 mph (4.8 km/h), and (c) 3.5 mph (5.6 km/h).

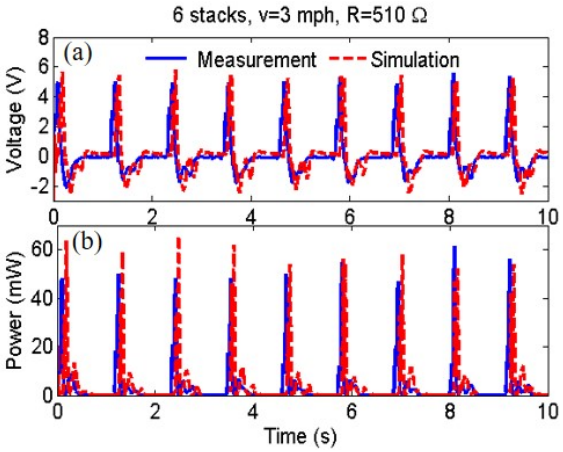

Figure 2.19: Measured and simulated voltage and power from the harvester (6 stacks, v=3.0 mph (4.8 km/h), R=510 Ω).

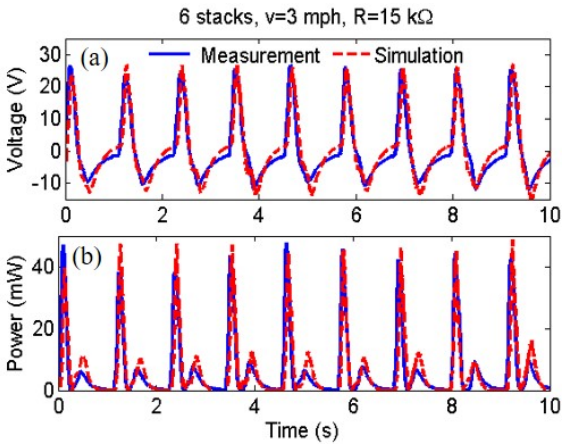

Figure 2.20: Measured and simulated voltage and power from the harvester (6 stacks, v=3.0 mph (4.8 km/h), R=15 kΩ).

with six piezoelectric stacks and frames at walking speed of 3.0 mph (4.8 km/h) and the external electrical resistance of 510 Ω are depicted in Fig. 2.19 (a) and (b), respectively. The peaks of the instantaneous voltage and power are around 6 V and 60 mW, both of which are slightly greater than those of the harvester with eight stacks. Similarly, Fig. 2.20 (a) and (b) plot the instant voltage and power outputs of the harvester with six stacks under the electrical resistance of 15 kΩ, whose peaks are 27 V and 48 mW. The comparison between Fig. 2.20 and Fig. 2.17 suggests that both the voltage and power outputs of the harvester with six stacks are higher than those of the harvester with eight stacks at the same walking speed and external resistance. These findings match with the previous analysis that fewer stacks in the harvester will result in large input force to each piezoelectric stack and consequently, a large power output.

The RMS voltage and average power of the harvester with six piezoelectric stacks are plotted in Fig. 2.21 (a) and (b) for the walking speeds of 2.5 mph (4.0 km/h) and 3.0 mph (4.8 km/h), respectively. It can be seen that both the RMS voltage and average power predicted by the numerical model are very close to the experimental results. The maximum average

power outputs are 8 mW/shoe and 9 mW/shoe for the two different walking speeds, and the corresponding optimal resistive load is around 3600 Ω. According to [55], the delivered power is around 70% of the generated power, which means the generated power are around 11.4 mW/shoe and 12.9 mW/shoe. The harvester produces 33% and 29% more power than those from the harvester with eight stacks at the walking speeds of 2.5 mph (4.0 km/h) and 3.0 mph (4.8 km/h). The simulated RMS voltage and average power of the harvester with six piezoelectric stacks at 3.5 mph (5.6 km/h) are plotted in Fig. 2.21 (c). The maximum average power is about 14 mW, which is 56% more than that of the harvester with eight piezoelectric stacks.

The validated numerical model can be used to simulate the harvesters' voltage and power outputs with different numbers of piezoelectric stacks. The harvester with four piezoelectric stacks is simulated for the three different working speeds considered previously. The same force amplification factor obtained in the previous design is assumed to be achievable in the following simulations. The simulated RMS voltage and average power from the harvester with four piezoelectric stacks are presented in Fig. 2.22 (a) and (b), respectively. Both the RMS voltage and average power increase along with the increment of the walking speed over different external resistances. The maximum average power outputs at the three walking speeds are around 12 mW, 14 mW, and 20 mW, which are more than two times of those of the harvester with eight piezoelectric stacks. Although the results show that the harvester with fewer piezoelectric stacks could produce larger average power, it is worth mentioning that the design of the frame would become more challenging due to the larger input force. In addition, only one piezoelectric harvester is considered in one of a pair of boots. Therefore, the total maximum average power output would be up to 40 mW if two harvesters with four piezoelectric stacks are installed a pair of boots.

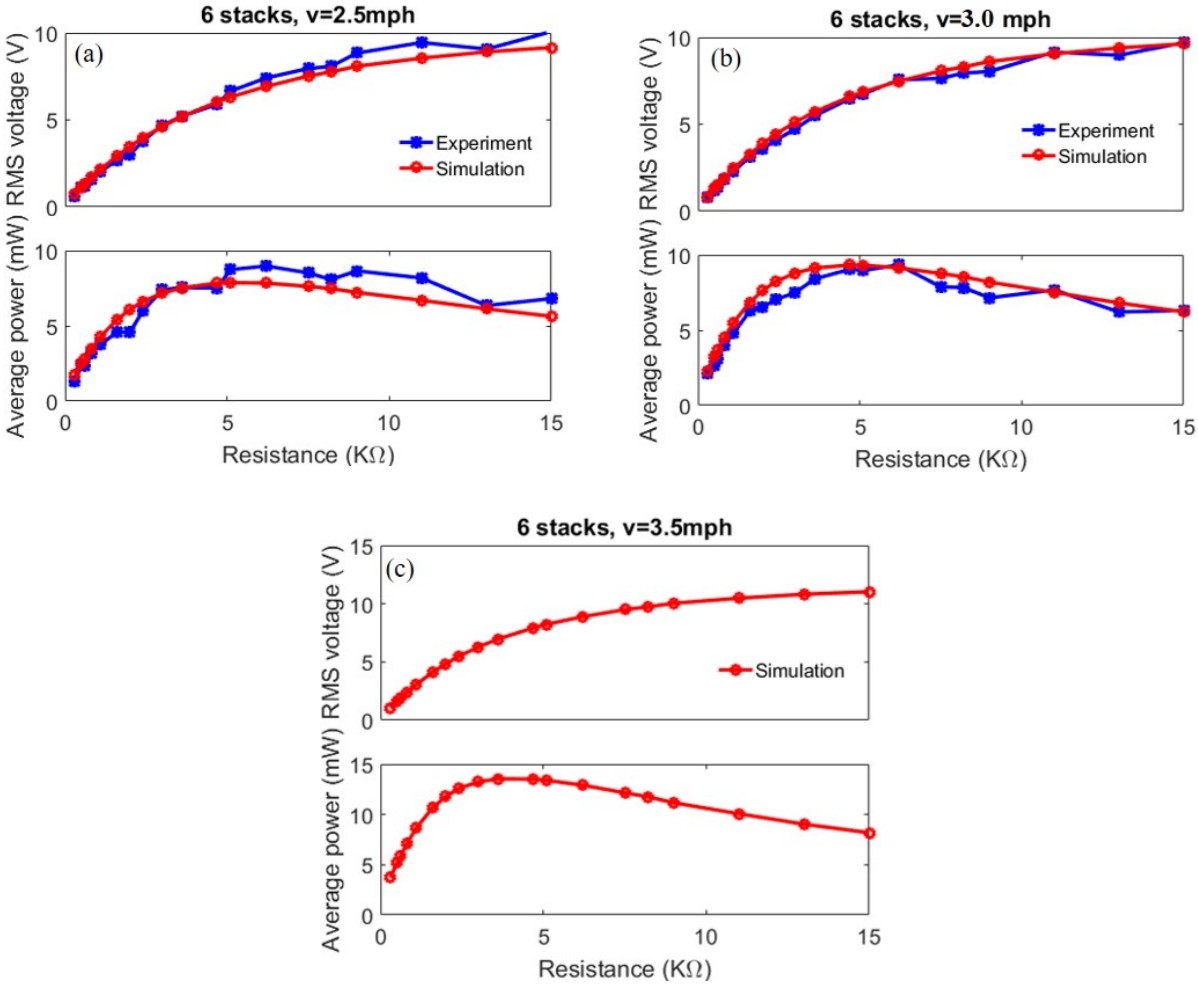

Figure 2.21: RMS voltage and average power of the harvester with six PZT stacks at walking speeds of (a) 2.5 mph (4.0 km/h), (b) 3.0 mph (4.8 km/h), and (c) 3.5 mph (5.6 km/h).

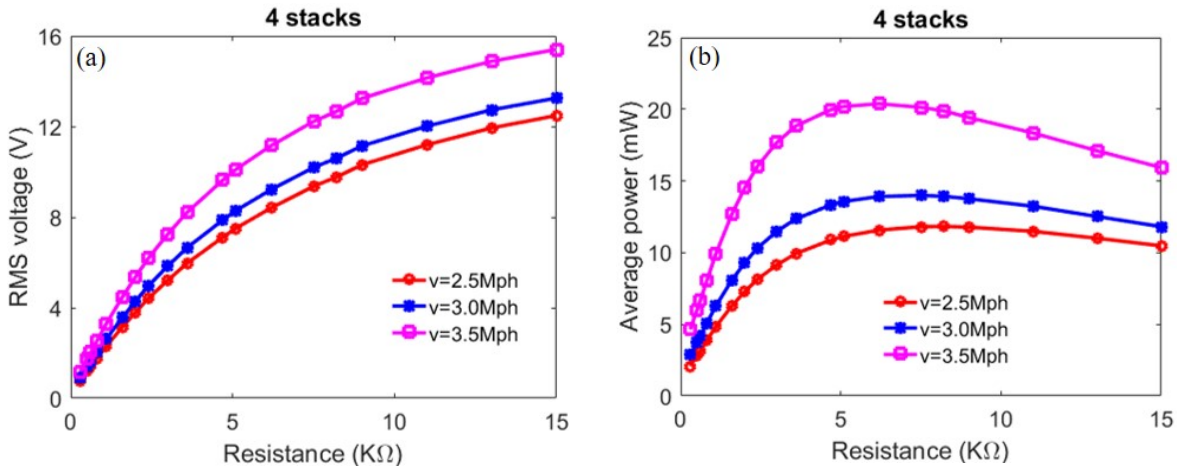

Figure 2.22: Simulation results of the harvester with four stacks at walking speeds of 2.5 mph (4.0 km/h),3.0 mph (4.8 km/h), and 3.5 mph (5.6 km/h): (a) RMS voltage, (b) average power.

2.8 Discussion

As a preliminary attempt and proof of the concept, this study takes a boot (Belleville 790 ST, 790ST-9, TacticalGear.com) as the object to perform the design, integration, and test of the footwear piezoelectric energy harvester with a single-stage force amplifier. This is mainly because the boot has a relatively large space in the heel to facilitate the design and integration of the harvester compared with most generic shoes. A similar design can also be applied to a sports shoe and generic shoes with smaller piezoelectric stacks (for example, the commercially available piezoelectric stack of 5 mm×5 mm×20 mm) and force amplification frames. It will certainly bring more challenges to design and manufacture a smaller prototype under the constrain of the very limited space in the heel of an ordinary shoe. Nonetheless, there is a potential to improve the power output by exploiting the piezoelectric material more sufficiently with smaller piezoelectric stacks. The stress in a piezoelectric stack can be greatly increased by a smaller cross-sectional area, as a result of which larger power output can be achieved. For simplicity, an external resistive load is considered in the current study.

However, a power storage unit and management circuit must be included to safely power sensors and devices. It is reported that the most commonly employed wireless communication standards in body area networks (Zigbee) have a maximum power consumption of 30 mW when the chip is on [110]. This means the proposed footwear harvester could provide enough power for a standard body area network.

The power output of the presented footwear energy harvester depends on different conditions except for the walking speed, for instance, the road condition and wearer's weight. The prototype is only tested on a treadmill with a very even surface that cannot well represent the real road condition. However, as a scientific measurement tool, a treadmill provides controllable walking conditions to get results that are more accurate. Practically, more power could be generated from a rough road condition since a large ground reaction force can be induced by an uneven road surface. Furthermore, the wearer's weight can also have a considerable influence on the power output. Wearers with heavier weight generally have large ground reaction forces at heels that can result in higher power outputs. The power output can be improved by designing and integrating a two-stage force amplification frame into the harvester instead of the current single-stage frame. In addition, piezoelectric materials with large d_{33} constants, such as, PMN-PT and PZN-PT crystals [111], could significantly enhance the mechanical-to-electrical energy conversion in future.

2.9 Chapter summary

A piezoelectric footwear energy harvester with a force amplification mechanism is designed, optimized, modeled, and experimentally tested in this chapter. The harvester consists of several piezoelectric stacks within force amplification frames and two heel-shaped aluminum plates. The dynamic forces at the heel are measured at different walking speeds to obtain

the input force for the design of the force amplification frames and numerical simulations. A parameterized finite element model is established to optimize the force amplification frame using the biography-based optimization algorithm. A simplified analytical model is developed to predict the voltage outputs at different walking speeds and external resistive loads. Two prototypes of the harvesters, respectively including eight and six piezoelectric stacks, are manufactured, assembled, and integrated into the heel of a 9-size Belleville boot (26 cm in length) for treadmill tests. The total weight of the boot with a six piezoelectric stack harvester is 1086 g, 124 g more than the original boot. The numerical simulations have good agreements with the experimental results, proving that the simplified analytical model can reliably predict the electrical outputs of the proposed foot wearable harvester. The maximum average power outputs (delivered to matched resistive load) of the harvester with eight stacks are 6 mW/shoe, 7 mW/shoe, and 9 mW/shoe at the walking speeds of 2.5 mph (4.0 km/h), 3.0 mph (4.8 km/h) and 3.5 mph (5.6 km/h), respectively. In comparison, the harvester with six stacks could produce 8 mW/shoe, 9 mW/shoe, and 14 mW/shoe at the three walking speeds, which are 33%, 29%, and 56% more than those of the harvester with eight stacks, respectively. For the harvester with four stacks, the numerically predicted maximum average power outputs at the three walking speeds of 2.5 mph (4.0 km/h), 3.0 mph (4.8 km/h) and 3.5 mph (5.6 km/h) are 12 mW/shoe, 14 mW/shoe, and 20 mW/shoe. Results also show that harvester with fewer piezoelectric stacks could generate more power due to large force input to each stack.

Chapter 3

Material equivalence, finite element modeling, and validation of the piezoelectric footwear energy harvester

3.1 Chapter introduction

Many models have been developed to characterize the electromechanical coupling dynamic behavior of multilayered piezoelectric stacks, including the single degree-of-model (SDOF) model [45, 109], distributed parameter model [42, 112], transfer matrix (TM) model [113], and FE model [95]. In chapter two, the piezoelectric footwear energy harvester composed of multiple piezoelectric stacks inset in the single-stage force amplification frames (FAFs) was modeled using a simplified SDOF model. The simplified SDOF model only considered the dynamics of the piezoelectric stack without taking the force amplification frame (FAF) into account, which is of importance to the energy harvesting performance. Therefore, the SDOF model cannot be used to investigate the effect of the geometric parameters of the FAF on

the power output of the harvester.

The finite element (FE) method has been used to solve piezoelectric electromechanical coupling problems. Tolliver et al [95] built a FE model of a piezoelectric multilayer-stacked hybrid transduction consisting of two components operating in d_{33} and d_{31} modes, respectively. Yang and Tang [114] developed a FE model of a piezoelectric cantilever harvester to identify the parameters for the equivalent circuit model. A FE model of a nonlinear piezoelectric energy harvester involving magnetic interaction was established in ANSYS and experimentally validated [115]. Recently, a parameter study of a trident-shaped multimodal piezoelectric energy harvester was conducted based on the FE model [116]. Finite element analysis was also used to investigate bi-stable piezoelectric energy harvesters [93, 117]. Nevertheless, it is impractical to build a FE model for the piezoelectric stack composed of hundreds of thin piezoelectric films of thickness, like 0.1 mm. This is because the piezoelectric films are too thin to mesh, or even if they can mesh, that will consequently result in a huge computational burden due to a large number of nodes and elements.

The contributions and novelty of this chapter are threefold. First, a material equivalent model is developed to simplify the multilayered piezoelectric stack into an equivalent bulk to address the mesh problem in FE modeling. Then, a parameterized one-fourth FE model of the piezoelectric footwear energy harvester is established to expedite the dynamic analysis and experimentally validated by taking advantage of the symmetry in geometries, load, and boundary conditions. The numerical simulations agree well with the experimental results, which indicates that the proposed material equivalent model and the FE model have good accuracy. The effect of the FAF's geometries on the power output of the footwear energy harvester is investigated. The material equivalent model proposed in this study also provides a general way for FE modeling of multilayered piezoelectric stacks. The experimentally achieved peak power outputs of the piezoelectric footwear energy harvester at the walking

speeds of 2.5 mph (4.0 km/h) and 3.0 mph (4.8 km/h) are 83.2 mW and 84.8 mW, and the average power outputs are 8.5 mW and 9.3 mW, respectively.

3.2 Material equivalence

The multilayer piezoelectric stack is simplified as an equivalent bulk in this study to solve the meshing problem associated with the thin piezoelectric films. The equivalent material properties of the piezoelectric bulk and the equivalent resistance of the external resistor are derived from the simplified SDOF model of the multilayer piezoelectric stack. The piezoelectric footwear energy harvester, which consists of n_s multilayer piezoelectric stacks electronically connected in parallel with an external resistor R, was modeled as a SDOF system. The equations of motion of the system, including both the mechanical and electrical equations, are given in Eqs. 2.9 and 2.13. Assuming the total active length of the piezoelectric stack is $L_p = nt_p$, the capacitance of the multilayer piezoelectric stack in Eq. 2.13 can be rewritten as

$$C_p = \frac{n^2 \varepsilon_{33}^T A}{L_p} = \frac{\bar{\varepsilon}_{33} A}{L_p} = \bar{C}_p \tag{3.1}$$

where $\bar{\varepsilon}_{33} = n^2 \varepsilon_{33}^T$ and $\bar{C}_p$ can be taken as the equivalent dielectric constant and capacitance of the piezoelectric bulk, respectively. Defining the equivalent piezoelectric charge constant of the piezoelectric bulk as $\bar{d}_{33} = nd_{33}$ and the equivalent resistance in the circuit $\bar{R} = n_s R$, Eqs. 2.9 and 2.13 can be converted into

$$\ddot{x}(t) + \omega_n^2 x(t) - \omega_n^2 \bar{d}_{33} v(t) = \frac{\alpha}{m} F_{in}(t) \tag{3.2}$$

$$\dot{v}(t) + \frac{v(t)}{\bar{R}\bar{C}_p} + \frac{m\omega_n^2 \bar{d}_{33}}{\bar{C}_p} \dot{x}(t) = 0 \tag{3.3}$$

where $F_{in}(t) = \frac{F(t)}{n_s}$ is the dynamic force reallocated to each FAF by the aluminum plates. Eqs.3.2 and 3.3 are substantially the governing equations of motion of the piezoelectric bulk in Fig. 3.1. From the above analysis, the equivalent material properties of the piezoelectric bulk and the equivalent resistance are obtained from the multilayer piezoelectric stack and summarized in Fig. 3.1. These equivalent material properties, as well as the equivalent resistance, will be used to create the electromechanical coupling FE model.

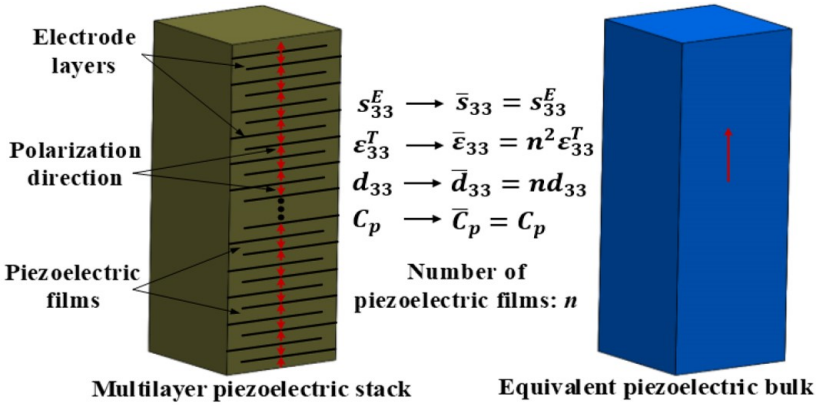

Figure 3.1: Equivalent piezoelectric bulk model. $s_{33}^E, \varepsilon_{33}^T, d_{33}$, and C_p are the compliant constant, dielectric constant, charge constant and capacitance of the piezoelectric stack. $\bar{s}_{33}^E, \bar{\varepsilon}_{33}, \bar{d}_{33}$, and C_p are the equivalent compliant constant, dielectric constant, charge constant and capacitance of the piezoelectric bulk.

3.3 Finite element modeling and dynamic analysis

A complete FE model of the whole PBEH can be established in available commercial software packages, such as Ansys Multiphysics, Abaqus, and Comsol. However, performing dynamic analysis on a complete FE model could be time-consuming and thus inefficient for parameter analysis. To reduce the computational cost, only one unit of the piezoelectric stack and FAF is taken into account in the full FE model. Static analysis is performed on the full model to design an optimal FAF. To further simplify the modeling, a one-fourth FE model

is developed by exploiting the geometry, boundary, and load symmetries. The multilayer piezoelectric stack is modeled as a bulk based on the material equivalence. The static analysis is also carried out to the one-fourth model with the optimal parameters to validate the mechanical characteristics with the full model. Dynamic analysis is conducted to the one-fourth FE model over varying external resistors, and results are compared with experimental measurements. A parametric study is carried out based on the one-fourth FE model to investigate the effect of the geometric dimensions of the FAF on the power output.

3.3.1 Full FE model

A full FE model of the transducer unit including the piezoelectric stack and the FAF is developed and programmed based on the APDL (ANSYS Parametric Design Language) in ANSYS [107] and illustrated in Fig. 3.2. The FAF is modeled by the three-dimensional (3D) tetrahedral solid structural element (Solid72). This element has four nodes and six degrees of freedom (DOFs) at each node and thus can consider the irregular meshes of the fillets at corners and abrupt changes in sections. The equivalent piezoelectric bulk is modeled by the 3D tetrahedral coupled-field solid element (Solid98). This element has ten nodes and an additional DOF of electric potential at each node except for the three translational DOFs. The external resistor is simulated by the Circu94 element, which is a two-terminal element with one voltage potential DOF at each node and could interface with the piezoelectric element. ANSYS provides users with the piezoelectric material model that can be specified by inputting the piezoelectric material properties. Since the piezoelectric stack only works in d_{33} mode [42, 55], the other ineffective piezoelectric constants are assigned to zeros in the material model. The force transferred to the FAF is applied by the equivalent node forces at the top surface of the middle lock. The fixed boundary condition is applied to the bottom surface of the middle block.

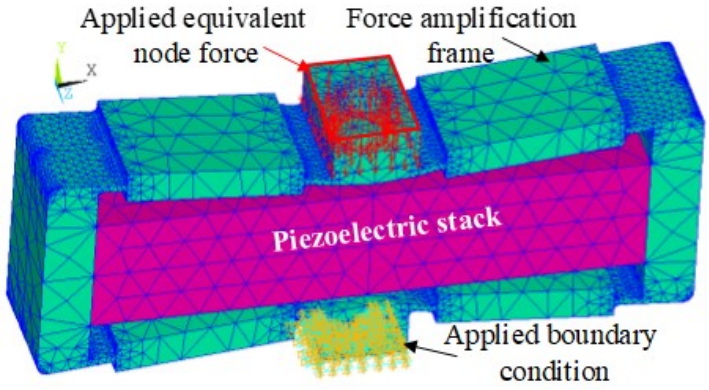

Figure 3.2: The FE model of the transducer unit with the applied equivalent node loads and boundary condition.

3.3.2 Symmetric FE model

The full FE model still has a large number of elements and DOFs, which result in a significant computational burden in dynamic analysis. To further simplify the model and promote the computation, a one-fourth symmetric FE model, as shown in Fig. 4, is developed based on the symmetries in geometry, load, and boundary conditions. The sum of the applied equivalent node forces over the top surface of the middle block is also a quarter of the input force of the full model, which equals to $\frac{F_{in}(t)}{4}$. Symmetric boundary conditions are applied to the symmetric surface so that the frame can only deform along the vertical direction. It should be noted that the symmetric boundary conditions at the symmetric plane of $z = 0$ are not plotted in Fig. 3.3 to make the picture clear. Again, the fixed boundary conditions are applied to the bottom surface of the other middle block. The voltage DOFs of the piezoelectric elements at the two ends are coupled together such that the voltages of all the nodes at each end are the same. Zero boundary conditions are exerted to the voltage DOFs of the nodes at the left end of the piezoelectric bulk to model the zero reference potential point of the ground. The resistor is directly connected to the two ends of the piezoelectric bulk. It is noteworthy that the input value of the external electrical resistance

in the symmetric FE model should be the equivalent resistance $\bar{R}$ derived from the material equivalence method. The automatic (smart) element sizing is used to mesh the model by

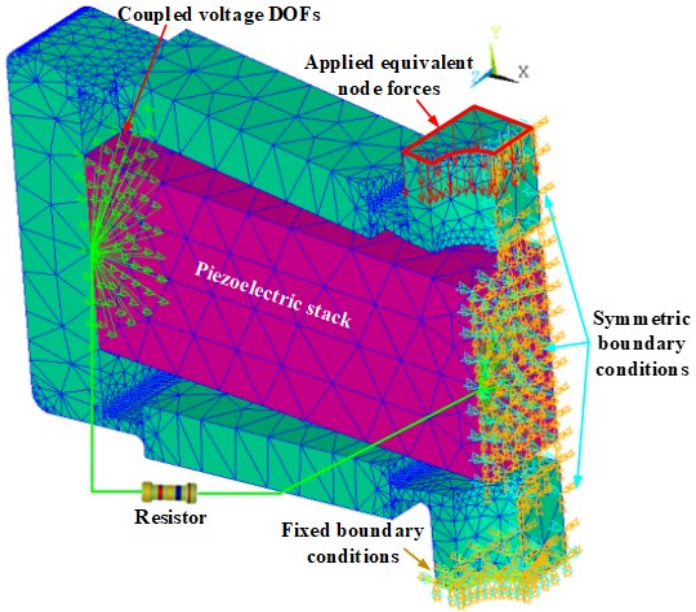

Figure 3.3: The proposed one-fourth symmetric FE model with the applied equivalent node loads and boundary conditions.

setting the overall element size level. This mesh method enables a finer mesh at corners and abrupt changes of cross-sections. The solution convergence test over the size level of the element is conducted to balance the trade-off between the accuracy and computational cost. The developed symmetric FE model is parameterized and coded in the ANSYS APDL. Different from the simplified single DOF model in [45], the symmetric FE model considers the dynamics of the FAF and thus could be used for parametric study by greatly facilitating the dynamic analysis to investigate the influence of the FAF on the performance of the harvester.

3.3.3 Static analysis

Static analysis is firstly performed to the proposed one-fourth symmetric FE model to validate the model accuracy by comparing it with the results obtained from the full model. The Von-Mises stress distributions in the FAF is presented in Fig. 3.4. The maximum stress is around 449 MPa, which is far less than the yield stress of the material. The maximum stress locates at the insides of the junctions between the thick beams and the thin beams. The normal stress in the piezoelectric stack is around 17.3 MPa. By integrating the normal stress over the cross-section of the piezoelectric stack, the force transferred to the inner piezoelectric stack is obtained as F_{out}= 846.8 N. Therefore, the force amplification factor α of the FAF is computed as 8.5. The stress distributions in the FAF and the piezoelectric bulk, as well as the force amplification factor attained from the symmetric FE model agree well with those of the full FE model, as shown in Table 3.1. This validates that the proposed symmetric FE model has good accuracy in representing the full model with the significant benefit in the efficiency of the dynamic analysis on account of the reduced number of elements and DOFs.

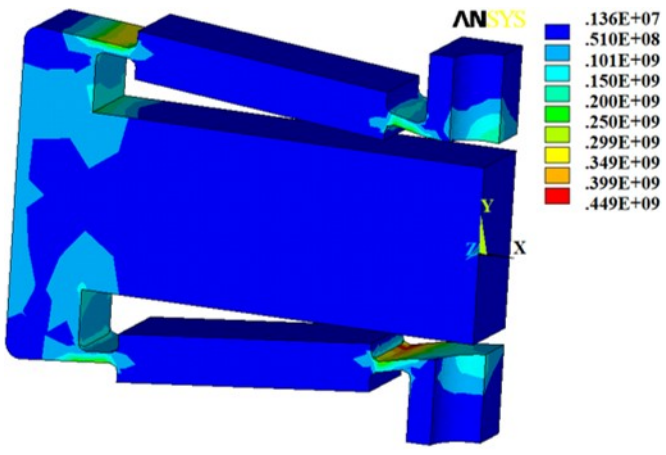

Figure 3.4: Stress distribution in the force amplification frame.

Table 3.1: Comparison of the results from the full model and symmetric model.

Model	Max. stress in the FAF (MPa)	Normal stress in the PZT-stack (MPa)	Force amplification factor α
Full model[45]	450	17.3	8.5
One-fourth model	449	17.3	8.5

3.3.4 Dynamic analysis and energy conversion efficiency

Transient dynamic analysis is performed on the one-fourth symmetric FE model with a closed-loop circuit connected to the external resistor. The input material constants of the piezoelectric bulk are the equivalent material properties obtained by the material equivalent method presented in Section 3.2. The ANSYS build-in Newmark integration method is used in the transient dynamic analysis, and the two integration parameters are set to 0.5 and 0.25. The mechanical damping is considered by assigning a damping ratio of 0.015. The input dynamic forces are measured at the heel by treadmill experiments under different walking speeds, which are presented in chapter one. It should be clarified that the experiments for the dynamic force measurements are performed separately from the tests of the harvester by keeping the experimental conditions as close as possible. The sampling period of the dynamic force is 0.02, and the total time length is T_s=10 s.

Simulations are performed to walking speeds of 2.0 mph (3.2 km/h), 2.5 mph (4.0 km/h), 3.0 mph (4.8 km/h), 4.0 mph (6.4 km/h), and 6.0 mph (9.7 km/h) to investigate the influence of walking speed on the average power output and optimal resistance. The prototype is only tested at the two walking speeds of 2.5 mph (4.0 km/h) and 3.0 mph (4.8 km/h) to prevent the frames from breaking due to large force inputs. High walking speeds could result in a very large impact force at the heel in practice, which may be far beyond the design input force of the frame. Based on the assumption that the reaction force at the heel is evenly allocated to each frame by the aluminum plates, the input dynamic reaction

force to the symmetric FE model is actually the measured reaction force firstly divided by the number of the frames included in the harvester and then four due to the load symmetry.

The voltage outputs of the piezoelectric footwear energy harvester are simulated over different external resistive loads of R= 300 Ω, 1100 Ω, 1600 Ω, 2400 Ω, 3600 Ω, 5100 Ω, 6200 Ω, 7500 Ω, 9000 Ω, 11000 Ω, 13000 Ω, 15000 Ω at each walking speed. The actual resistance used in the symmetric FE model for the dynamic analysis is $4n_sR$ due to the material equivalence and symmetry. To evaluate the performace of the harvester, the instant and average power outputs can be calculated from the voltage responses by Eqs.2.14 and 2.15.

To evaluate the mechanical-to-electrical energy conversion efficiency of the proposed piezoelectric footwear energy harvester, the input mechanical power to the harvester can be estimated by [118]

$$P_m = W_b d_h f_w \tag{3.4}$$

where P_m is the mechanical power generated at the heel as human walking. W_b is the body-weight of the wearer. d_h is the heel's fall distance, which is also the vertical deformation of the harvester that could be calculated from the FE analysis. f_w is the walking frequency related to the walking speed. Therefore, the mechanical-to-electrical energy conversion efficiency of the footwear energy harvester can be calculated by

$$\eta_e = \frac{\bar{P}}{P_m} \times 100\% \tag{3.5}$$

3.4 Numerical results and validation

This section compares the FE numerical results under different walking speeds and external resistive loads with experimental results and single DOF model predictions. The instantaneous voltage and power responses of the footwear energy harvester at the walking speeds of 2.5 mph (4.0 km/h) and 3 mph (4.8 km/h) are plotted in Fig. 3.5 (a) and (b) for the chosen external resistive loads of R =300 Ω, 5100 Ω, and 15 kΩ. These three resistive loads are selected to represent small, optimal, and large resistance. To validate the one-fourth symmetric FE model, the simulation results from the full FE model are also presented in Fig. 3.5 (a) and (b). Good agreements between the symmetric and full FE models can be observed. The transient power outputs are calculated from the measured and simulated voltage responses and plotted at the left side of the voltage responses. The experimentally achieved peak voltage and power under the walking speed of 2.5 mph (4.0 km/h) are 2.8 V, 20.6 V, 26.4 V, and 26.1 mW, 83.2 mW, 46.5 mW at the three resistors, respectively. 3.4V, 20.8 V, 26.8 V, and 39.4 mW, 84.8 mW, and 47.9 mW are obtained at 3 mph (4.8 km/h). The numerical results simulated from the symmetric FE model agree well with the experimental measurements and single DOF model predictions. This suggests that the proposed symmetric FE model could accurately simulate the electromechanical coupling behavior of the harvester. The simplified equivalent material model of the piezoelectric bulk from the single DOF model of the multilayer piezoelectric stack is correct.

Discrepancies between the FE simulations, experimental results, and the single DOF model predictions are still observable in Fig. 3.5. This can be attributed to the fact that the input dynamic forces in the FE simulations are not synchronously measured from the same experiments that the voltage responses are measured. In other words, the inputs of the FE model are not exactly the same with the real cases, because the reaction dynamic force at the heel may always vary in repeated tests even for the same test subject and experimental

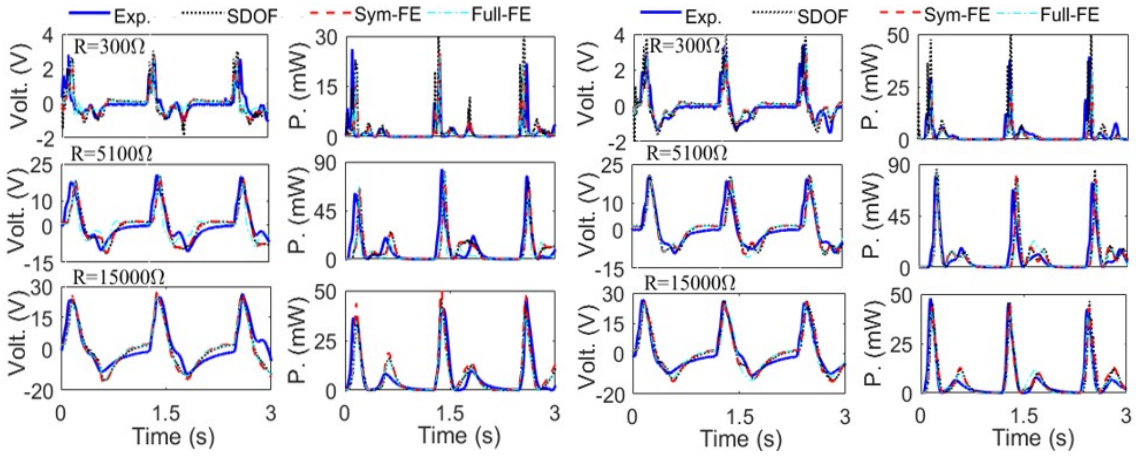

(a) v=2.5 mph (4.0 km/h), R=300 Ω, 5100 Ω and 15 kΩ.

(b) v=3 mph (4.8 km/h), R=300 Ω, 5100 Ω and 15 kΩ.

Figure 3.5: Instantaneous voltage and power responses of the footwear energy harvester.

setup. In addition, numerical model error due to the mesh size and simplifications, as well as the material error, also results in the differences between numerical predictions and measurements. Nevertheless, the symmetric FE model maintains an overall consistency with the experiments and gives dependable predictions at different walking speeds and various external resistive loads.

To evaluate the performance of the developed symmetric FE model, the root mean square (RMS) voltage and average power at varying external resistive loads are calculated from the simulated instantaneous voltage responses and compared with experimental and single DOF model results. Fig. 3.6 (a) and (b) plot the RMS voltage and average power under the walking speeds of 2.5 mph (4.0 km/h) and 3.0 mph (4.8 km/h) over varying resistance, respectively. It is shown that the RMS voltage and average power simulated from the symmetric FE model are in accordance with those calculated from the experimental measurements and the single DOF model predictions. This further confirms the symmetric FE model has good accuracy in the prediction of the dynamic behavior of the PBEH over

varying resistance. The RMS voltage and average power increase along with the walking speed. The maximum average power at the two walking speeds is around 8.5 mW and 9.3 mW over the optimal resistance around 5100 Ω. The corresponding mechanical-to-electrical energy conversion efficiencies calculated using Eq. 3.5 are 4.5% and 4.7%. The vertical displacement of the harvester obtained from the FE analysis is around d_h=0.28 mm. The

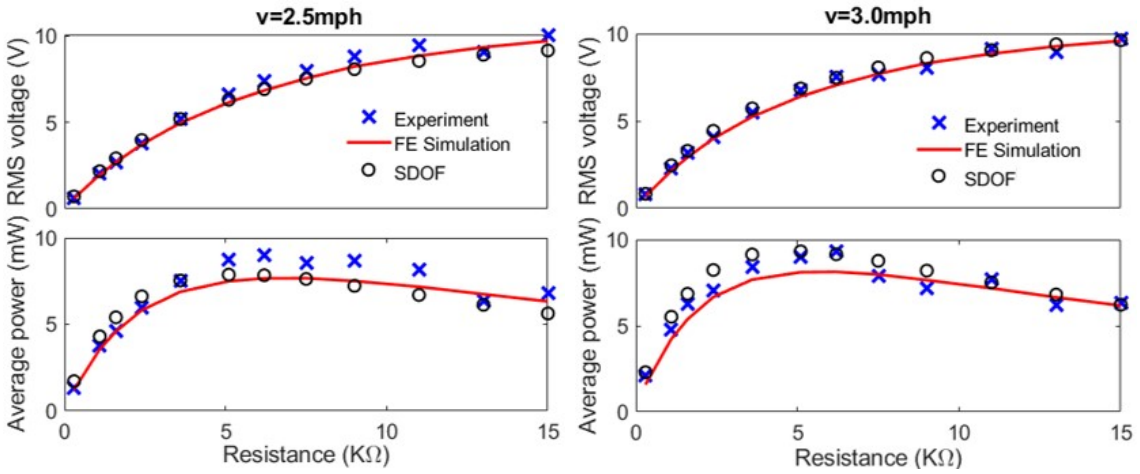

(a) v=2.5 mph (4.0 km/h). (b) v=3 mph (4.8 km/h).

Figure 3.6: RMS voltage and average power of the footwear energy harvester over various resistive loads under the walking speed of 2.5 mph (4.0 km/h) and 3.0 mph (4.8 km/h).

energy generation performance of the footwear energy harvester is compared with the existing results that have experimentally achieved by footfall piezoelectric energy harvesters in Table 3.2. It shows that the proposed piezoelectric footwear energy harvester has a larger power output and a larger size. It should be noted that the size of the footwear energy harvester is actually designed according to the heel size of the boot with the purpose of collecting all the distributed force under the heel as human walking. The efficiency of the boot harvester is comparable with the work in Ref. [46], but much lower than the one reported in [47].

The average power simulated from both the symmetric FE and single DOF models over different walking speeds are plotted together with the optimal resistance in Fig. 3.7(a), which shows that the average power output increases, and the optimal resistance decreases along

Table 3.2: Performance comparison with the existing results

Reference	Material	Average power (mW)	Size (mm^2or mm^3)	Efficiency (%)
Kymissis et al.[46]	PVDF (3-1)	1.1@1 Hz	100×(5∼8)×2.45	0.5
Kymissis et al.[46]	PZT (3-1)	1.8@1 Hz	7×7(insole)	5
Shenck and Paradiso[47]	PZT (3-1)	8.4@ 0.9Hz	50×85(insole)	17.6
Fan et al.[49]	PZT (3-1)	0.35@8 km/h	70×40×0.6	-
Zhao and You[8]	PVDF (3-1)	1.0@ 1Hz	80×50 (insole)	-
Kuang et al[50]	PZT (3-1)	2.5@4.8 km/h	52×30×12.7	-
Proposed	PZT (3-3)	9.3@4.8 km/h (0.9Hz)	68×94×24	4.7

with the walking speed. The average power output is up to 34.7 mW at 6.0 mph (9.7 km/h) with a mechanical-to-electrical power conversion efficiency of 10.8%. This is mainly because both the amplitude and frequency of the dynamic force at the heel increases along with the walking speed, as shown in Fig. 3.7 (b). The data presented in Fig. 3.7 (b) are the average maximal heel-ground reaction forces at the heel normalized to the gravity of the wearer. The error bars show the measurements for ten periods for each speed. The maximal heel-ground reaction force is taken as the peak-to-peak force in one period, as illustrated in the right corner of Fig. 3.7 (b). It should be mentioned that the appearance of the negative force in the measurement is an artificial effect of the built-in high-pass filter of the dynamic analyzer. Among the time interval that the heel lifts from the ground, but has not yet hit the ground again, the reaction force should be zero. The high-pass filter filters out the DC component in the signal and shifts the force measurement. The walking frequency shows an almost linear relationship with the walking speed. However, the maximal heel-ground reaction force increases quickly at first and then slowly as the walking speed becomes very large.

3.5 Parametric study

The design of the FAF is of vital importance for power conversion efficacy. An ideal FAF should have the features of a large force amplification factor and enough load capacity to

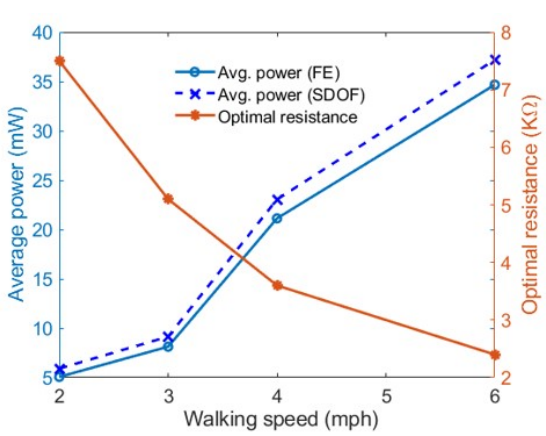

(a) Average power and optimal resistance.

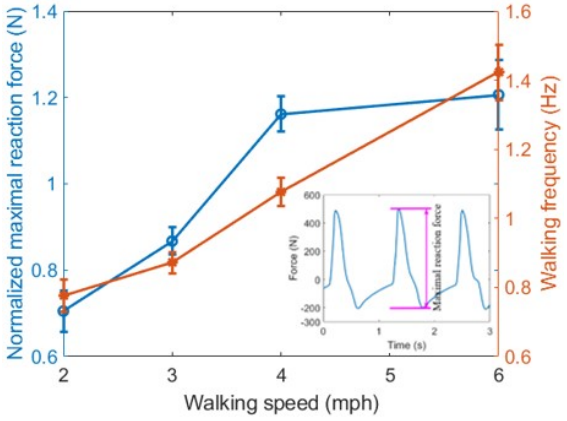

(b) Normalized maximal heel-ground reaction forces and walking frequencies.

Figure 3.7: Average power, optimal resistance, normalized maximal heel-ground reaction force, and walking frequency vs. walking speed.

operate safely under a varying dynamic force environment. These features not only depend on the material selection and machining processing but also are determined by the geometric dimensions. Therefore, parametric studies are carried out based on the validated symmetric FE-model to investigate the influence of the geometries of the FAF on the power generation performance. The optimal parameters of the FAF presented in Table 2.1 are obtained under specific geometric and stress constraints, which means they are practical under certain given conditions but not the globally optimal solutions. The parametric study could help identify the influence of the key parameters of the FAF on the power generation performance. Four key parameters of the FAF, respectively, the tilt angle θ of the beams, the thickness t_1, length L_1 of the thin beam, and the thickness t_e of the end block, are considered in the parametric study.

The geometric dimensions in Table 2.1 are set as the reference for the parametric study. The dynamic reaction force at the heel measured at 3.0 mph (4.8 km/h) is used as input since the average human walking speed is around 3.0 mph. The resistance of the external resistor is chosen as 5100 Ω, which is close to the optimal resistance. For each of the four

parameters of interest, the instantaneous voltage responses of the model with varying values of the parameters are derived while other parameters remain unchanged. The RMS voltage and average power are calculated and plotted versus each varying parameter, as shown in Fig. 3.8 (a), (b), (c) and (d).

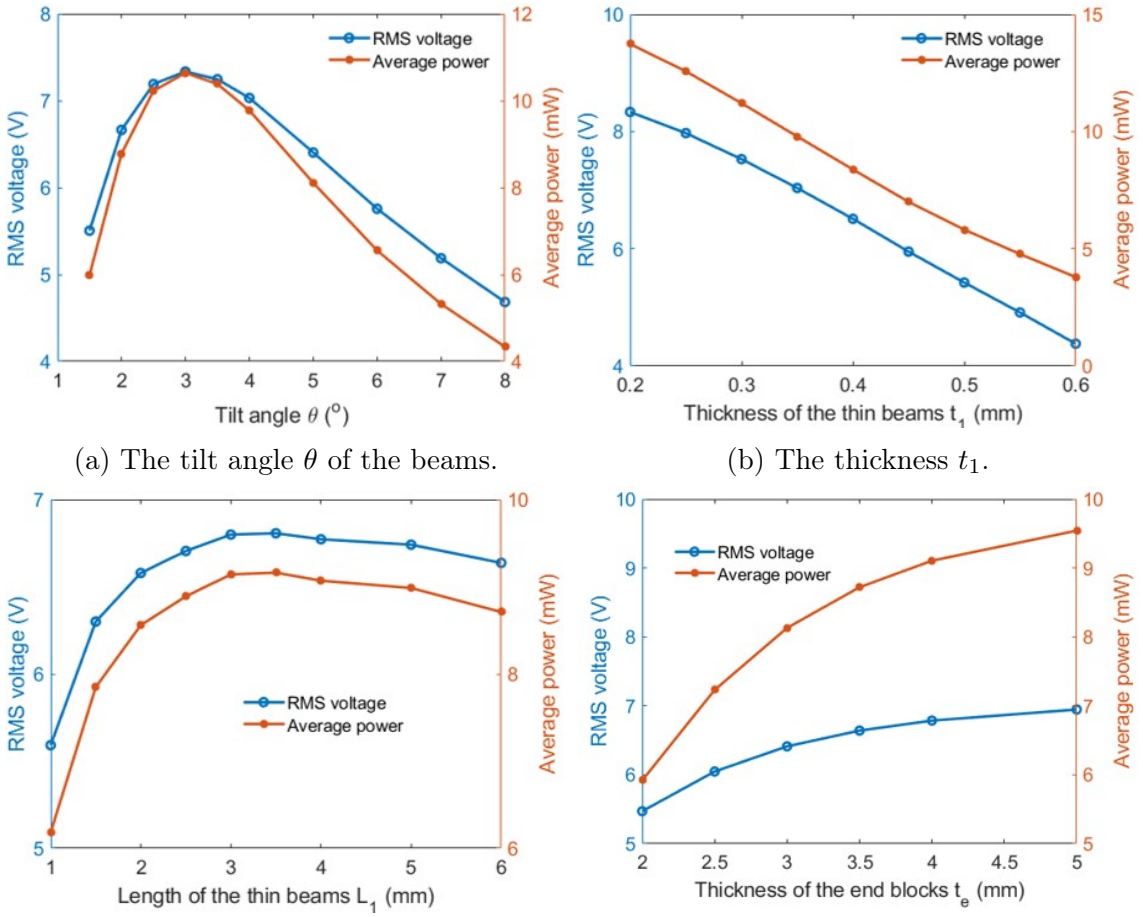

(a) The tilt angle θ of the beams.

(b) The thickness t_1.

(c) The length L_1 of the thin beam .

(d) The thickness t_e of the end block.

Figure 3.8: The RMS voltage and average power of the footwear energy harvester along with the geometric dimensions of the FAF.

Fig. 3.8 (a) shows that the RMS voltage and average power first increase and then decrease along with the tilt angle θ of the beam. There is an optimal tilt angle of around 3^o, which gives the maximum RMS voltage and average power. Nevertheless, the numerical simulations show that the maximum stress in the frame with the optimal tilt angle also rises

remarkably. The thickness of the thin beams has a severe impact on the RMS voltage and power output of the harvester, as shown in Fig. 3.8 (b). The average power reduces by 10 mW from 14 mW to 4 mW when only 0.4 mm increment in the beam thickness from 0.2 mm to 0.6 mm. This large reduction in power output is because more mechanical energy is stagnated in the frame as strain energy due to strong bending constraint as the thin beam becomes thicker. The RMS voltage and average power increase rapidly along with the increment in the length of the thin beams (hinges), as shown in Fig. 3.8 (c). However, they vary slowly with a slight reduction when the length of the thin beams is larger than 3.0 mm. The thickness of the end blocks has a smaller influence of the RMS voltage and average power, as shown in Fig. 3.8 (d), compared with the thickness of the thin beams. In particular, when $t_e > 3.5$ mm, the average power has a very slow increment along with t_e. Although thicker end blocks lead to higher power output, they are not desirable because thicker end blocks elongate the total length of the frame and consequently take more space and add weight.

3.6 Chapter summary

A material equivalent model is developed in this chapter to simplify the multilayer piezoelectric stack into bulk to facilitate FE modeling. A symmetric electromechanical coupling FE model is established to simulate the dynamic behavior of the piezoelectric energy harvester by exploiting the symmetries in geometry, load, and boundary conditions. The harvester is composed of six FAFs with inner piezoelectric stacks and two heel-shaped aluminum plates. The symmetric finite element model is validated against experimental results. The instantaneous voltage responses and power output at different walking speeds over varying external resistive loads are measured from treadmill experiments and simulated from the FE model.

The numerical simulation results are in good accordance with the experimental measurements, which confirms the developed symmetric FE model has good accuracy. The maximal heel-ground reaction forces and frequencies of the reaction force at the heel over different walking speeds are presented based on experimental measurements to study the influence on the power output of the harvester. A parametric study is performed on the experimentally validated FE model to investigate the effect of the geometric dimensions of the FAF on the average power output.

The proposed piezoelectric footwear energy harvester experimentally achieves the peak voltage and power of 20.6 V and 83.2 mW at 2.5 mph (4.0 km/h), 26.8 V, and 84.8 mW at 3.0 mph (4.8 km/h) with the optimal resistance of 5100 Ω. The average power outputs are around 8.5 mW and 9.3 mW at the walking speeds of 2.5 mph (4.0 km/h) and 3.0 mph (4.8 km/h), resulting in the mechanical-to-electrical power conversion efficiencies of 4.5% and 4.7%. The numerically simulated average power output is 34.7 mW at 6.0 mph (9.7 km/h), with a conversion efficiency of 10.8%. Results also show that the average power increases along with the walking speed, while the optimal resistance reduces. The geometric dimensions of the FAF have significant effects on the performance of the piezoelectric footwear energy harvester. An optimal tilt angle of the beams is found that could give the maximum power output with the given electrical resistance. The average power decreases with the increment in the thickness of the thin beams and slowly increases with the thickness of the end blocks.

Chapter 4

Piezoelectric energy harvesting from human walking using a two-stage amplification mechanism

4.1 Introduction

Hundreds of piezoelectric films mechanically stacked in series and electrically connected in parallel could greatly enhance the power output and durability in large force environments. Therefore, piezoelectric stack transducers have been applied to scavenge energy from large load environments, such as backpack [109], vehicle suspension system [119], public road [98], and railway system [97]. The large load capacity and high energy conversion efficiency render piezoelectric stacks very suitable for harvesting energy from footsteps. Force amplification mechanisms have been utilized to further increase power output of PHEs [120]. Two bow-shape concave metal plates were combined together with a piezoelectric plate sandwiched in-between to amplify the force exerted on the piezoelectric material [121]. Force amplification

frames in both compressive mode [102] and tensile mode [122] were developed to amplify the input forces of piezoelectric stacks for large power output. A compound two-stage bridge-type amplification frame was developed and optimized to maximize the force amplification ratio and power output of the piezoelectric stack transducer [123]. A rhombus-type force amplifier was adopted in a bidirectional energy harvester with a single piezoelectric stack to increase the power output [124]. Two arch-shaped metal bridges were used to amplify vertical input force to the sandwiched PZT discs and constitute piezoelectric bridge transducers for energy harvesting from roadway [125]. A footwear PEH sandwiched in a cymbal-shaped amplifier generated an average power of 2.5 mW [50]. Based on the cymbal-shaped design, a piezoelectric flex transducer with piezoelectric element sandwiched between two flex-plates was developed [126] and optimized to achieve the maximum force amplification and maximum power output [127]. The PZT-5H piezoelectric ceramic with a steel force amplification frame was integrated into a human shoe, and 1.43mW power was numerically simulated under an applied mass of 90 kg [128]. A single-stage force amplifier enabled a footwear PEH to have an average power output of 9 mW at the walking speed of 5.6 km/h [45]. These interesting works have exploited either the acceleration excitations induced by leg swing or heel strike and force excitations at the heel.

When the force amplification structures are used to improve the performance of a footwear energy harvester inside the heel, the design becomes significantly challenging and even intractable. These tough problems arise from the large reaction force and finite space at the heel, which are usually considered as load conditions and geometric constraints in the design and optimization. The force amplification structures must be designed to have sufficient strength to withstand the large reaction force during human walking. However, the strength of the structure depends on the material properties and geometric dimensions, which are restricted by the available space. In addition, the force amplification structures are

usually pushed to work at the edge of the yield strength in the design by the goal of maximizing the force amplification effect for large power output. Therefore, it's quite challenging to design a proper force amplification structure that could safely function in a footwear energy harvester.

This chapter presents a two-stage force amplification PEH that can be embedded into a shoe heel for scavenging energy from human walking. The dynamic reaction forces at a heel are amplified twice and then transferred to the inner piezoelectric stacks using the proposed two-stage force amplification frames. The contributions of this chapter include: 1) a compact heel-shaped energy harvester is designed, fabricated, tested and modeled under a large force input and very limited geometric space; 2) large power output is achieved by the two-stage force amplification mechanism which redirects and amplifies twice the input dynamic force at a heel before applied to the inner piezoelectric stacks; 3) the performance of the two-stage PEH is evaluated experimentally and numerically under different load levels, frequencies, walking speeds and external electrical resistance. The numerical simulations from a simplified single-degree-of-freedom model agreed well with experimental results. The power conversion performance of the two-stage PEH is compared with these reported in the literature. Results show that the proposed PEH has larger power output owing to the two-stage force amplification mechanism.

4.2 Design and work principle

The proposed two-stage force amplification mechanism is substantially realized by the first- and second-stage frames, as shown in Fig. 4.1 (a)-(c). The resultant two-stage piezoelectric transducer unit is given in Fig. 4.1 (d). The PEH proposed in this study consists of two heel-shaped metal plates and four two-stage piezoelectric transducer units, each of which

includes two multilayered piezoelectric stacks. The two-stage piezoelectric transducer units are sandwiched between the two heel-shaped metal plates by using screws. The overall layout of the proposed two-stage PEH is illustrated in Fig. 4.1 (e). When implanted in a shoe heel, the top and bottom heel-shaped plates take and transfer the dynamic forces from human body weight and ground reaction to the sandwiched second-stage force amplification frames (FAFs). The top plate is subjected to the dynamic force under the heel induced by body weight, while the bottom one is exposed to the reaction force from the bottom of the heel. Therefore, the two plates squeeze the force amplification frames during the heel strike and release during heel-off as human walking and thus compress the inner piezoelectric stacks to generate power. The heel-shaped plates are stiff enough to prevent undesired deformation so that the kinetic energy from human motions could be efficiently transferred to the two-stage transducer units, rather than stagnated as strain energy in the plates. The finalized dimensions of the heel-shaped plates are 98 mm $\times$ 67.5 mm $\times$2.7 mm, which fits a 9-size Belleville boot (26 cm in length).

The second-stage FAFs substantially play dual roles, i.e., amplify the vertical force F_{in} transferred from the heel-shaped plates and synchronously redirect it to the horizontal direction. Assume the dynamic force on the heel-shaped plates is evenly reallocated to the four second-stage FAFs, the input force F_{in} is thus a quarter of the total dynamic force on the plates. As shown in Fig. 4.1 (a)The second-stage compliant mechanism composes of four uniform beams, two end blocks, and two middle blocks. The beams have a tilt angle of θ_1 that enables the second-stage FAFs to work in a compressive mode and amplify the input force by $\alpha_1 = \tan(\theta_1)$ times [102], i.e., $F_{o1} = \alpha_1 F_{in}$. The output force F_{o1} of the second-stage FAF is imposed to the two first-stage FAFs in series, as shown in Fig. 4.1 (b), which is further amplified by $\alpha_2 = \tan(\theta_2)$ times and redirected to the inner piezoelectric stacks. The output of the first-stage frame is $F_{o2} = \alpha_2 F_{o1} = \alpha_1 \alpha_2 F_{in}$, which is the actual input

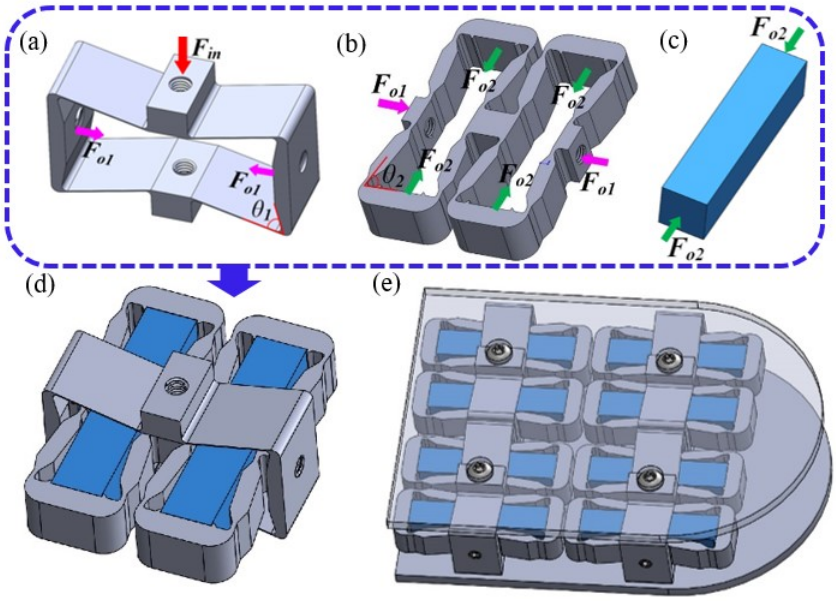

Figure 4.1: Illustration of the proposed two-stage PEH. (a) second-stage FAF; (b) first-stage FAF; (c) piezoelectric stack; (d) two-stage piezoelectric transducer unit; (e) assembled two-stage PEH.

force of the innermost piezoelectric stacks. This implies that the dynamic force at the heel is amplified twice with the overall force amplification factor $\alpha = \alpha_1\alpha_2$. Since the generated voltage of a linear piezoelectric stack transducer is proportional to the applied force [55], the proposed two-stage PEH, therefore, has a larger voltage output compared with the case of a single-stage design [45]. The first-stage FAF has a more complex design, including four identical thick beams with a tilt angle of θ_2 hinged with end blocks and middle blocks. The hinge connections reduce the bending constraints at corners so that mechanical energy can be efficiently delivered to the innermost piezoelectric stacks with a minimum loss as strain energy in the frames [45]. Supporters inside the two end blocks of the first-stage frame were designed to hold the inner piezoelectric stacks stably in dynamic environments. The first- and second-stage FAFs are connected at the middle blocks with set screws.

The design of the FAFs is crucial to the mechanical-to-electric energy conversion performance of the proposed two-stage amplification PEH because the generated instantaneous

electric power of the piezoelectric stack is proportionally correlated to the input force amplified by the FAFs. Therefore, a large overall force amplification factor α is desirable to maximize the power output. However, that is usually concomitant with large stress in the FAFs, which is unfavorable from the perspective of safety. This is because a large stress concentration could likely lead to the structural failure of the FAFs under dynamic loads. Furthermore, the geometric dimensions of the FAFs are limited by the finite space in the heel. An optimal two-stage FAF should own a large overall force amplification factor α, be compatible with the space in the heel, and meanwhile keep the maximum stresses in both the FAF and inner piezoelectric stacks within allowable material stresses. To attain the optimal two-stage FAF, a parameterized finite element (FE) model of the two-stage piezoelectric transducer unit was established in ANSYS using ANSYS Parametric Design Language (APDL) [107]. Both the FAFs and the PZT-stacks were modeled by the three-dimensional (3D) four-node tetrahedral solid structural element (Solid72). Piezoelectric materials can generate electric charges only when subjected to dynamic forces. Therefore, the piezoelectric effect was not considered in the FE analysis, where only static analysis was performed to design and optimize the FAFs. The overall force amplification factor of the two-stage FAF derived from the static analysis will later be used in the dynamic analysis. In terms of the previous study, the peak value of the measured dynamic forces at the heel at the walking speed of 3.0 mph(4.8 km/h) presented in the second chapter was used for the design. Since the proposed PEH contains four two-stage transducer units and the force is averagely allocated to them, one-fourth of the measured peak force was applied to the top surface of the middle block of the second-stage FAF by equivalent node forces, as shown inFig. 4.2 (a). It's assumed that the second-stage FAFs were well connected with the heel-shaped plates; thus, the force was uniformly distributed on the top surface of the middle block. Therefore, the equivalent node force applied to each FE node was equal to the input force divided by the total number of the FE nodes on the middle block's surface. Fixed boundary conditions

were applied to the nodes at the bottom surface of the other middle block. The spring steel (60Si2CrVa) with the yield strength of 1600 MPa, Young's modulus, and Poisson's ratio of 210 GPa and 0.32 were chosen for the frames due to its high strength [45].

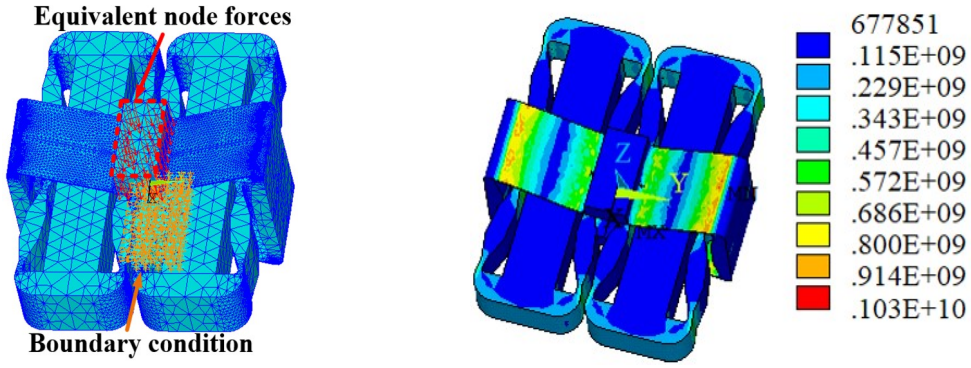

(a) FE model

(b) stress contour (Pa)

Figure 4.2: FE model and stress contour of the two-stage piezoelectric transducer unit

The output force F_{o2} of the two-stage FAF can be calculated by integrating the normal stress over the cross-section of the piezoelectric stacks in the FE analysis and thus the overall force amplification factor can be obtained by

$$\alpha = \frac{F_{o2}}{F_{in}} \tag{4.1}$$

A parameter study was performed on the FE model of the two-stage FAF to derive a large overall force amplification factor and meanwhile keep the maximum stresses within the allowable values of materials. The Von-Mises stress contour of the optimal two-stage FAF is given in Fig. 4.2 (b). It can be seen that the maximum stress in the FAF is around 1030 MPa, which is within the yield stress. The normal stress over the cross-section of the PZT-stacks is around 39 MPa. The calculated overall force amplification factor is α= 12.8. This implies that the input dynamic force during human walking could be amplified by 12.8 times before applied to the innermost piezoelectric stacks.

Table 4.1: Material and geometric properties

Piezoelectric stack: Navy Type II Ceram Tec SP505	FAF: Spring steel material (60Si2CrVa)
Cross section: A=7.0× 7.0 mm^2 ; Length: L=32.34;	Yield strength: 1600 MPa;
Young's modulus: E=41.67 Gpa;	Young's modulus: 210 Gpa;
Piezoelectric constant: $d_{33} = 475\ pC/N$;	Poisson's ratio: 0.32;
Permittivity: $\varepsilon_{33}^{T} = 1.66 \times 10^{-8}\ F/m$;	
Mass: m=12.5 ×10^{-3} kg;	

4.3 Experimental test

The piezoelectric stack used in this study is Navy Type II Ceram Tec SP505, which is constituted of 300 layers of PZT films [55]. The thickness of each PZT film is 0.1 mm. All the piezoelectric films in the stack are connected in parallel through 301 electrode layers of silver films. The thickness of each electrode layer is 0.1 μm. The geometric and material properties of the piezoelectric stack are given in Table 4.1 together with these of the force amplification frame.

All the two-stage piezoelectric transducer unit were tested on a vibration shaker (VG100-6) separately to examine all the piezoelectric stacks work well after piled in the frames. The experimental setup is shown in Fig. 4.3 (a), where the Spider 80X dynamic analyzer was used to control the system. The signal was generated by the Spider 80X, amplified by the amplifier, and then fed to the shaker. The two-stage piezoelectric transducer unit was connected to the shaker and a fixer frame using adapters, as shown in the close-up view in Fig. 4.3 (b). The force sensor between the shaker and adapters is used to measure the input dynamic force of the two-stage transducer unit. As an example, Fig. 4.4 presents the measured input force and open-circuit voltage of one unit, and the numerical simulation results from the SDOF model developed in chapter two in Eqs. 2.8 and 2.13 with the overall force amplification factor $\alpha = 12.8$. It shows that the numerically simulated voltage response of the single

transducer unit perfectly matches with the experimental result. This demonstrates that the integrated two-stage transducer works well and verifies that the FE analysis results and the SDOF model of the harvester are correct and have good accuracy.

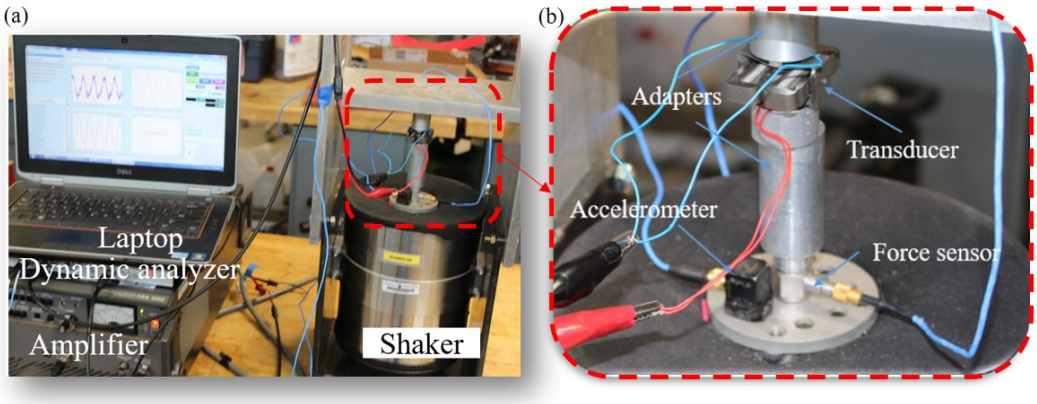

Figure 4.3: Experimental setup for the test of the two-stage piezoelectric transducer unit. (a) overall setup; (b) close-up view.

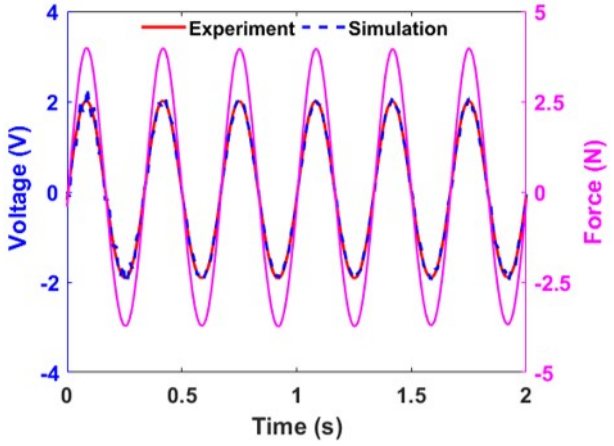

Figure 4.4: The open circuit voltage output of the two-stage transducer unit and the measured input force.

The prototype was tested on an Instron machine under different load levels and excitation frequencies. Fig. 4.5 illustrates the diagram of the experimental setup. The prototype of the two-stage PEH was clamped between the actuator and the fixed Instron crosshead using

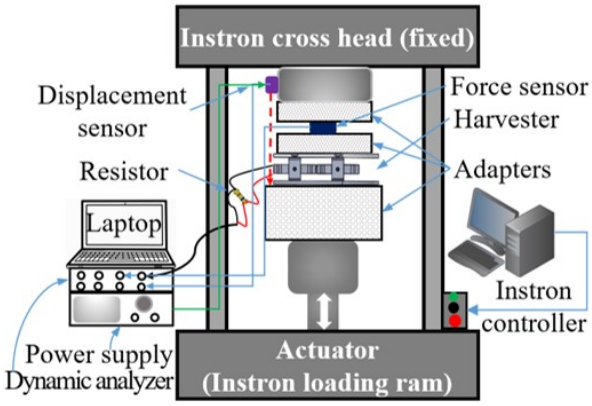

Figure 4.5: The diagram of the experimental setup.

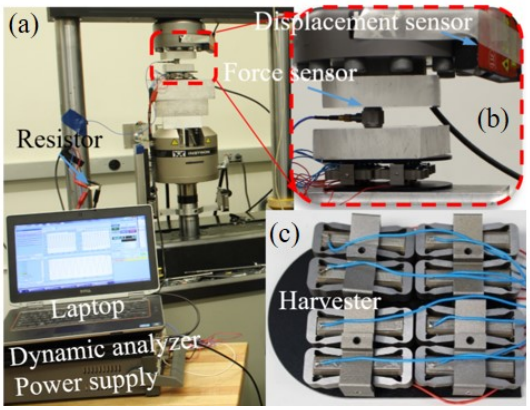

Figure 4.6: Picture of the experimental setup.

adapters, among which a force sensor (PCB 208C03) measured the input force. The actuator of the Instron that was controlled by the Instron controller could move up and down under the input displacement signal and thus provides excitation to the prototype. The driving displacements of the Instron actuator were sinusoidal. A laser displacement sensor (Micro-Epsilon optoNCDT 1302) powered by the power supply measured the input displacement. The PEH was directly connected to an external electrical resistive load. The input force, displacement, and the output voltage across the electrical resistive load were recorded by a dynamic analyzer (Crystal Instruments, Spider-80X). The amplitude of the input force was controlled by tuning the driving displacement of the Instron machine, which has a 90^o phase shift to keep the prototype in a compressive status during the actuator moved up and down. This caused that the prototype substantially subjected to a preload due to the phase shift of the driving displacement. In reality, the harvester in the heel also experiences a preload of human body weight. Fig. 4.6 (a) shows the overall experimental setup. A close-up view of the clamped harvester is given in Fig. 4.6 (b). The picture of the assembled prototype is shown in Fig. 4.6 (c), in which the top plate isn't included for a clear view of the two-stage units.

4.4 Results

The prototype of the two-stage PEH was tested under five load levels with the force amplitudes of 80 N, 150 N, 300 N, 400N, and 500 N in the experiments. Three frequencies, namely, 1 Hz, 2 Hz, and 3 Hz, were considered for the first four load levels to simulate different walking speeds. To prevent the prototype from breaking, only the first two frequencies were tested for the high load level of 500 N. The typical voltage and power outputs of the harvester are plotted Fig. 4.7 together with the measured input forces and displacements. Fig. 4.7 (a) and (b) are the results for the load level of 80 N and frequency of 1 Hz at the resistive loads of 300 Ω and 15000 Ω, respectively. The two resistive loads are selected to represent the cases of small and large resistance. Figs. 4.6 (c) and (d) plot the results for the load level of 500 N and frequency of 1 Hz. The numerical simulations were conducted to the SDOF model with the measured input forces, and the results are also presented in Fig. 4.7 along with the experimental results. Good agreements could be observed between the simulation results and the experimental results. This indicates that the simplified SDOF model has good accuracy in predicting the voltage outputs of the proposed two-stage piezoelectric energy harvester under different external electrical resistive loads.

The peak power outputs of the harvester with the two selected resistors are 0.45 mW and 2.75 mW for the load level of 80 N, 5.45 mW and 19.54 mW for the load level of 500 N. The actual overall force amplification factor was found less than the initial value of 12.8, which were around 9.2 for the load level of 80 N and only 4.5 for 500 N. Furthermore, the measured input forces are not ideal harmonic signals different from the input sinusoidal control signal of the Instron. These are because the tilt angles of the beams in the flexure FAFs change at large deformations, and thus the overall force amplification factor varies, or the stiffness of the PEH is not linear when large deformations happen. A high load level could result in the large tensile deformations of the thin beams in the second-stage frames. The large

deformations of these beams augment the tilt angle θ_1 and consequently reduce the overall force amplification factor. Nevertheless, the FE analysis for the force amplification factor was performed under the assumption of small linear elasticity and therefore didn't consider the large deformation and nonlinearity. Increasing the thickness of the beams could reduce the potential of large nonlinear deformation. Nevertheless, this could also reduce the overall force amplification factor due to the augment of stiffness.

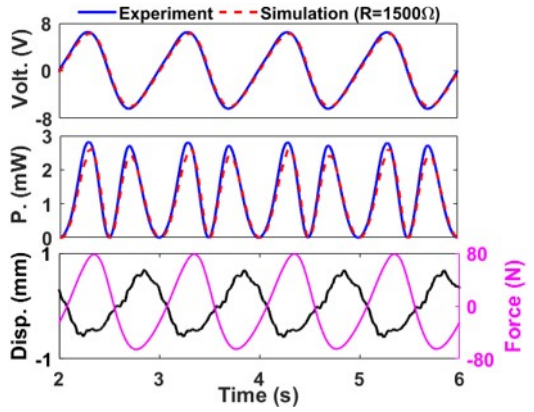

(a) 80 N and $R = 300\Omega$

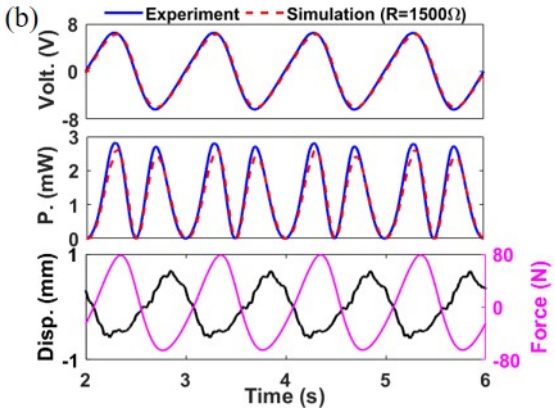

(b) 80 N and $R = 15000\Omega$

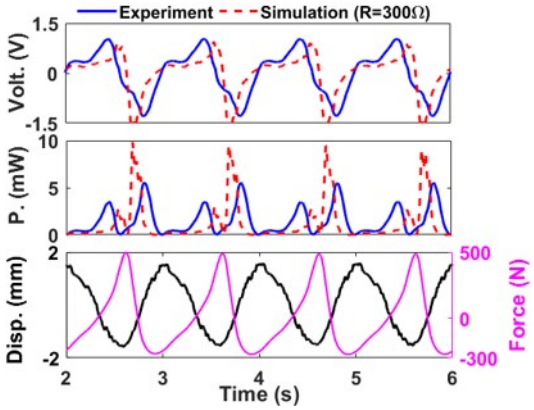

(c) 500 N and $R = 300\Omega$

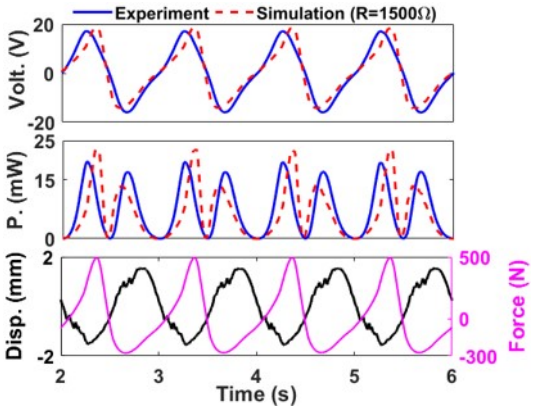

(d) 500 N and $R = 15000\Omega$

Figure 4.7: The instantaneous voltage and power of the prototype under excitation forces with the frequency of 1 Hz and the amplitudes of 80 N and 500 N.

The values of the overall force amplification factor under different load levels are identified by matching the numerical results with the experimental measurements and plotted

in Fig. 4.8. As analyzed above, the overall force amplification factor decreases as the load level increases. This is because the angle θ_1 of the second stage FAF becomes smaller as the deformations of the tilt beams increase along with the load level. The average power outputs over various resistors are calculated from the voltage responses to evaluate the performance of the two-stage PEH. As an example, Figs. 4.9 (a) and (b) present the average power at the load levels of 80 N and 300 N with different excitation frequencies. Again, the numerical simulations show good agreements with the experimental results. The average power increases along with the excitation frequency for varying resistive loads. An optimal resistance can be identified for each load case, which decreases as the excitation frequency increases.

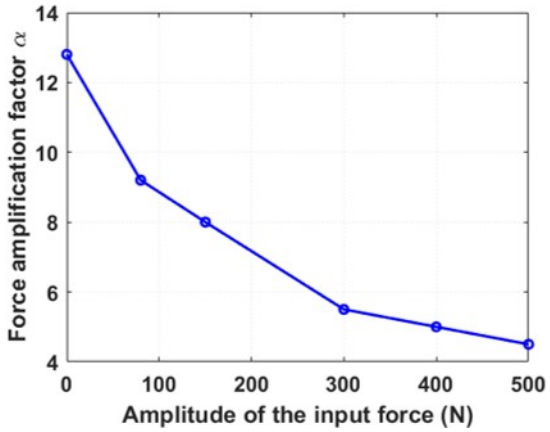

Figure 4.8: The actual value of the overall force amplification factor over different input force levels.

The maximum average power outputs of 1.65 mW, 3.77 mW, and 5.92 mW are obtained under the load level of 80 N at 1 Hz, 2 Hz and 3 Hz at the corresponding optimal resistive loads. The average power outputs of 6.35 mW, 14.02 mW, and 21.91 mW are achieved under the load level of 300 N at the three frequencies. The maximum average power outputs are plotted in Fig. 4.9 (c) for different load levels and excitation frequencies. The experimentally achieved average power outputs under the load level of 500 N at 1 Hz and 2 Hz are 10.96

mW and 23.86 mW, and the corresponding optimal resistive loads are 5100 Ω and 2400 Ω, respectively. The peak power outputs are 31.72 mW and 65.79 mW. The numerical simulation showed a maximum average power of 34.32 mW, and peak power of 110.2 mW can be attained at 3 Hz and the optimal resistive loads of 1600 Ω. The power is sufficient to continuously power a wearable wireless communication sensor (Zigbee), which has a maximum power consumption of 30 mW at the operational mode[110].

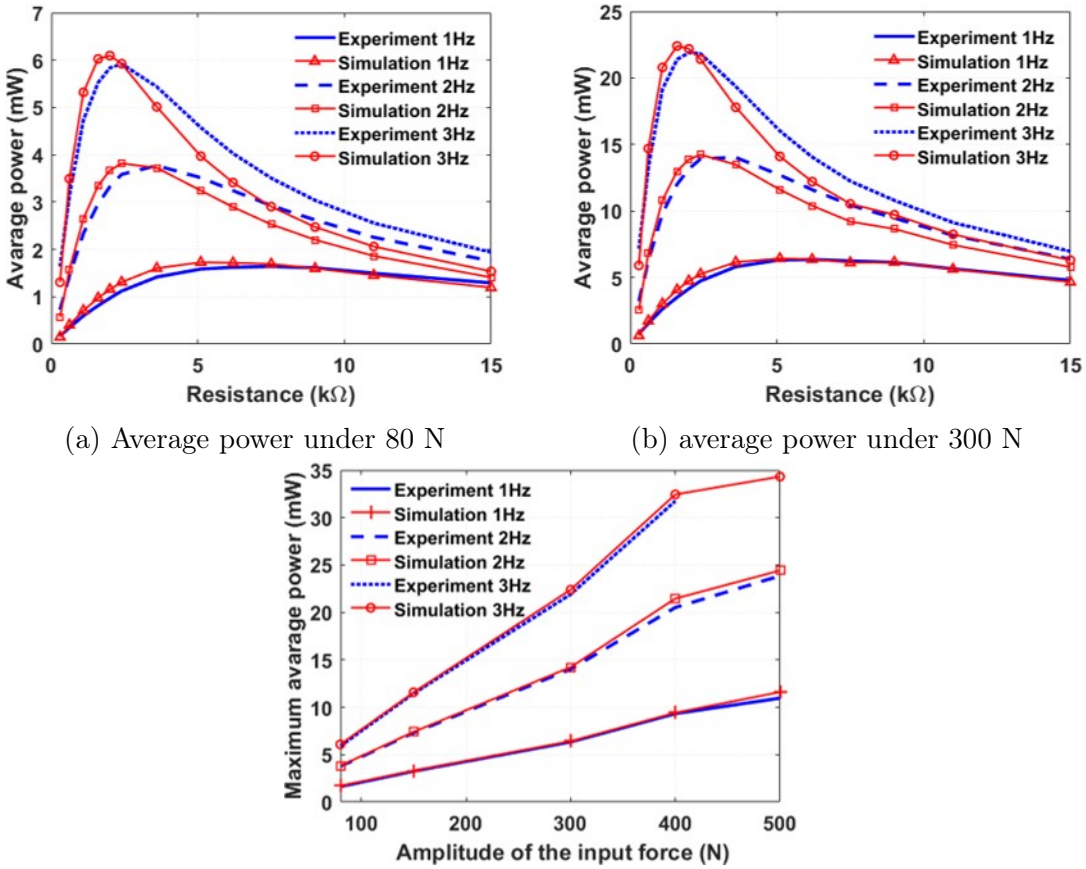

(a) Average power under 80 N

(b) average power under 300 N

(c) maximum average power under different load levels and excitation frequencies

Figure 4.9: Average power under different load levels and excitation frequencies.

Table 4.2 compares the performance of the proposed two-stage PEH with the results experimentally achieved by footfall piezoelectric energy harvesters in literature. The results show that the proposed two-stage PEH has the maximum average power output but a larger

size. The larger size is advisable for the force-based two-stage PEH. This is because the harvester is designed in terms of the heel size so that the dynamic forces over the entire heel area could be effectively collected by the heel-shaped plates and transferred to the piezoelectric transducers. It should be mentioned that this study is for the feasibility study and technique try; therefore, the investment cost was not fully considered.

Table 4.2: Comparison with the existing results.

Reference	Material	Average power (mW)	Size (mm^2or mm^3)
Qian et al. [45]	PZT (3-3)	9.3@4.8 km/h (0.9Hz)	68×94×24
Kymissis et al.[46]	PVDF (3-1)	1.1@1 Hz	100×(5∼8)×2.45
Kymissis et al.[46]	PZT (3-1)	1.8@1 Hz	7×7(insole)
Shenck and Paradiso[47]	PZT (3-1)	8.4@ 0.9Hz	50×85(insole)
Fan et al.[49]	PZT (3-1)	0.35@8 km/h	70×40×0.6
Zhao and You[8]	PVDF (3-1)	1.0@ 1Hz	80×50 (insole)
Kuang et al[50]	PZT (3-1)	2.5@4.8 km/h	52×30×12.7
Proposed two-stage PEH	PZT (3-3)	23.9@2 Hz/11.0@1Hz	67.5×(64 98)×25

To evaluate the power generation performance of the two-stage PEH under real human walking loads, simulations are performed using the validated SDOF model with the measured dynamic forces at a heel presented in the second chapter. The dynamic forces were measured from a male subject with the bodyweight of 84 kg and height of 172 cm at three walking speeds of 2.5 mph (mile per hour, 4.0 km/h), 3.0 mph (4.8 km/h), and 3.5 mph (5.6 km/h). The values of the overall force amplification factor under different walking speeds in the simulations are selected from Fig. 4.8 in terms of the peak values of the dynamic forces. Various external resistive loads are considered for each walking speed to identify the optimal resistance. The optimal resistances are found to decrease along with the increasing walking speed, which are 4100 Ω, 3600 Ω, and 3000 Ω at the walking speeds of 2.5 mph (mile per hour, 4.0 km/h), 3.0 mph (4.8 km/h), and 3.5 mph (5.6 km/h), respectively. The instantaneous voltage and power of the two-stage PEH across the optimal electrical resistive loads are

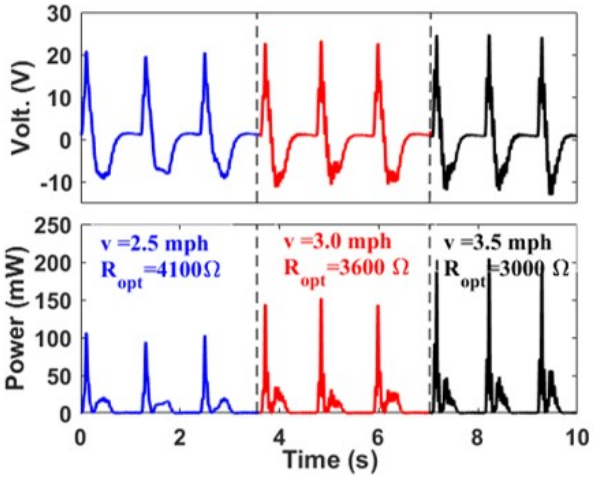

Figure 4.10: Instantaneous voltage and power outputs at different walking speeds.

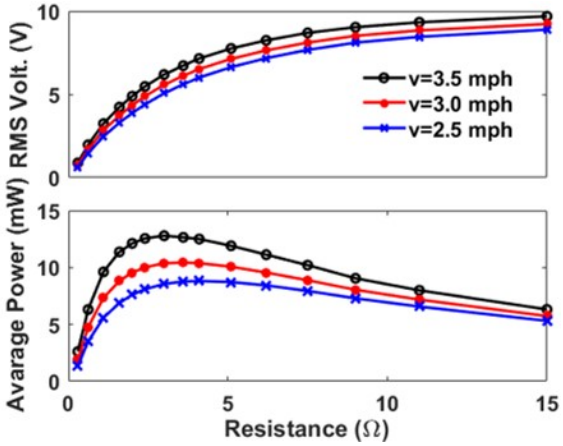

Figure 4.11: RMS voltage and average power outputs under various external resistive loads.

plotted in Fig. 4.10 for the three walking speeds. It shows that the instantaneous voltage and power increase as the walking speed increases. The peak power outputs of the harvester at the optimal resistances are 106.3 mW, 152.0 mW, and 204.7 mW at the three walking speeds, respectively. The root mean square (RMS) of the voltage and the average power outputs at different electrical resistive loads are calculated from the instantaneous voltage responses for each walking speed and presented in Fig. 4.11. It is observed that both the RMS voltage and the average have slight increments along with the augment of the walking speed. The average power outputs across the optimal electrical resistive loads are 8.8 mW, 10.4 mW, and 12.8 mW under the three walking speeds.

The voltage and power outputs of the harvester were only evaluated at different walking speeds, while the influence of human loads, including the bodyweight and wearable accessories, which would also be an interesting dimension, were not considered. However, human loads are varying largely in reality, depending on different wearers and accessories, like backpacks. The existing research has shown that increasing human load could result in an increase in walking speed [129]. Therefore, the detailed analysis of the influence of the

human load on the power output is not conducted in this study for the avoidance of duplication. Nevertheless, it can be reasonably predicted that the voltage and power outputs of the harvester will be aggrandized as human load increases because of the resultant higher walking speed and larger dynamic force at the heel.

4.5 Chapter summary

In summary, a two-stage force amplification piezoelectric energy harvester was developed, fabricated, modeled, and tested in this chapter. The harvester can be embedded into a shoe heel for scavenging energy from human walking to achieve autonomous power supply for wearable sensors and low-power electronics. Two-stage force amplification frames using a compliant mechanism were designed and analyzed to magnify dynamic forces at the heel and efficiently transfer the kinetic energy from human walking to the inner piezoelectric stacks with a minimum energy loss. In-lab experiments and numerical simulations were conducted to evaluate the performance of the proposed two-stage piezoelectric energy harvester over different load levels, frequencies, and human walking speeds. The numerical simulations matched well with the experimental results. Simulations showed that the maximum average power could be up to 34.32 mW under the dynamic force of 500 N at 3 Hz. 23.86 mW and 10.96 mW average power outputs were experimentally achieved at 2 Hz and 1 Hz, respectively. A comparison study showed that the proposed two-stage PEH outperformed the existing piezoelectric shoe harvesters in power generation but had a larger size. Numerical simulations were performed on the experimentally validated model with the measured dynamic forces at a heel under different walking speeds. The average power outputs of the two-stage PEH were 8.8 mW, 10.4 mW, and 12.8 mW under the walking speeds of 2.5 mph (mile per hour, 4.0 km/h), 3.0 mph (4.8 km/h), and 3.5 mph (5.6 km/h), respectively. The peak power outputs

under the three walking speeds can be up to 106.3 mW, 152.0 mW, and 204.7 mW.

Chapter 5

Bio-inspired bi-stable piezoelectric harvester for broadband vibration energy harvesting

5.1 Introduction

Bionic designs have been widely explored recently for the development of piezoelectric energy harvesters. By learning from the auditory hair bundle, a compliant bi-stable mechanism consisting of a four-bar linkage system was developed to enhance the performance of piezoelectric vibration energy harvesting [130]. Inspired by the structures of tree leaves, leaf-like piezoelectric harvesters composed of triangle polyvinylidene fluoride (PVDF) films and stiffeners mimicking bionic leaf veins were prototyped and tested for wind energy harvesting [131, 132]. Enlightened by the parasitic relationship between a dodder and the host plant, a host-parasite piezoelectric energy harvester was proposed to achieve the bi-stability and frequency up-conversion for low-frequency, low-amplitude vibration energy harvesting [133].

A piezoelectric composite energy harvester was designed by imitating the unique microstructure of sea sponges, which has demonstrated remarkable improvements in vibration energy harvesting due to the well-distributed stress on the piezoelectric component [134].

This effort proposes a novel low-cost, magnet-free, bi-stable piezoelectric energy harvester inspired by the rapid shape transition of the Venus flytrap leaves. A cantilever beam is cut into two sub-beams, whose free ends are constrained by an in-plane pre-displacement to create the bending and twisting curves and to harvest the mechanical potential energy during the snap-through. The force-displacement relationship, nonlinear dynamics, and energy harvesting performance of the proposed bio-inspired bi-stable piezoelectric energy harvester are analyzed and experimentally investigated under different excitation frequencies and levels.

5.2 Bio-inspired design

A good example of the bi-stable nonlinearity in nature is the Venus flytrap, which could trap agile insects by quickly closing its two curvature leaves within a very short time (100 ms) [135]. The Venus flytrap leaves are bi-curved in two directions and have two layers of lopes with local tissues, porous structures, and fluid in between. The leaves will close when the inner layer contracts and outer layer stretches and will open in reverse, as shown in Fig. 5.1(a) and (b), respectively. The curved leaves are almost flat in the first stable (open) state and concave at the second stable (close) state [136]. The plant achieves the open state by stretching its leaves back, during which the leaves store potential mechanical energy in the form of elastic energy. The stored energy will be released in the form of hydraulic movement in the porous structures when the leaves are triggered to snap shut. The rapid shape transition from the open state to the closed state as the leaves sense external stimulus is referred to as the snap-through phenomenon. The sudden snap-through of a nonlinear

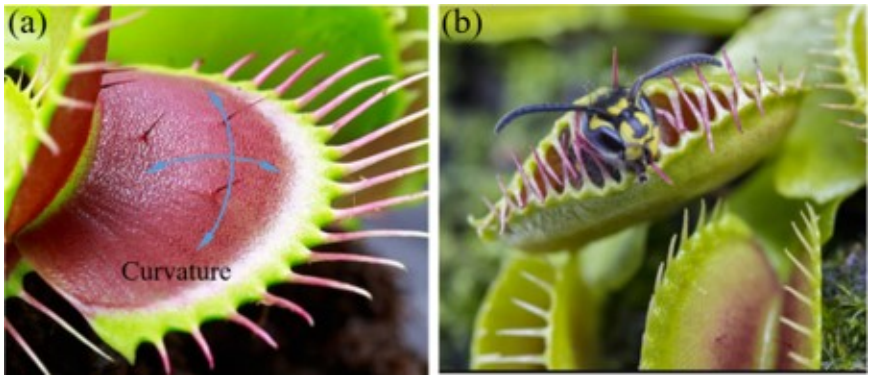

Figure 5.1: Bistability of the Venus flytrap leaves which have bi-directional curves with stored mechanical potential energy: (a) first stable state when the two leaves open (b) second stable state when the two leaves close.

bi-stable structure is usually associated with a large energy release, which results in a large power output desired for vibration energy harvesting. If this snap-through mechanism could be used for energy harvesting, large power output can be achieved due to the concomitant higher energy release. In summary, the knowledge learned from the Venus flytrap's snap-through mechanism includes: 1) the leaves are bi-curved in two directions, and 2) the leaves store potential mechanical energy.

Inspired by the rapid shape transition of the hyperbolic leaves of the Venus flytrap, a low-cost, magnet-free, bi-stable piezoelectric energy harvester is developed to harvest energy from broadband vibrations. The host structure of the proposed bio-inspired bi-stable piezoelectric energy harvester (BBPEH) is tailored from a cantilever beam, as illustrated in Fig. 5.2 (a), by cutting off a strip in the middle of the beam along the length direction. The resultant structure has two sub-beams, as shown in Fig. 5.2 (b), which is specifically inspired by the double-leaf structure of the Venus flytrap. The energy is harvested by bonding a piezoelectric transducer on the surface of one of the sub-beams near the clamped end, as displayed in Fig. 5.2 (c). It is worth noting that more piezoelectric transducers could be attached to the other sub-beam or the opposite surface of the same sub-beam to improve the power output.

To introduce the curvature in the length and width directions, an in-plane pre-displacement Δ along the width direction of the sub-beams is applied oppositely to the two free ends of the sub-beams, which are then constrained by two rigid blocks, as depicted in Fig. 5.2(d). The in-plane pre-displacement is exerted along the width direction of the sub-beams towards to the cut-off middle strip as indicated by the two vectors inFig. 5.2(d). It is worth mentioning that the pre-displacement should be less than the net distance between the two sub-beams to avert overlap.

These rigid blocks can also be used to tune the local resonant frequency of the nonlinear harvester. The in-plane pre-deformation constraint induces both bending and twisting deformations in the sub-beams, therefore, curvatures in both the length and width directions. The deformed structure also stores the potential energy of bending and twisting deformations resulting from the applied pre-displacement constraint, which is analogous to the potential mechanical energy in the Venus flytrap. Since the bending and twisting deformations are achievable bi-directionally for the sub-beams, the structure has two stable states as illustrated in Fig. 5.2 (e) and (f), respectively.

The proposed BBPEH satisfies the two conditions learned from the snap-through mechanism of the Venus flytrap. When the harvester is subjected to base excitations at the clamped end, it will vibrate either locally around one of the stable states (shown in Fig. 5.2 (e) and (f)) or globally snap from one stable state to the other. The design takes full advantage of the mutual constraint and balance of the two sub-beam structures to achieve the self-twisting and pre-stress purpose. Compared with the bi-stable piezoelectric energy harvesters made of magnets or composite laminates, the merits of the proposed BBPEH lie in its low cost, easy manufacturing, and the elimination of the magnetic field, as usually used in previously reported bi-stable energy harvesters. Since the proposed BBPEH doesn't need additional magnets and is simply made of metal sheet, the cost can be lower than the

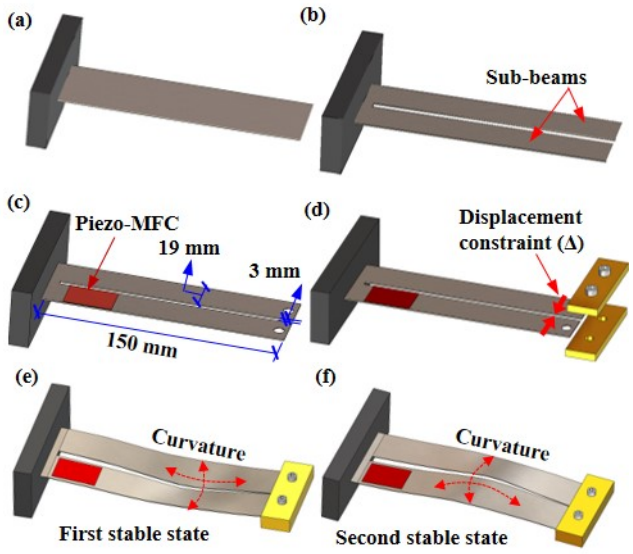

Figure 5.2: Design of the proposed bio-inspired bi-stable piezoelectric energy harvester: (a) cantilever beam (b) tailored cantilever beam with two subbeams (c) the piezoelectric transducer was attached to one of the sub-beams to harvest vibration energy (d) applied in-plane displacement constraint (e) bi-curved sub-beams under the applied constraint (first stable state) (f) second stable state.

magnet- and composite laminate-based harvesters with the same piezoelectric MFC transducer. Additionally, the quick snap-through motion between the two stable states can cause local high-frequency vibrations of the sub-beams due to the sudden energy release. As such, even under a low-frequency excitation, the sub-beams can locally vibrate at very high frequencies because of the snap-through. This capability to convert low-frequency excitations to high-frequency vibrations has not been extensively explored but can be very effective to attain large power outputs, especially when using piezoelectric transduction.

5.3 Modeling and experimental tests

A prototype of the bi-stable piezoelectric harvester was built using a metal cantilever structure, piezoelectric macro fiber composite (MFC, M2814-P2, Smart Material Corp.), and two

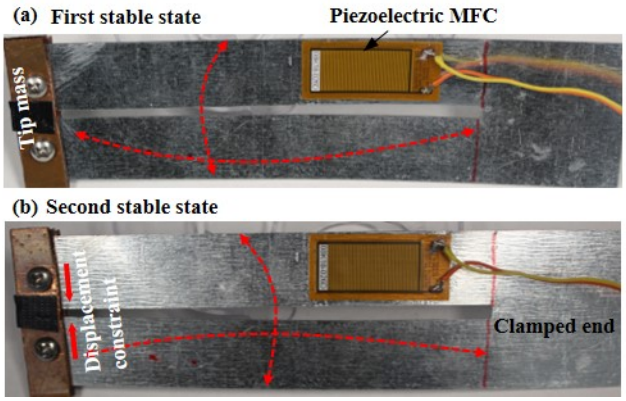

Figure 5.3: The prototype of the proposed bio-inspired bi-stable piezoelectric energy harvester: (a) first stable state, (b) second stable state.

rigid copper blocks. Fig. 5.3 (a) and (b) show the first and second stable states of the manufactured prototype of the BBPEH. The active length and width of the piezoelectric MFC are 28 mm and 14 mm, respectively. The thickness of the beam is 0.381 mm. The rest of the dimensions of the harvester are noted in Fig. 5.2 (c).

5.3.1 Modeling

It is challenging to develop a rigorous analytical model to characterize the proposed BBPEH because of the irregular structure and complicated constraints. A simplified lumped-mass model can describe the dynamics of a bi-stable beam structure with the axial pre-stress with coupled higher-order terms induced by the axial motion [82, 137]. The coupled governing mechanical and electrical equations of the proposed BBPEH are written as

$$\ddot{x} + 2\xi\omega_n\dot{x} + \beta(x\dot{x}^2 + x^2\ddot{x}) + f_{nl}(x) + \theta v + \bar{\theta}x^2 v = -\mu\ddot{y} \tag{5.1}$$

$$C_p\dot{v} + \frac{v}{R} - \theta\dot{x} - \alpha x^2\dot{x} = 0 \tag{5.2}$$

where x and v are the tip displacement of the BBPEH and voltage output across the external resistive load R, the over dots indicate the derivatives with respect to time. ξ is the damping ratio, β and α are the coefficients of the coupled higher-order terms induced by the axial stresses, θ and $\bar{\theta}$ are the linear and nonlinear electromechanical coupling coefficients, μ is the inertia force factor due to the distributed mass of the harvester, $\ddot{y}$ is the base excitation acceleration, f_{nl} is the nonlinear restoring force. C_p is the capacitance of the piezoelectric MFC, which is 48 nF as specified in the datasheet. It should be pointed out that the model considers the nonlinearity resulting from the pre-stress and the middle plane stretch of the beam but doesn't take the twisting motion into account. Below, using experimental results, it is shown that the system could be represented by this simplified single-degree-of-freedom model with acceptable errors.

5.3.2 Measurement of the force-displacement relationship

An experiment was carried out to derive the nonlinear restoring force describing the relation between the displacement and force. The experimental setup is shown in Fig. 5.4, in which a stander and a ball-screw mechanism were used to drive the force gauge (Mark-10 M2-2) forward and backward. The clamped end of the BBPEH was fixed to a support, and the free end was connected to the force gauge with a U-shape adapter and two pins. The two pins clip but do not hold the free end of the harvester tightly to allow the harvester to move freely in the axial direction as it is driven forward and backward by the force gauge. The laser displacement sensor (Micro Epsilon optoNCDT 1302) is used to measure the tip displacement of the harvester, which is the travel distance of the ball-screw. The Spider 80X (by Crystal Instruments Corp.) and laptop are used to collect the data from the displacement sensor. The force-displacement relationship was measured by driving the force gauge in both forward and backward directions, as indicated by the solid and dashed arrow lines in Fig. 5.4 (a).

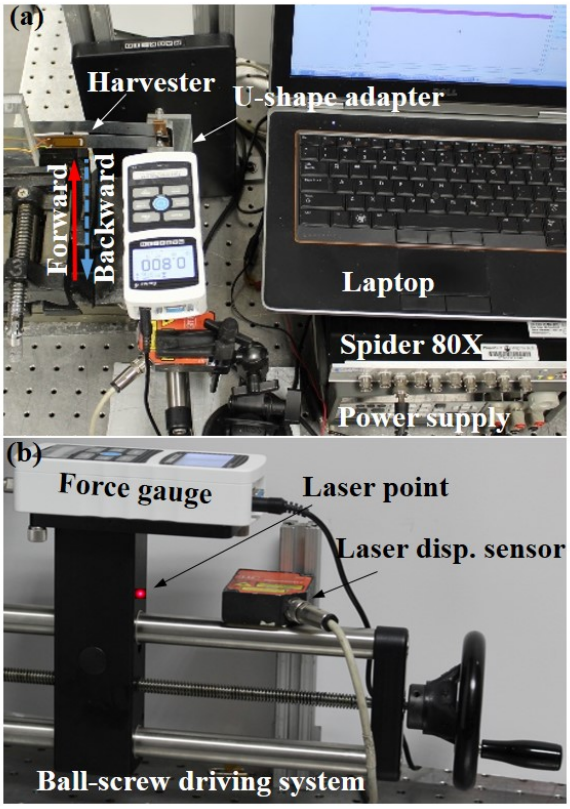

Figure 5.4: Experimental setup of the force-displacement measurement, (a) overall experimental setup, (b) close-up view of the ball-screw driving system and laser displacement sensor.

When the force gauge moved forward, the harvester snapped from the first stable state to the second one, as shown in Fig. 5.3. By reversing the force direction, the harvester snapped from the second stable state back to the first one. The measured force was read directly from the force gauge.

The measured force-displacement variations are plotted in Fig. 5.5 (a). The star and circle markers in the figure represent the measured data points as the force gauge moved forward and backward, respectively, while the curves are the fitted models with the sixth order polynomials. A_0 and C_0 mark the two equilibrium positions with the pentagrams corresponding to the two stable states, where the forces are zero. To measure the negative

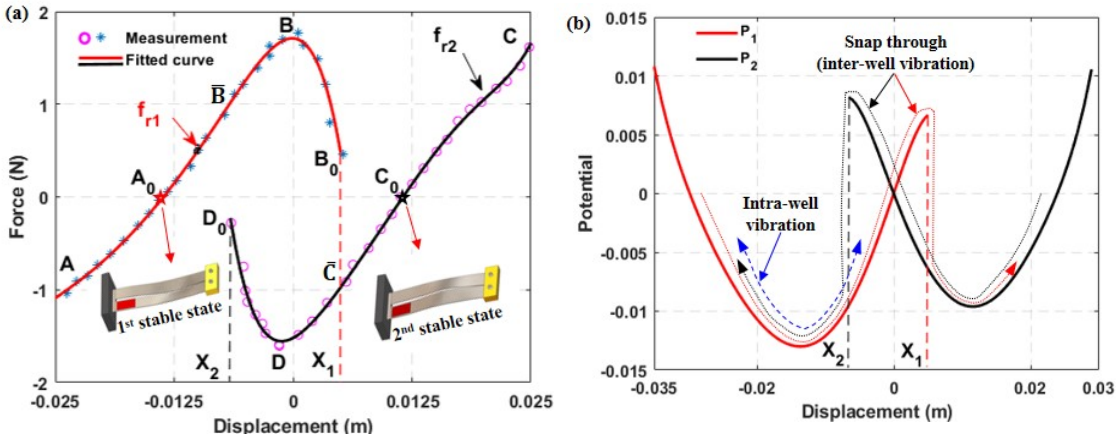

Figure 5.5: Measurement of the nonlinear restoring force: (a) measured force-displacement curve, (b) the potential function of the BBPEH.

force (A-A_0) in the experiment by driving the force gauge forward, the beam was pulled backward to a position in advance and was then gradually pushed forward by the force gauge. Similarly, to measure the positive force (C-C0) by driving the force gauge backward, the beam was first pushed to a position and was then slowly pulled backward. The force-displacement curves of the proposed BBPEH are quite different from that of a general bi-stable system, which usually characterized by one continuous force-displacement curve [86]. The nonlinear restoring force follows the A-A_0-B-B_0 (C-C_0-D-D_0) branch as the force gauge moves forward (backward). The force firstly increases along with the displacement to a maximum value at B (D), after which it decreases due to the negative stiffness. The nonlinear restoring force causes the jump to the other branch at the point B_0 (D_0) if the displacement keeps on increasing and exceeds X_1 (X_2), which indicates that the harvester snapped from the first (second) stable state to the second (first) one. The harvester exhibits a softening stiffness from point A_0 to A (C_0 to C), hardening softening stiffness from point A_0 to B (C_0 to D), and negative stiffness from point B to B_0 (D to D_0).

The polynominal curve fittings of the nonlinear restoring forces are given by

$$\bar{f}_{nl}(x) = \begin{cases} f_{r1} = \sum_{i=0}^{6} k_{1i} x^i, \text{A} - \text{A}_0 - \text{B} - \text{B}_0 \text{ branch} \\ f_{r2} = \sum_{i=0}^{6} k_{2i} x^i, \text{C} - \text{C}_0 - \text{D} - \text{D}_0 \text{ branch} \end{cases} \tag{5.3}$$

where the coefficients $\{k_{1i}, i = 0, 1, 2, ..., 6\} = [1.710, 6.016, -3.052\times10^4, -2.816\times10^6, -1.335\times 10^8, -3.363 \times 10^9, -3.510 \times 10^{10}]$, and $\{k_{2i}, i = 0, 1, 2, ..., 6\} = [-1.520, 54.48, 1.798 \times 10^4, 1.930\times10^6, 1.296\times10^8, -4.926\times10^9, 7.605\times10^{10}]$. It should be noted that the measured or fitted restoring force $\bar{f}_{nl} = mf_{nl}$, where m is the effective mass of the harvester that can be identified from the local natural frequencies and the linear stiffness near the equilibrium positions. In the numerical integration, the nonlinear restoring force $f_{nl}(x, t)$ at each time step is determined from the displacement at the current time step and the restoring force at the previous one. For instance, if the displacement $x(t_n)$ of the harvester at the current time step t_n is less than X_2 the restoring force is f_{r1} along the branch A-A_0-B-B_0; while if the displacement is larger than X_1, the restoring force is f_{r2} along the branch C-C_0-D-D_0. It is more complicated when $x(t_n)$ jumps between X_1 and X_2, in which case the nonlinear restoring force depends on the force from the previous time step. If $f_{nl}(x, t_{(n-1)}) = f_{r1}$, which implies $f_{nl}(x, t_{(n-1)})$ is on the branch A-A_0-B-B_0, $f_{nl}(x, t_n) = f_{r1}$ at the current time step, otherwise, $f_{nl}(x, t_n) = f_{r2}$. Based on the analysis above, a rule-base of the nonlinear restoring force is established and used in the numerical integrations of equations (5.1) and (5.2) as presented in Table 5.1.

Table 5.1: Rule-base for the nonlinear restoring force f_r

Displacement	$\boldsymbol{f_r(x, t_{n-1})}$	$\boldsymbol{f_r(x, t_n)}$ **and branch**
$x(t_n) < X_2$	f_{r1}	$f_{r1}, A \to \bar{B}$ or $\bar{\text{B}} \to$ A
$X_2 < x(t_n) < X_1$	f_{r1}	$f_{r1}, C \to \bar{B}$ or $\bar{\text{B}} \to$ C
$X_2 < x(t_n) < X_1$	f_{r2}	$f_{r2}, B \to \bar{C}$ or $\bar{\text{C}} \to$ B
$x(t_n) > X_1$	f_{r2}	$f_{r2}, D \to \bar{C}$ or $\bar{\text{C}} \to$ D

This variation of the force-displacement curves is attributed to the boundary conditions, imperfect geometry properties, and asymmetrical stress distribution in the harvester. Similar force-displacement curves were also found in other bi-stable systems, such as the bi-stable composite structure [117] and shallow arch [138]. It was observed during the experiments that the large deformation firstly appeared close to the clamped end of the harvester and then gradually spread toward the free end as the force increased. The potential energy function of the BBPEH was obtained by integrating the fitted polynomials of the nonlinear restoring forces and plotted in Fig. 5.5 (b), which suggests that the harvester has two asymmetric potential wells and independent barriers. The asymmetry in the potential wells results from the manufacturing error in the geometries of the two sub-beams and the effect of the piezoelectric MFC transducer. The trajectories of both the intra-well and inter-well motions of the BBPEH are illustrated in Fig. 5.5 (b). The intra-well and inter-well dynamics of a bi-stable system primarily depend on the potential function apart from the external excitation. It is worth noting that the potential function, as well as the force-displacement curves of the proposed BBPEH, is set by the pre-displacement Δ once the geometric dimensions are given. Intuitively, exerting a larger pre-displacement of Δ to the free ends of the sub-beams requires more effort than applying a smaller one due to the larger restoring force. In principle, a larger Δ injects more potential energy to the system in the form of larger stress and strain. This implies that the system created with a larger Δ has deeper potential wells and higher barriers, and large energy release accompanied by larger amplitude vibrations during the snapping through. However, bi-stable energy harvesting systems with deeper potential wells and higher barriers require larger external excitations to activate the desired snap-through dynamics compared with those with lower potential wells. It has also been shown that the asymmetry of potential wells has a significant influence on the energy harvesting performance of bi-stable harvesters under random excitations [139]. The asymmetry in the potential wells degrades the mean power output for the random excitations of low to moderate noise

intensities [140]. In the proposed BBPEH configuration, the asymmetry in the potential wells can be reduced or eliminated by subtly tailoring the sub-beams.

5.3.3 Dynamics experimental setup

Experiments were conducted on the prototype to validate the design, identify the system parameters, and evaluate the energy harvesting performance of the proposed BBPEH. The experimental setup is shown in Fig. 5.6, where the harvester was fixed on a VT-600 shaker, providing base excitations. A Polytech Laser Vibrometer (Model # PSV-500) was used to measure the tip velocity and record the harvester's voltage output. The input signal was generated from the laser vibrometer, amplified by an amplifier, and then fed to the shaker. The PCB accelerometer (PCB 356A17) was employed to measure the base excitation acceleration. Frequency sweep experiments were performed firstly with very low excitation levels (amplitudes) to identify the local resonant frequency ω_n under the open circuit and the electromechanical coupling coefficient θ of the harvester at the first stable state. The local vibration resonant frequency of the harvester was found to be ω_n=12.47 Hz. The remaining system parameters were identified from the frequency sweep experiment under a higher excitation level and given as follows: $\xi = 5.6 \times 10^{-3}, \beta = 1.0, \theta = 2.821 \times 10^{-5}, \bar{\theta} = 0.2, \mu = 0.33,$ and $\alpha = 6.08 \times 10^{-2}$.

5.4 Results and discussion

5.4.1 Frequency sweep excitations

The numerical integrations of the governing equations (5.1) and (5.2) were performed using the input acceleration excitations measured from experiments. The nonlinear restoring force

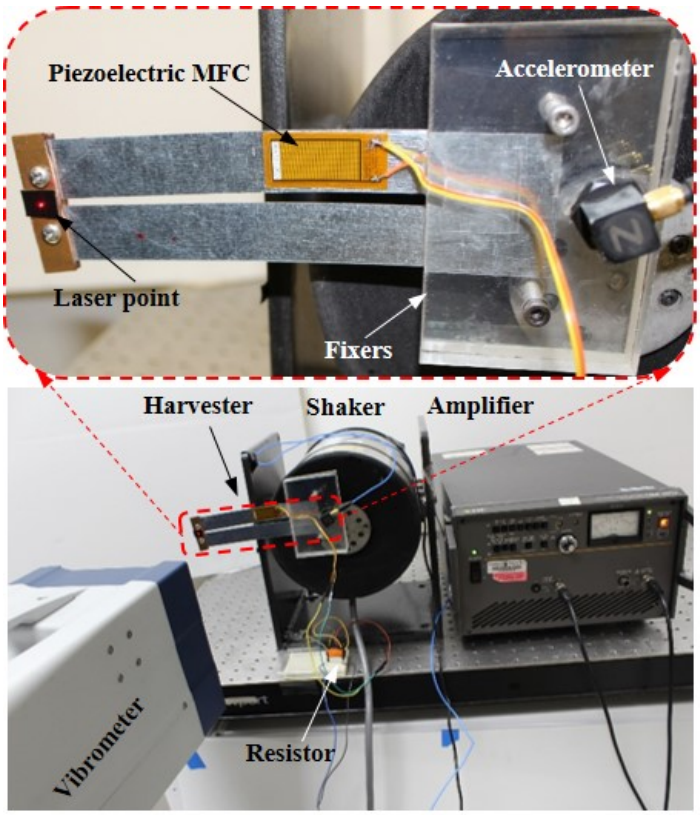

Figure 5.6: Experimental setup of dynamics tests.

at each time step of the numerical integration was determined using the proposed rule-base in Table 5.1. The excitation frequency linearly increases and decreases in the range of interest for the upward and downward frequency sweep experiments and numerical integrations. The measured excitation acceleration also linearly increases and decreases along with the upward and downward frequency sweeps. For the intra-well dynamics test, the excitation acceleration level is lower, between 0.35g to 0.55g, in comparison to 2.1g to 4.1g noted as the higher excitation level to activate the large amplitude inter-well vibrations. The experimental measurements and simulated results of the frequency sweep at a lower level are plotted in Fig. 5.7 (a) and (b), respectively, including the tip displacements, velocities, and voltages across an external resistive load of $R = 180$ kΩ. The left column of Fig. 5.7 plots the upward frequency sweep results, while the right column shows the downward frequency sweep results. The displacement responses in Fig. 5.7 clearly show that the system only oscillates around the first stable state for both the upward and downward frequency sweep, and the voltage responses are small, in particular for the case of the upward frequency sweep. The numerical integration results in Fig. 5.7 (b) agree well with the measurements for the small-amplitude intra-well oscillations in Fig. 5.7 (a). Fig. 5.8 (a) and (b) plot the experimentally measured and numerically simulated frequency sweep results at a higher excitation level. The snap-through vibrations could be observed from the displacement responses in Fig. 5.8 (a) and (b) for both the upward and downward frequency sweep. Relatively large voltage levels are harvested over the frequency interval of [10.6, 12.3] Hz from the vibrations associated with snap-through responses. However, discrepancies are observed for the global vibrations from Fig. 5.8 (a) and (b). Specifically, the integration results of the downward frequency sweep show a slightly wider frequency bandwidth (10.8-11.8 Hz) of the inter-well vibrations than the experimental results (10.6-11.2 Hz). These discrepancies are attributed to the model errors and noise in the measured acceleration excitation, especially the error in the measured and fitted force-displacement relation. For instance, the model doesn't consider

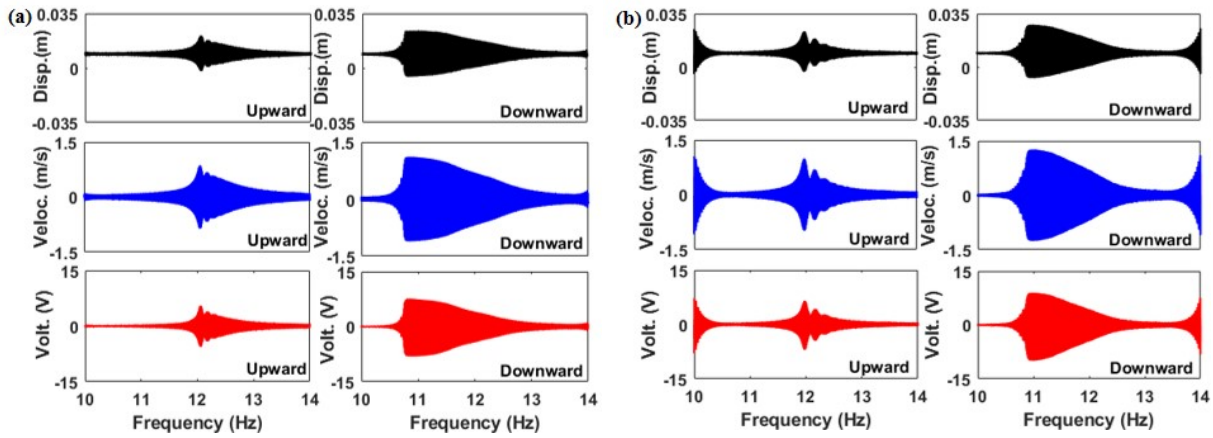

Figure 5.7: Frequency sweep experiment results of intra-well vibrations: (a) experiment, (b) simulation.

the twisting motion of the two sub-beams, which could result in evident errors at higher excitation accelerations

5.4.2 Harmonic excitations

To investigate the dynamics of the proposed BBPEH, experiments were also carried out under harmonic base acceleration excitations with a frequency of 12 Hz close to the local resonant frequency at different amplitudes. The plots in Fig. 5.9 (a)-(f) show the time domain velocity responses of the tip mass and the corresponding power spectrum obtained from FFT analysis for the excitation amplitudes of 0.1 g, 0.6 g, and 4.0 g, respectively. Fig. 5.9 (a) and (c) indicate that the tip mass experiences an almost perfect periodic motion at the lower excitation levels of 0.1 g and 0.6 g, and the corresponding power was concentrated at the excitation frequency of 12 Hz, as shown in Fig. 5.9 (b) and (d). The small-amplitude superharmonics at 24 Hz and 36 Hz appear due to the nonlinearity at the excitation level of 0.6 g, as shown in the inset in Fig. 5.9 (d). As the excitation amplitude is increased further to 4.0 g, the system experiences the snap-through phenomenon and exhibits very strong

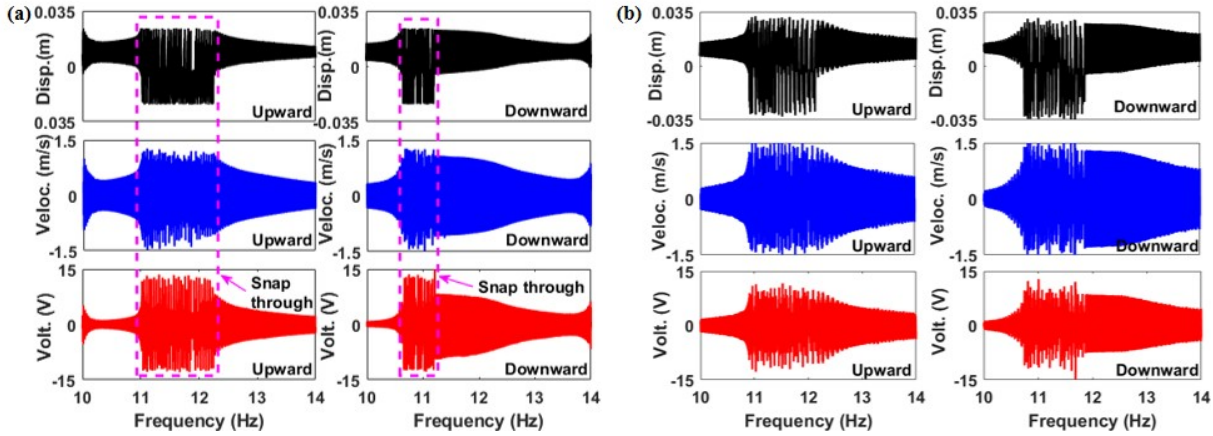

Figure 5.8: Frequency sweep experiment results of inter-well vibrations: (a) experiment, (b) simulation.

nonlinear vibrations, as illustrated in Fig. 5.9 (e), which exhibits relatively large peaks at subharmonics and superharmonics of the excitation frequency. These results also demonstrate that the nonlinear degree of the system increases along with the external excitation level. The power spectrum in Fig. 5.9 (f) shows more peaks over multiple frequencies in addition to the excitation frequency. Syta et al.[91] defined this type of response with clear and distinct peaks in the power spectrum as the multi-frequency regular snap-through response. The snap-through motion of the harvester could become chaotic at different excitation frequencies and levels. As an example, Fig. 5.10 presents the velocity response and the power spectrum of the harvester under the excitation level of 4.0 g at 10 Hz, where the energy is distributed over a broadband frequency range besides the large amplitude snap-through motion at the excitation frequency. These large-amplitude nonlinear jumps between the two potential wells with continuous spectrum over a wideband frequency range is referred to as the twin-well chaotic snap-through motion [141].

Time-domain voltage responses of the harvester at the excitation frequency of 12 Hz and different excitation levels of 0.1 g, 0.6 g, and 4.0 g are plotted in Fig. 5.11 (a)-(f), along

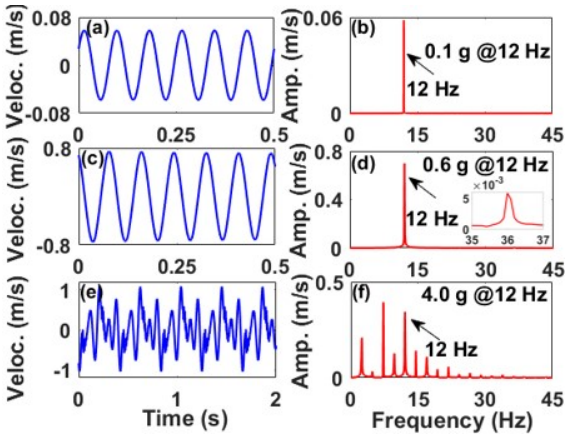

Figure 5.9: Time history and FFT of the tip velocity at the excitation frequency of 12 Hz and amplitudes of 0.1 g (a)-(b), 0.6 g (c)-(d), 4.0 g (e)-(f).

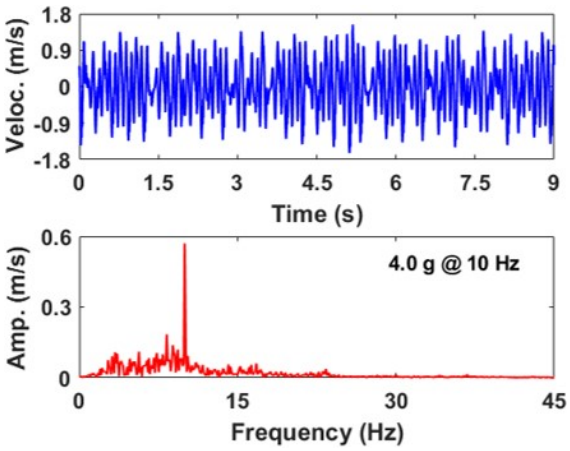

Figure 5.10: Time history and FFT of the tip velocity at the excitation frequency of 10 Hz and amplitudes of 4.0 g.

with the power spectrum obtained from FFT analysis. At the lower excitation level of 0.1 g, the time-domain voltage responses and power spectrum presented in Fig. 5.11 (a) and (b) exhibit a periodic motion at a frequency exactly equal to the excitation frequency. Moreover, the system oscillates only in one of the two potential wells under this small excitation level. This vibration is therefore referred to as the single-well period-one motion [141]. As the excitation level is increased to 0.6 g, the time-domain voltage responses in Fig. 5.11 (c) exhibit a period-doubling bifurcation, and two peaks in the power spectrum, at the excitation frequency of 12 Hz and its harmonics at 24 Hz. The second peak at 24 Hz confirms that the quadratic nonlinearity has a significant contribution to the system dynamics. This conclusion is consistent with the discussion on the experimental results of the force-displacement relationship. It should be noted that this periodic intra-well motion with two dominant frequencies is different from the period-two motion noted by Panyam et al. [141] and Emam et al.[142], where the additional peak of the power spectrum was at the subharmonic of the excitation frequency. The time-domain voltage response in Fig. 5.11 (e) shows the periodic snap-through motion with relatively high-frequency vibrations at each snap-through

phenomenon, which is not observed from the velocity response of the tip mass in Fig. 5.11 (e). This indicates that the sub-beams of the harvester undergo more complicated local dynamics during the snapping through. This high-frequency response is attributed to the local vibrations of the sub-beam, where the piezoelectric MFC transducer is attached. The high-frequency voltage response during one of the snap-through phenomena, as shown in the dotted box, is expanded in Fig. 5.11 (g). The power spectrum of the voltage response plotted in Fig. 5.11 (f) confirms that the sub-beams experience multiple high-frequency dominated dynamics. The continuously distributed spectrum over the wide frequency range suggests the chaotic motion of the sub-beams during the large amplitude inter-well vibrations. This suggests that the proposed BBPEH could extend the effective frequency range over a quite wide bandwidth aside from the single excitation frequency, and therefore generates more power. It should be mentioned that a much lower external resistor of 8.2 kΩ was used for the inter-well vibration because of the high-frequency local vibrations during snapping through, instead of the 180 kΩ used for the case of intra-well vibrations. Nevertheless, the voltage outputs are still much higher than those of the local intra-well vibrations plotted in Fig. 5.11 (a) and (c) even at a much lower resistive load due to the large amplitude inter-well vibrations.

5.4.3 Energy harvesting performance

The energy harvesting performance of the proposed BBPEH is also evaluated in terms of the average power output at different excitation levels and frequencies. The average power outputs across the external resistive load of $R = 180$ kΩ at lower excitation levels of 0.1 g, 0.2 g, and 0.3 g are presented in Fig. 5.12 (a) for different excitation frequencies. It is observed that the power outputs are very small (less than 5 μW) at the excitation frequencies away from the local resonant frequency under the low excitation levels. These levels increase dramati-

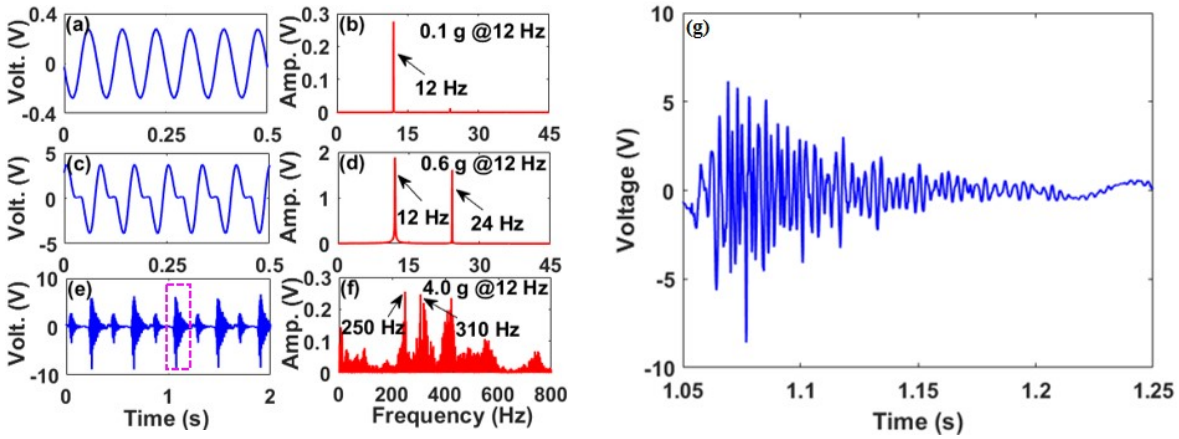

Figure 5.11: Time history and FFT of the voltage output at the excitation frequency of 12 Hz and amplitudes of 0.1 g (a)-(b), 0.6 g (c)-(d), 4.0 g (e)-(g).

cally as the excitation frequency moves closer to the local resonant frequency. The harvester experienced almost linear local intra-well vibrations at low excitation levels. Fig. 5.12 (b) plots the average power outputs across the same resistor at the moderate excitation levels of 0.4 g, 0.5 g, and 0.6 g. It should be noted that the harvester oscillates around one of the local stable states, and snap through does not take place under these moderate excitation levels over the frequency ranges of interest. The curves of the average power output over different frequencies clearly bend to the left hand, noting the evident soft nonlinearity associated with the local vibrations of a bistable system. As the excitation level increases, the frequency bandwidth of the power output is also broadened besides the increase in average power output.

At higher excitation levels, the large amplitude inter-well vibrations take place over a certain frequency range, and thus much higher average power outputs could be attained. Since it has been found that the voltage response of the harvester is dominated by the higher frequency components as a result of the snap-through dynamics, the lower load resistance of $R = 8.2$ kΩ was used in the experiments. The average power outputs of the harvester at

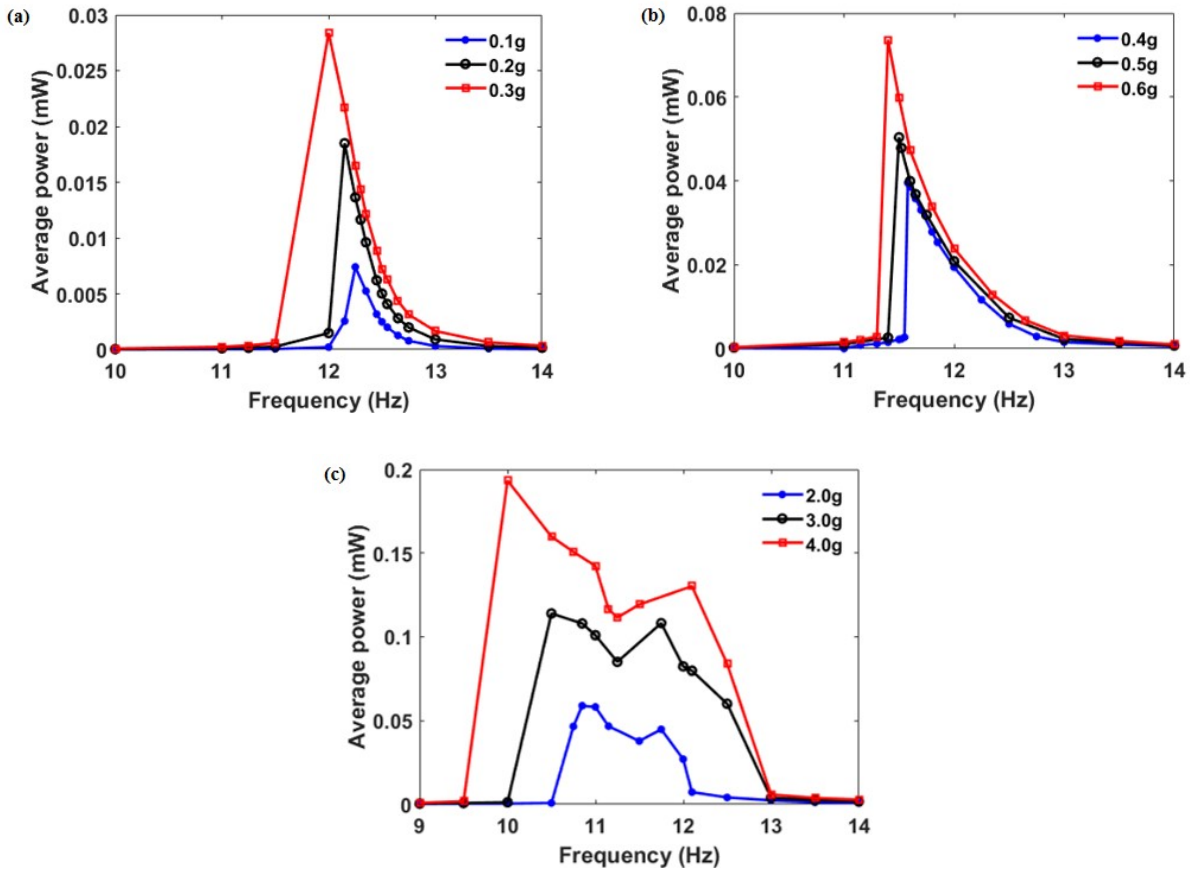

Figure 5.12: Average power outputs of the BBPEH at different excitation levels and frequencies: (a) lower excitation levels, (b)moderate excitation lever, (c) higher excitation levels.

the excitation levels of 2.0 g, 3.0 g, and 4.0 g and frequency varying from 9 Hz to 14 Hz are presented in Fig. 5.12 (c). At the excitation level of 2.0 g, the harvester has a significant large power output over the frequency range of 10.5-12.0 Hz because the large amplitude inter-well vibrations are activated. The harvested power is very small outside of this frequency range due to the small amplitude intra-well dynamics. The frequency bandwidth of the inter-well vibration becomes wider as the excitation level increases to 3.0 g and 4.0 g, to cover 10.0-13.0 Hz and 9.5-13.5 Hz, respectively. The average power output also evidently increases over these bandwidths. The maximum power output is around 0.193 mW at the excitation of 10 Hz and 4.0 g. This wideband feature of the frequency range in which the harvester could achieve snap-through dynamics accompanied by large power outputs is a key design purpose of nonlinear energy harvesters in practice since ambient environment excitations usually contain frequency components over a wide frequency broadband.

5.5 Chapter summary

Inspired by the rapid shape transition of the Venus flytrap leaves, a novel low-cost, magnet-free, bi-stable piezoelectric energy harvester is designed, prototyped, and tested towards assessing its capability for energy harvesting from broadband vibrations. Different from bi-stable energy harvesters that make use of nonlinear magnetic forces or residual stress in laminate composites, the proposed bio-inspired bi-stable piezoelectric energy harvester (BBPH) takes advantage of the mutual self-constraint at the free ends of two cantilever sub-beams with a pre-displacement. This mutual pre-displacement constraint at the free ends curves the two sub-beams in two directions inducing bending and twisting deformations with higher mechanical potential energy in the harvester. The force-displacement curves of the prototype were experimentally measured and numerically fitted by polynomial models. Both

frequency sweep and harmonic experiments are conducted on the prototype to study the nonlinear dynamics and to evaluate the energy harvesting performance. The results show that the sub-beams experience much richer local dynamics with multiple high-frequency vibrations compared with the tip mass, even under a single low-frequency harmonic excitation. These local high-frequency vibrations are desirable for high power output. The average power output of the BBPH shows an increasing trend in both the amplitude and frequency bandwidth as the excitation level increases and is high enough to activate large-amplitude inter-well vibrations. Although results were presented for one piezoelectric patch, additional patches that can harvest energy from other bending and torsion deflections can significantly increase the demonstrated power levels.

Chapter 6

Theoretical modeling and experimental validation of a torsional piezoelectric vibration energy harvesting system

6.1 Introduction

In oil exploration, a borehole is created by a drill bit, which is driven by an electrical motor at a constant rotational speed. The difference in material properties of the drilling system, the friction along the wall of the borehole, and the resistance on the drill bit cause the rotational speed of the drill tip to vary and fail to keep the same speed with the motor, inducing torsional vibration of the drill shaft. The torsional vibration energy can be harvested by a shear-mode piezoelectric harvester and converted into usable electricity to power sensors. This chapter presents a theoretical model and experimental validation of a piezoelectric transducer for torsional vibration energy harvesting from a rotation shaft. The effect of the position and orientation of the piezoelectric transducer on the power output is investigated. The

transducer position is parameterized by two variables, the axial position, and the orientation. Results suggest that the piezoelectric transducer works only in d_{15} mode (pure shear mode) when the attached angle is 0° and 90°, in the coupled mode of both d_{31} and d_{33} for the attached angle of 45°, in multiple coupled mode of d_{15}, d_{31} and d_{33} for other angles. The optimal position and angle of the transducer are obtained by parameter analysis. The electromechanical coupling behavior between the piezoelectric transducer connected to an external resistor and the torsional shaft is assumed to be linear and weak [143]. All the material properties used in the modeling are assumed to be constant with respect to the effect of a dynamic environment. The approximate expressions of voltage and power are derived and proven to predict the voltage and power accurately. The transducer in d_{15} mode (pure shear mode) has larger power output than the one in the coupled mode of d_{31} and d_{33}. The implicit relationship between the power output and the two position parameters of the transducer is intuitively revealed and physically interpreted based on the approximate power expression. Those findings offer a good reference for the practical design of the torsional vibration energy harvesting system.

6.2 Theoretical Modeling

Torsional vibration frequently appears in shaft, pipe, and rod structures in mechanical systems. To investigate the harvestable energy from torsional vibrations, it is necessary to establish a theoretical model and study the transducer's placement. Different models have been developed in literature to describe the torsional vibration of an oil drilling shaft [61, 144, 145]. A typical oil well drilling system usually consists of a surface-mounted drive system and a drill bit at the top and down ends of the shaft, respectively [61]. The surface-mounted drive system and the drill bit can be modeled as two flanges. Therefore, the torsional vibration

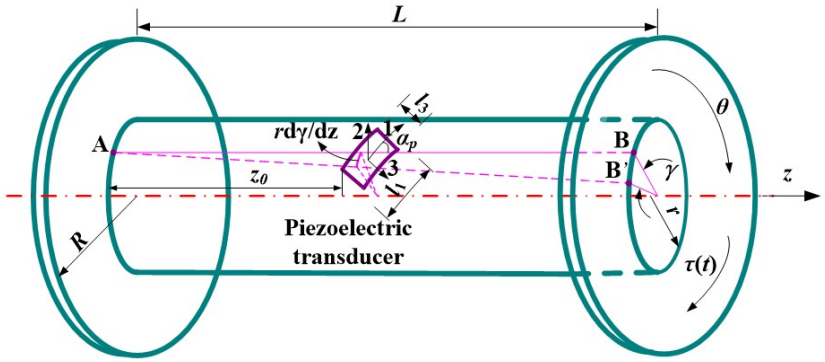

Figure 6.1: Model of the torsional vibration energy harvesting system.

energy harvesting system can be characterized by a shaft with two rotational mass at both ends, and a piezoelectric transducer mounted on the surface of the shaft at the location z_0 and angle α_p, as illustrated in Fig. 6.1. The overall length, inner radius, and thickness of the hollow shaft are denoted by L, r, and t_s, respectively. The radius and thickness of the flanges are specified as R and t_d. To simulate the real situation, a torsional excitation is applied to the flange at the right end of the shaft. The induced angular displacement at any point along the shaft is defined as $\gamma(z,t)$. The coordinate of the piezoelectric transducer is denoted by 1-2-3, which is aligned with the shaft coordinate $z-r-\theta$. The position parameter z_0 of the piezoelectric transducer is defined as the distance from the left corner of the piezoelectric transducer to the left end of the shaft, while α_p is the angle between axis 3 of the piezoelectric transducer and the longitudinal axis z of the shaft. The geometric sizes of the piezoelectric transducer are characterized by $l_1 \times l_3 \times t_p$.

Since the system is only subjected to the torque $\tau(t)$ around the z axis, the only nonzero strain appearing in the shaft is the shear strain $S_{z\theta}$, which can be related to the angular displacement $\gamma(z,t)$ of the shaft by the following equation.

$$S_{z\theta} = \gamma \frac{\partial \gamma}{\partial z} \tag{6.1}$$

The strain transferred to the piezoelectric transducer from the shaft completely depends on the pasted angle α_p. Given the fact that the thickness of the piezoelectric transducer is far less than its length and width, all the strain associated with the thickness direction (axis 2) is ignored in this study. Fig. 6.2 presents the normal and shear strain in the piezoelectric transducer, as well as the electrode tips. The transducer is assumed to be perfectly attached to the surface of the shaft, resulting in no relative motion between the transducer and the shaft. Particularly, if the piezoelectric transducer is placed at α_p=0° and 90°, the shear strain in the piezoelectric transducer is $S_{13} = S_{z\theta}$ and the normal strain $S_{11} = S_{33} = 0$. For the case of an arbitrary α_p, the strain in the piezoelectric transducer can be correlated with the strain at the covered surface of the shaft based on Mohr's Circle method, as shown in Fig. 6.3 [146]. In terms of the geometrical relationship illustrated in the Mohr's Circle, combining Eq. 6.1, the strain in piezoelectric transducer caused by the torsional vibration of the shaft can then be derived by

$$\underline{S} = \begin{bmatrix} S_{11} \\ S_{22} \\ S_{33} \\ S_{23} \\ S_{13} \\ S_{12} \end{bmatrix} = \begin{bmatrix} -\frac{\gamma}{2}\sin(2\alpha_p)\frac{S_{\theta z}}{2} \\ 0 \\ \frac{\gamma}{2}\sin(2\alpha_p)\frac{S_{\theta z}}{2} \\ 0 \\ -\frac{\gamma}{2}\cos(2\alpha_p)\frac{S_{\theta z}}{2} \\ 0 \end{bmatrix} = \begin{bmatrix} -\frac{\gamma}{2}\sin(2\alpha_p)\frac{\partial \gamma}{\partial z} \\ 0 \\ \frac{\gamma}{2}\sin(2\alpha_p)\frac{\partial \gamma}{\partial z} \\ 0 \\ -\frac{\gamma}{2}\cos(2\alpha_p)\frac{\partial \gamma}{\partial z} \\ 0 \end{bmatrix} \tag{6.2}$$

For the piezoelectric transducer in Fig. 6.2, the charges induced by the shear strain S_{13} for the d_{15} piezoelectric mode are concentrated on the first principle surfaces (perpendicular to axis 1). It is noteworthy that the strain S_{11} and S_{33} is not zero when the angle $\alpha_p \neq 0°$or 90°, which also induce charges for the d_{31} and d_{33} piezoelectric modes. Note that the intensity of the electric field is treated as constant across the thickness of the piezoelectric transducer,

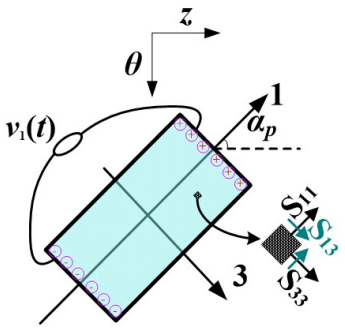

Figure 6.2: Piezoelectric transducer and strain analysis in 1-3 plane.

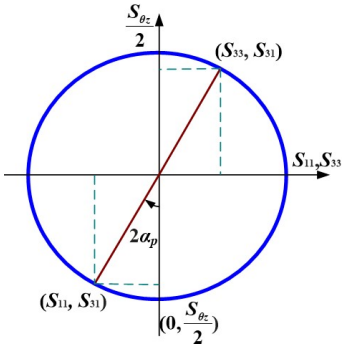

Figure 6.3: Mohr's Circle for the strain analysis in the piezoelectric transducer .

although there is the curvature on the transducer for perfectly mounting on the shaft surface. Assume the piezoelectric transducer is square ($l_1 = l_3$) and shunted by a circuit in parallel. The induced electric field intensity can be written in the following

$$\underline{E} = \begin{bmatrix} -\frac{v_1(t)}{l_1} & 0 & -\frac{v_1(t)}{l_1} \end{bmatrix} \tag{6.3}$$

The stress $\underline{\sigma}$ and electric displacement $\underline{D}$ in the piezoelectric transducer can be derived from the piezoelectric constitutive relationship as shown below [114, 147, 148]

$$\begin{bmatrix} \underline{\sigma} \\ \underline{D} \end{bmatrix} = \begin{bmatrix} C^E & -e^T \\ e & \varepsilon^s \end{bmatrix} \begin{bmatrix} \underline{S} \\ \underline{E} \end{bmatrix} \tag{6.4}$$

where C^E, e^T, and ε^S are the elasticity matrix, piezoelectric constant, and dielectric constant of the piezoelectric material, respectively, and T denotes transposition. The superscripts 'E' and 'S' declare that the corresponding elastic and dielectric parameters are measured at the constant electric field and strain environment.

Let ρ_s and ρ_p be the densities of the shaft and piezoelectric material, respectively. The

total kinetic energy of the torsional vibration system can be expressed as

$$T = \frac{1}{2}\int_{V_s} \rho_s r^2 \left(\frac{\partial \gamma}{\partial t}\right)^2 dV_s + \frac{1}{2}\int_{V_p} \rho_p r^2 \left(\frac{\partial \gamma}{\partial t}\right)^2 dV_p + \frac{1}{2}\Big[I_d\Big(\frac{\partial \gamma(0,t)}{\partial t}\Big)^2 + I_d\Big(\frac{\partial \gamma(L,t)}{\partial t}\Big)^2\Big] \tag{6.5}$$

where V_s and V_p denote the volumes of the shaft and piezoelectric transducer; I_d is the second moment of inertia of the flanges. The first two terms in the right-hand side of Eq. 6.5 are the kinetic energy of the shaft and piezoelectric transducer, respectively. The potential energy of the system is

$$U = \frac{1}{2}\int_{V_s} S_{z\theta}^T G_s S_{z\theta} dV_s + \frac{1}{2}\Big(\int_{V_p} \underline{S}^T C^E \underline{S} dV_p - \int_{V_p} \underline{S}^T e^T \underline{E} dV_p - \int_{V_p} \underline{E}^T \underline{D} dV_p \tag{6.6}$$

where G_s is the shear modulus of the shaft. Substitution of Eq. 6.1 into the first term in the right hand side of Eq. 6.6 yields the potential energy in the shaft as the following

$$U_s = \frac{1}{2}\int_{V_s} G_s r^2 \Big(\frac{\partial \gamma}{\partial z}\Big)^2 dV_s \tag{6.7}$$

while the potential energy in the piezoelectric material can be deduced by incorporating Eqs. 6.2-6.4 into the terms in the parenthesis of Eq. 6.6.

$$U_p = \frac{1}{2}\int_{V_p} \Big[\eta_1 r^2 \Big(\frac{\partial \gamma}{\partial z}\Big)^2 + \eta_2 r \Big(\frac{\partial \gamma}{\partial z}\Big) v_1(t) + (\,\epsilon_{11} + \epsilon_{33}) \left(\frac{v_1(t)}{l_1}\right)^2\Big] dV_p \tag{6.8}$$

in which the coefficients η_1 and η_2 are the functions of the material properties and attached angle of the piezoelectric transducer, as given in Eqs. (9) and (10), respectively.

$$\eta_1 = (\,C_{11} - 2C_{13} + C_{33})\,\sin^2(\,2\alpha_p) \,+ C_{55}\cos^2(\,2\alpha_p) \tag{6.9}$$

$$\eta_2 = \frac{1}{2l_1}\Big[(\,e_{31} - e_{33})\,\sin^2(\,2\alpha_p) \,- 2e_{15}\cos^2(\,2\alpha_p)\Big] \tag{6.10}$$

where C_{11}, C_{13}, C_{33}, and C_{55} are elastic constants of the piezoelectric material.

Eq. 6.8 shows that the coefficient η_2 measures the contribution of the electromechanical coupling term to the total potential energy. This indicates that η_2 actually characterizes the mechanical-to-electrical energy conversion performance of the system. It can be observed from Eq. 6.10 that the transducer works only in d_{15} mode for $\alpha_p = 0°$ and $90°$, in the coupled mode of d_{31} and d_{33} for $\alpha_p = 45°$, and in the coupled mode of d_{31}, d_{33} and d_{15} at any other angles.

The work done by both external force and electric load can be written as

$$W = \int_0^L \tau(t)\gamma dz - v_1(t)q_1(t) \tag{6.11}$$

where $\tau(t)$ is the applied torque along the length direction of the shaft and $v_1(t)$ and $q_1(t)$ are electric potential and applied surface charge to the piezoelectric transducer. The angular displacement $\gamma(z,t)$ is subjected to the Rayleigh-Ritz procedure. For the sake of simplicity, only the first vibration mode is considered in this study based on the fact that the fundamental mode dominantly contributes to the vibration in comparison with higher modes. Let $\underline{\phi}(z)$ denote the first torsional mode shape function of the shaft and $\underline{w}(t)$ denote the time- varying portion of the angular displacement. Thus, the angular displacement can be approximated as

$$\gamma(z,t) = \underline{\phi}(z)\underline{w}(t) \tag{6.12}$$

According to the Hamilton's principle [147, 148, 149], the dynamic system can be character-

ized by

$$\int_{t_0}^{t_1} \Big[\delta T - \delta U + \delta W\Big] dt \tag{6.13}$$

By substituting Eqs.6.5 - 6.11 into Eq. 6.13 and performing variational operation, one can obtain

$$\begin{aligned}
&\int_{t_0}^{t_1} \Bigg\{ \int_0^L \Bigg[-\rho_s I_s\Big(\frac{\partial^2\gamma}{\partial t^2}\Big) - \rho_p I_p\Big(\frac{\partial^2\gamma}{\partial t^2}\Big)\Delta\delta + G_s I_s\Big(\frac{\partial^2\gamma}{\partial z^2}\Big) + \eta_1 I_p\Big(\frac{\partial^2\gamma}{\partial z^2}\Big)\Delta\delta + \tau(t)\Bigg]\delta\gamma dz - \\
&\frac{1}{2}\int_{z_0}^{z_1} \eta_2 J_p\Big(\frac{\partial(\delta\gamma)}{\partial z} v_1(t) dz\Bigg\} dt - \int_{t_0}^{t_1} \Bigg\{ -I_d\frac{\partial^2\gamma}{\partial t^2}\Big|_0 - I_d\frac{\partial^2\gamma}{\partial t^2}\Big|^L - G_s I_s\Big(\frac{\partial\gamma}{\partial z}\Big)\Big|_0^L - \eta_1 I_p\Big(\frac{\partial\gamma}{\partial z}\Big|_{z_0}^{z_1}\Bigg\}\delta\gamma dt \\
&\int_{t_0}^{t_1} \Bigg\{ -\int_0^L \frac{1}{2}\eta_2 J_p\Big(\frac{\partial\gamma}{\partial z}\Delta\delta dz - C_p v_1(t) - q_1(t)\Bigg\}\delta v_1(t) dt = 0
\end{aligned} \tag{6.14}$$

where I_s and I_p are the second moments of inertia of the shaft and the piezoelectric transducer, respectively; $\Delta\delta = \delta(z - z_0) - \delta(z - z_1)$, in which δ denotes the delta function, while z_0 and z_1 are the coordinates of the two ends of the piezoelectric transducer; J_p is the first moment of inertia of the piezoelectric transducer with respect to the z-axis of the shaft. C_p is the equivalent capacitance of the transducer. Since $\delta\gamma$ is arbitrary, the boundary conditions of the torsional vibration system can be obtained from the terms in the second brace of Eq. 6.14 by ignoring the effect of the piezoelectric transducer as follows

$$I_d\frac{\partial^2\gamma}{\partial t^2} - G_s I_s\Big(\frac{\partial\gamma}{\partial z}\Big) = 0 \quad \text{at} \quad z = 0 \tag{6.15a}$$

$$I_d\frac{\partial^2\gamma}{\partial t^2} + G_s I_s\Big(\frac{\partial\gamma}{\partial z}\Big) = 0 \quad \text{at} \quad z = L \tag{6.15b}$$

By substituting Eq.6.12 into the terms in the first brace of Eq. 6.14 and further performing

variation, the equation of electromechanical motion of the system can be obtained by

$$M\ddot{\underline{w}}(t) + c\dot{\underline{w}}(t) + K\underline{w}(t) + \Omega v_1(t) = \tilde{\tau}(t) \tag{6.16}$$

where the mechanical damping has been added to the system by introducing a modal damping coefficient c. The equivalent mass, stiffness, electromechanical coupling coefficient and the modal torsional force are respectively given by

$$M = \int_0^L (\rho_s I_s + \rho_p I_p \Delta\delta)\, \underline{\phi}(z)\underline{\phi}(z)dz \tag{6.17}$$

$$K = -\int (G_s I_s + \eta_1 I_p \Delta\delta)\, \underline{\phi}''(z)\underline{\phi}(z) \tag{6.18}$$

$$\Omega = \frac{1}{2}\int_0^L \eta_2 J_p \underline{\phi}'(z)\Delta\delta dz \tag{6.19}$$

$$\tilde{\tau}(t) = \int_0^L \underline{\phi}(z)\tau(t)dz \tag{6.20}$$

Eqs. 6.18 and 6.19 indicate that the stiffness and the electromechanical coupling vector Ω of the system are correlated with the two uncertain position parameters α_p and z_0 of the piezoelectric transducer by the involvement of η_1 and η_2, respectively. However, the contribution of the piezoelectric transducer to the total stiffness of the system is substantially ignorable compared with the one of the shaft. When only a concentrated torque is applied to the right flange of the shaft, the modal force in Eq. 6.20 degenerates to

$$\tilde{\tau}(t) = \underline{\phi}(L)\tau(t) \tag{6.21}$$

Similarly, the electric function can be derived from the terms in the third brace of Eq. 6.14

by substituting Eq. 6.12 in

$$\Omega\underline{\dot{w}} + C_p\dot{v}_1(t) - \frac{v_1(t)}{R_L} = 0 \tag{6.22}$$

where the Ohm's law has been used to relate the charge to the external resistive load by $I(t) = -\frac{v_1(t)}{R_L}$. To describe the torsional vibration of the shaft with a flange at each end and satistfy the boundary conditions of Eqs. 6.15a and 6.15b, the following mode shape function is chosen [150].

$$\underline{\phi}(z) = \cos\frac{\beta z}{L} - m\beta\sin\frac{\beta z}{L} \tag{6.23}$$

where $m = \frac{I_d}{\rho_s L I_s}$ and β is the consecutive root of the following transcendental equation

$$\tan\beta = \frac{2m\beta}{(m\beta)^2 - 1} \tag{6.24}$$

Assume the shaft is subjected to a harmonic excitation $\tau(t) = \Gamma e^{j\omega t}$, where Γ and ω are the amplitude and frequency of the excitation, and j is the unit imaginary number. The steady state mechanical response of the shaft and electric voltage across the external resistive load are supposed to be harmonic at the same frequency given by $\underline{w}(t) = We^{j\omega t}$ and $v_1(t) = Ve^{j\omega t}$, where W and V are the amplitudes of the mechanical response and voltage output. By substituting the assumed solutions into Eqs. 6.16 and 6.22, one can obtain

$$W = \frac{\underline{\phi}(L)\Gamma/M - \Omega V/M}{\omega_1^2 + 2j\xi\omega_1\omega - \omega^2} \tag{6.25}$$

$$V = \frac{j\Omega W\omega/C_p}{j\omega + 1/(R_L C_p)} \tag{6.26}$$

where $\omega_1 = \sqrt{K/M}$ is the first angular natural frequency of the system, and ξ is the first modal damping ratio. The transfer function from the input torque to the amplitude of the

voltage output can be attained by substituting Eq. 6.26 into 6.25

$$\frac{|V|}{\Gamma} = \frac{\Omega \underline{\phi}(L)\omega/(\,MC_p)}{\sqrt{\left[\frac{\omega_1^2-\omega^2}{R_L C_p} + 2\xi\omega_1\omega^2\right]^2 + \left[\frac{\Omega^2}{MC_p} - (\,\omega_1^2 - \omega^2) + \frac{2\xi\omega_1}{R_L C_p}\right]^2 \omega^2}} \tag{6.27}$$

Thus, the normalized power flowing through the external resistive load is given by

$$P = \frac{|V|^2}{\Gamma^2 R_L} = \frac{\left[\Omega \underline{\phi}(L)\omega/(\,MC_p)\right]^2}{\sqrt{\left[\frac{\omega_1^2-\omega^2}{R_L C_p} + 2\xi\omega_1\omega^2\right]^2 + \left[\frac{\Omega^2}{MC_p} - (\,\omega_1^2 - \omega^2) + \frac{2\xi\omega_1}{R_L C_p}\right]^2 \omega^2}} \frac{1}{R_L} \tag{6.28}$$

In the above equations, three uncertain parameters need to be determined, including the external electrical resistance, piezoelectric transducer position parameters α_p and z_0 . Combining Eqs. 6.10, 6.19 and 6.28, it can be seen that the effect of the position of the piezoelectric transducer on the power output is indirectly concealed in the electromechanical coupling coefficient Ω. To extract as much power as possible, the three uncertainty parameters can be determined by setting the partial derivatives of the power with respect to the parameters to zero, i.e. $\frac{\partial P}{\partial R_L} = 0$, $\frac{\partial P}{\partial z_0} = \frac{\partial P}{\partial \Omega}\frac{\partial \Omega}{\partial z_0} = 0$, and $\frac{\partial P}{\partial \alpha_p} = \frac{\partial P}{\partial \Omega}\frac{\partial \Omega}{\partial \alpha_p} = 0$. However, analytically attaining the explicit expressions of the optimal position parameters from the above derivatives is a daunting task due to the involvement of the trigonometric functions of the parameter α_p. Nevertheless, the optimal external resistive load can be derived as the function of the position parameters as below

$$R_L^{opt} = \frac{1}{\omega C_p}\sqrt{\frac{(\,\omega_1^2 - \omega^2)^{\,2} + (\,2\xi\omega_1\omega)^{\,2}}{\left[\frac{\Omega^2}{MC_p} - (\,\omega_1^2 - \omega^2)\right]^2 + (\,2\xi\omega_1\omega)^{\,2}}} \tag{6.29}$$

Substituting the optimal resistance in Eq. 6.29 into Eqs. 6.27 and 6.28 gives the normalized voltage and power expressions, which are only characterized by the two unknown position

parameters α_p and z_0 in the electromechanical coupling coefficient Ω.

$$\frac{|V|}{\Gamma} = \frac{\underline{\phi}(L)\Omega/(MC_p)}{\sqrt{\left[(\omega_1^2-\omega^2)\Psi + 2\xi\omega_1\omega\right]^2 + \left[\frac{\Omega^2}{MC_p} - (\omega_1^2-\omega^2) + 2\xi\omega_1\omega\Psi\right]^2}} \tag{6.30}$$

$$P = \frac{\underline{\phi}^2(L)\Omega^2\omega\Psi/(M^2C_p)}{\left[(\omega_1^2-\omega^2)\Psi + 2\xi\omega_1\omega\right]^2 + \left[\frac{\Omega^2}{MC_p} - (\omega_1^2-\omega^2) + 2\xi\omega_1\omega\Psi\right]^2} \tag{6.31}$$

where $\Psi = \sqrt{\frac{\left[\frac{\Omega^2}{MC_p} - (\omega_1^2-\omega^2)\right]^2 + (2\xi\omega_1\omega)^2}{(\omega_1^2-\omega^2)^2 + (2\xi\omega_1\omega)^2}}$ is a coefficient related to the electromechanical coefficient Ω and the excitation frequency ω. Although the explicit expressions of the optimal position parameters cannot be directly attained by maximizing the generated power in Eq. 6.31, it is still possible to find the optimal values by parameter analysis. In general, the term $\frac{\Omega^2}{MC_p}$ is very small due to the very weak electromechanical coupling coefficient and thus is negligible compared with other terms in Ψ , resulting in $\Psi \approx 1$, in which case the optimal resistance, normalized voltage, and power can be approximately written as

$$R_L^{opt} \approx \frac{1}{\omega C_p} \tag{6.32}$$

$$\frac{|V|}{\Gamma} \approx \frac{\underline{\phi}(L)\Omega}{\sqrt{2}MC_p\sqrt{(\omega_1^2-\omega^2)^2 + (2\xi\omega_1\omega)^2}} \tag{6.33}$$

$$P \approx \frac{\underline{\phi}^2(L)\Omega^2\omega}{2M^2C_p\left[(\omega_1^2-\omega^2)^2 + (2\xi\omega_1\omega)^2\right]} \tag{6.34}$$

It is well known that the generated power will reach the maximum when the system is subjected to the resonant excitation ($\omega = \omega_1$), in which case Eqs. 6.30 and 6.31 become

$$\frac{|V|}{\Gamma} = \frac{\underline{\phi}(L)\Omega/(\,MC_p)}{\sqrt{\left(2\xi\omega_1^2\right)^2 + \left(2\xi\omega_1^2\tilde{\Psi} + \frac{\Omega^2}{MC_p}\right)^2}} \tag{6.35}$$

$$P = \frac{\underline{\phi}^2(L)\Omega^2\omega\tilde{\Psi}/(\,M^2C_p)}{\left(2\xi\omega_1^2\right) + \left(2\xi\omega_1^2\tilde{\Psi} + \frac{\Omega^2}{MC_P}\right)} \tag{6.36}$$

where $\tilde{\Psi} = \frac{\sqrt{[\Omega^2/(\,MC_p)\,^2]^2 + (2\xi\omega_1^2)^2}}{2\xi\omega_1^2}$. In reality, $\frac{\Omega^2}{MC_p} \ll 2\xi\omega_1^2$, which implies $\Psi \approx 1$. Eventually, Eqs. 6.35 and 6.36 can be approximately written as follows by ignoring the small terms.

$$\frac{|V|}{\Gamma} \approx \frac{\underline{\phi}(L)\Omega}{2\sqrt{2}MC_p\xi\omega_1^2} \tag{6.37}$$

$$P \approx \frac{\underline{\phi}^2(L)\Omega^2}{8C_pM^2\xi^2\omega_1^3} \tag{6.38}$$

The derived approximation Eqs. 6.37 and 6.38 of the normalized voltage and power, for the case of optimal resistive load and resonant excitation, are also functions of the two uncertain parameters α_p and z_0. The approximate expressions 6.37 and 6.38 can be conveniently used to estimate the harvested voltage and power. A parameter analysis could be performed to find the optimal values of the uncertain parameters corresponding to the maximum power output. The approximate expression 6.38 of the normalized power indicates that the harvested power is directly proportional to the square of the electromechanical coupling coefficient Ω and inversely proportional to the capacitance C_p of the piezoelectric transducer, the square of the mechanical modal damping ratio ξ, and the cube of the natural frequency. The electromechanical coupling coefficient Ω is nonlinearly characterized by α_p and z_0.

6.3 Experimental Setup and Validation

To verify the theoretical model and analysis, experiments are conducted on a prototype of the shaft with two flanges made of aluminum. The geometric and material properties of the prototype are given in Table 6.1. The piezoelectric transducer is purchased from EBL Products Inc. The geometric and material properties of the transducer are listed in Table 6.2. Three piezoelectric transducers are attached in the middle of the shaft along with the angles α_p=0°, 45°, and 90°, respectively. The epoxy hardener adhesive is used to bonded the piezoelectric transducers on the surface of the shaft. Special attention is needed to align the attaching angles of the transduces before the adhesive solidifies. In practice, the purely torsional excitation is hard to realize; thus, the impact force testing is performed on the prototype. An impulse force is applied tangentially to the edge of one of the flanges to excite the torsional mode of interest. To achieve the free-free boundary condition, the prototype is suspended on a designed frame structure by thin copper wires of negligible weight. A photograph and schematic diagram of the experimental setup are given in Fig. 6.4 (a) and (b). An ICP® Impact Hammer with a hard tip (Model 086C30) is used to provide the impulse force with the frequency range of interest. A plastic cable tie is fixed to the reserved hole near the edge of the flange to provide the excitation point. The impact force along the tangential direction of the flange is directly applied to the plastic cable tie. A Coco 80 Vibration Analyzer is adopted to record the frequency responses of the voltage generated by the piezoelectric transducers attached at the three different angles.

The measured voltage frequency responses of the transducers placed at α_p=0°, 45°, and 90° are plotted in Fig. 6.5 (a). It can be seen that the first natural frequency of the prototype is around 1425 Hz. The voltage frequency curve is smoother around the torsional frequency, but a little rough in other frequency range due to the very small voltage output and low signal-to-noise ratio. The simulated voltage responses for the piezoelectric transducers

Table 6.1: Geometric and material properties of the prototype.

Property	Symbol	Value
Length	L	152.4 mm
Inner radius of the shaft	r	14.9 mm
Thickness of the shaft	t_s	0.91 mm
Radius of the flanges	R	50.6 mm
Thickness of the flanges	t_d	3.2 mm
Density	$\rho_s = \rho_d$	2800 kg m^{-3}
Yang's modulus	E	68 GPa
Poisson ratio	μ	0.32

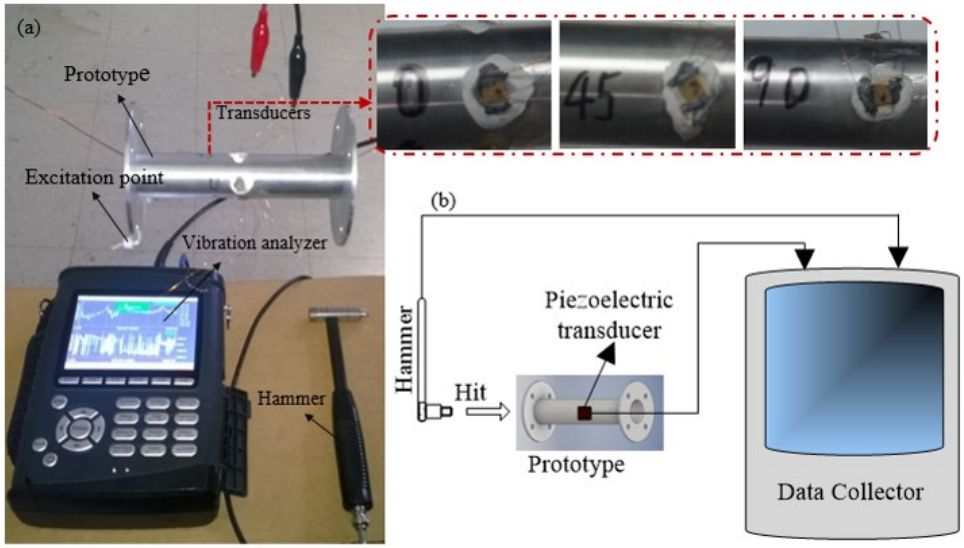

Figure 6.4: Experimental setup: (a) photograph and (b) schematic diagram.

attached at the three different angles are presented in Fig. 6.5 (b). For a fair comparison, the transfer function $\frac{|V|}{\Gamma}$ from the input torque to the amplitude of the voltage output in the numerical model is converted to $\frac{|V|}{F}$ by the relation between force and torque $\tau(t) = f(t)R$, where $f(t)$ is the applied force at the plastic cable tied near the outer edge of the flange. The first torsional resonance frequency attained from the theoretical model is 1446 Hz, which is very close to the experimental result.

Both the experimental and simulation results show that the normalized voltage responses

for α_p=0° and 90° are identical and larger than that of α_p=45°. This can be theoretically and physically elucidated as follows. Both the piezoelectric transducers attached at 0° and 90° work in d_{15} mode, since it can be found from Eq. 6.2 that the only non-zero strain in the transducer is S_{13} in such a case. Another reason is that the coefficient η_2 in Eq.6.10 determining the electromechanical coupling coefficient Ω only holds the term associated with the piezoelectric constant e_{15} when α_p=0° and 90°. Therefore, the transducers at α_p=0° and 90° are theoretically expected to give identical voltage output. For the case of α_p=45°, however, there are both S_{11} and S_{33} in the transducers, and only the term with $(e_{33} - e_{31})$ in the coefficient η_2 remains. For the selected PZT-5H material, it can be found from Table 6.2 that the values of the piezoelectric constant is slightly greater than $(e_{33} - e_{31})$ in Eq. 6.10, which can reasonably interpret the reason that the voltage output of the transducers at 0° and 90° is larger than the voltage output at 45°.

Table 6.2: Geometric and material properties of the piezoelectric transducer

Property	**Symbol**	**Value**
Length	l_1	5.0 mm
Width	l_2	5.0 mm
Thickness	t_p	0.1 mm
Density	ρ_p	7500 kgm^{-3}
Elastic constant	C_{11}	126 GPa
	C_{13}	84.1 GPa
	C_{33}	118 GPa
Piezoelectric constant	e_{31}	-6.5 Ccm^{-2}
	e_{33}	23.3 Ccm^{-2}
	e_{15}	17 Ccm^{-2}
Dielectric coefficients	ϵ_{11}	$1.503 \times 10^{-8} F$
	ϵ_{33}	$1.302 \times 10^{-8} F$

The difference between simulation and experiment results can be ascribed to the imperfect glue layer, for instance, different glue thicknesses and the imprecise pasted angles of the transducers. The theoretical model assumes that the harvester is perfectly attached to the

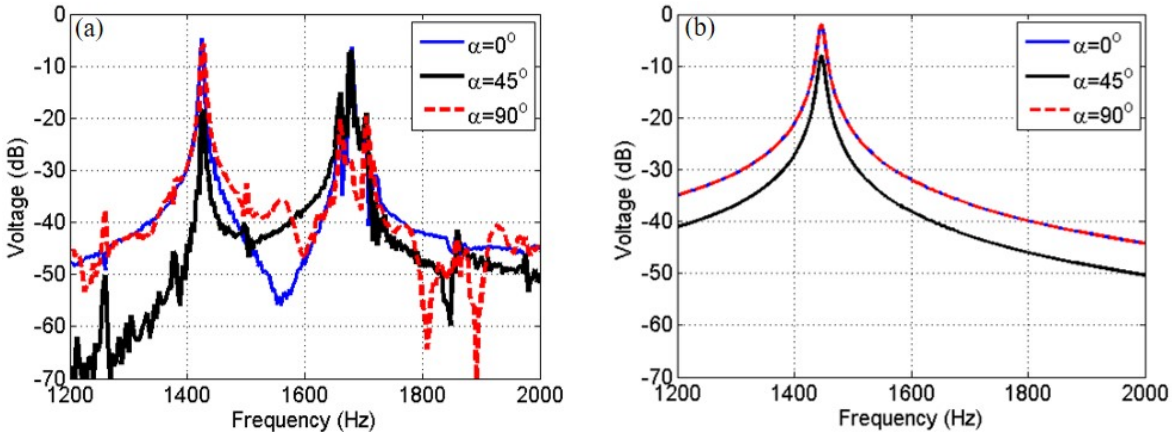

Figure 6.5: Voltage responses of the piezoelectric transducers attached at 0°, 45° and 90°: (a) Experiment and (b) Simulation.

shaft and neglects the glue layer. The stiffness of the glue layer is usually lower than that of the host structure, which results in the reduction of the strain transformed from the shaft to the harvester in real case. Thus, the theoretical voltages are larger than the experimental data.

Fig. 6.5 (a) and (b) display that the simulation result does not have the second peak at 1678Hz, because the second peak is not a torsional mode but is still experimentally captured. This is because the impact force is applied to the flange through the plastic tie at its edge in the experiment, which could induce the bending vibration of the shaft and the out-of-plane vibration of the flange, except for the torsional vibration. The bending vibration of the shaft is substantially inevitable in the current experiment method because the vertical force exerted at any point of the flange could always excite the bending mode of the shaft. The out-of-plane vibration of the flange is theoretically avoidable if the excitation force could be exactly applied along the tangent direction of the flange. However, it is hardly achievable to give a perfectly tangent excitation to the flange by hand hammer in the real world. The following finite element analysis illustrates that the second peak in the experiment data is

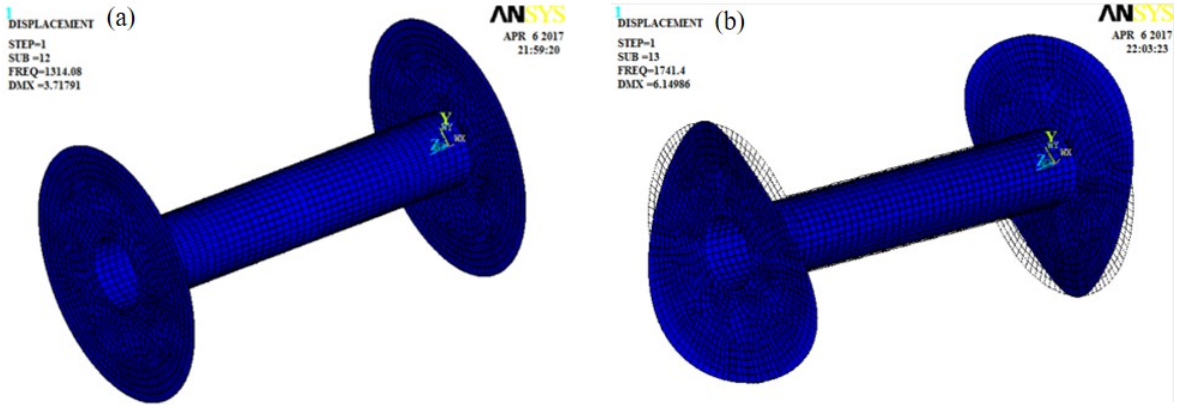

Figure 6.6: Finite element modal analysis results: (a) Torsional mode and (b) Coupled mode.

actually induced by the out-of-plane vibration of the flange.

To verify that, a finite element model of the shaft without the piezoelectric transducer is rendered in the commercial software ANSYS. Modal analysis is performed to identify the second vibration modal in Fig. 6.5 (a). The Shell63 element is used to model both the shaft and flanges, and a total 3386 nodes and 3286 elements are created in the model. The numerical results of the modal analysis are presented in Fig. 6.6 (a) and (b), which show that the second model in the experimental result is a coupled vibration mode of the flanges and shaft. The torsional and coupling vibration frequencies obtained from the numerical model are 1314 Hz and 1741 Hz, respectively. The error between the FE simulated torsional frequency and the experiment result is around 7.8%.

Harmonic analysis is conducted based on the FE model with two load cases. Firstly, a unit force is applied to the excitation point at the edge of the flange along the tangent direction, which is expected to create pure torsional vibration. Then an additional unit force is exerted at the same point, but along the shaft length direction (perpendicular to the flange plane), to excite the coupling torsional vibration and out-of-plane vibration of the flange. Fig. 6.7 presents the displacement frequency responses of the shaft at the two load cases. It

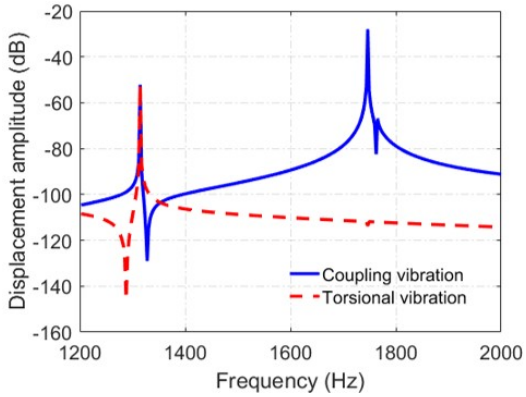

Figure 6.7: Torsional displacement frequency responses.

can be seen that only the torsional mode response shows up when the force is applied along the tangent direction of the flange, which is in accordance with the theoretical solution and above discussion. When both the tangent and out-of-plane forces are applied, two peaks can be observed from the frequency response due to the coupling torsional and out-of-plane vibrations of the flange. This confirms the experiment results and the above analysis.

6.4 Numerical Results and Parameter Analysis

Based on Eqs. 6.27 and 6.28, the generated voltage and power for varying external resistive loads are presented in Fig. 6.8 (a) and (b) for the resonant excitation, respectively. Note that the power mentioned hereafter is normalized with respect to the squared input force instead of the torque used to normalize the voltage mentioned in the section of Experimental Setup and Model Validation. Simulation results show that the voltage outputs of the harvesters at α_p=0° and 90° have identical values, but opposite signs. For convenient comparison, Fig. 6.8 presents the absolute value of the voltage output for the case of α_p=0°. It is shown that the voltage across varying resistive loads is always identical in values for α_p=0° and 90°, and greater than the voltage for α_p=45°. The optimal resistance corresponding to the maximum

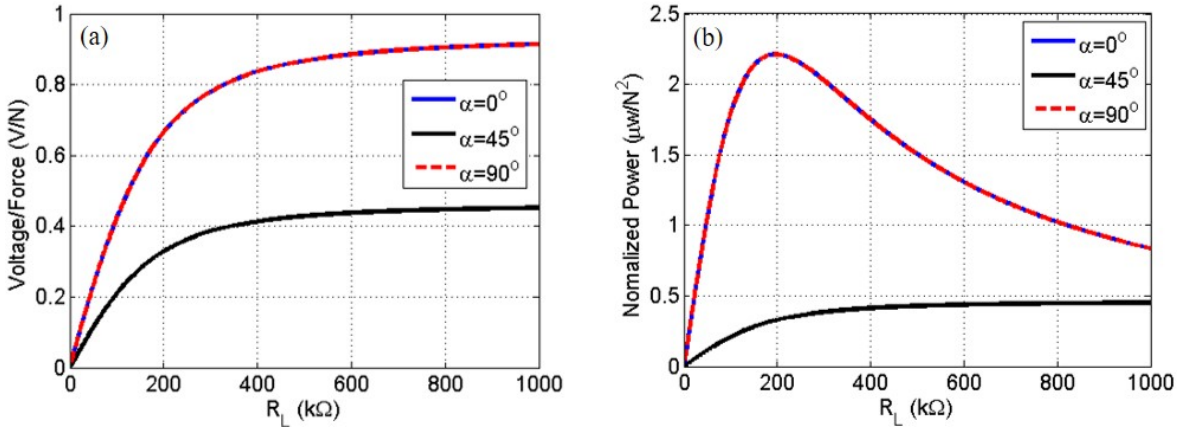

Figure 6.8: Predicted voltage and power for the piezoelectric transducers attached at different resistive loads: (a) Voltage and (b) power.

power is found at 200 kΩ approximately, which agrees with the theoretically optimal value calculated from Eq. 6.29.

Since the performance of the harvesters with the transducers at α_p=0° and 90° are identical and outperform the one with the transducer at α_p=45°, the following studies only focus on the model with the transducer at α_p=0° for concision. The voltage and power obtained from Eqs. 6.30 and 6.31 for the system with the optimal resistance are respectively plotted in Fig. 6.9 (a) and (b). The results show that the maximum voltage and power outputs occur at the resonant excitation, and the results obtained from the approximate equations match well with the analytical responses. This proves that the term $\frac{\Omega^2}{MC_p}$ in the analytical equations is small and ignorable. The resultant approximate equations are practical and can be used to estimate the transducer's voltage and power output.

Parameter analysis is performed to investigate the harvested voltage and power of the piezoelectric transducer for different values of the position parameters α_p and z_0 based on the derived approximate equations. To examine the maximum power output, the parameter analysis is conducted at the case of resonant vibration and optimal resistance. The voltage

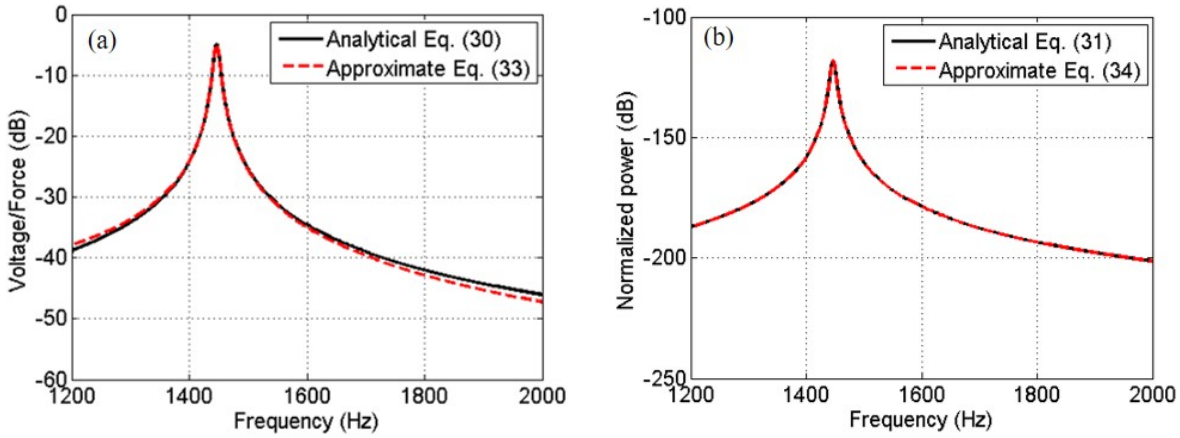

Figure 6.9: Analytical and approximate responses of (a) voltage and (b) power.

and power obtained from the analytical Eqs. 6.35 and 6.36 are given in Fig. 6.10 (a) and (b). It can be seen that both the voltage and power slightly increase as the position z_0 along with the shaft increases, and have the maximum values when α_p is approximately 15°. When the attached angle is about 60°, the harvested power is the lowest. It can also be observed that the voltages at α_p=0° and 90° are identical in values but opposite in signs, and greater than the voltage harvested from the transducer at 45°, which is in accordance with the previous experimental and theoretical results. The estimated voltage and power from the approximate Eqs. 6.37 and 6.38 are presented in Fig. 6.11 (a) and (b), respectively. Good agreement can be found between the analytical solutions and the estimated voltage and power over varying parameters α_p and z_0. This indicates the derived approximate equations can be used for further parameter analysis. In the approximate power Eq. 6.38, only the electromechanical coupling coefficient Ω and the frequency are related to the parameters α_p and z_0. The effect of parameter α_p on the natural frequency of the system depends on the coefficient η_1 in Eq. 6.9, which is involved in the total stiffness of the system, as shown in the Eq.6.18. Generally, the stiffness of the piezoelectric transducer is too little to compete with the one of the host shaft due to its small size. Thus, its contribution to natural frequency can be neglected

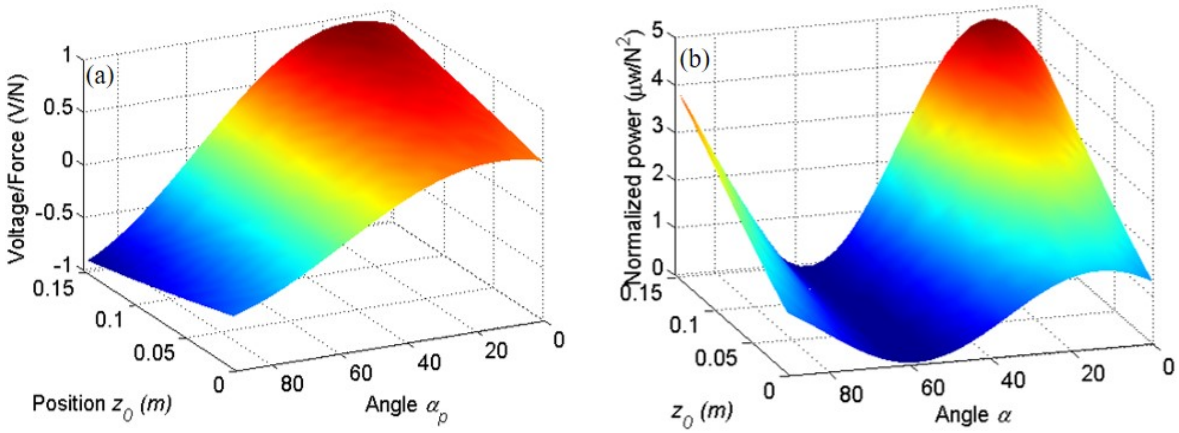

Figure 6.10: Analytical solutions for varying position parameters α_p and z_0. (a) voltage and (b) power.

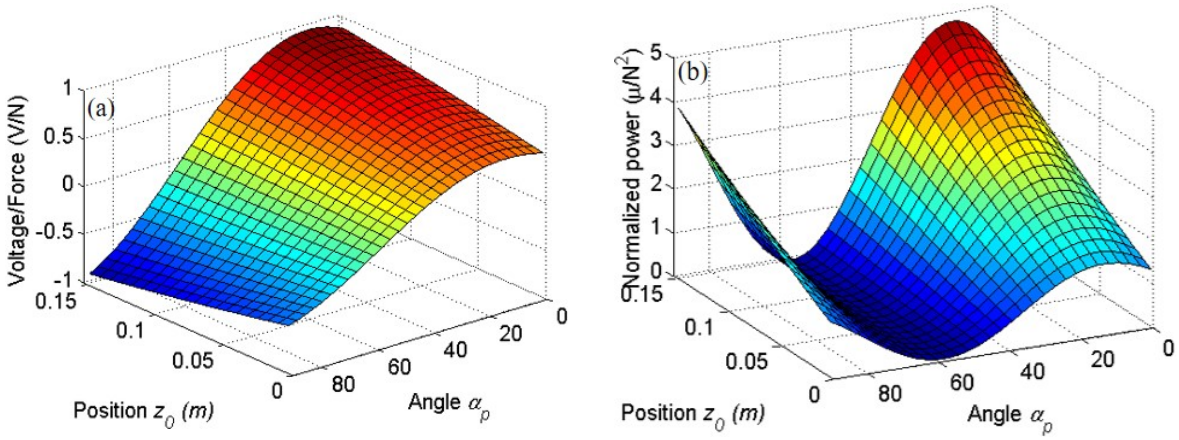

Figure 6.11: Approximate results for varying position parameters α_p and z_0. (a) voltage and (b) power.

compared with the host structure's contribution. This implies the effect of the parameter α_p on the frequency can be ignored. In such case, the normalized power is dominantly characterized by the two parameters only through the electromechanical coupling coefficient Ω. From Eq. 6.19 it is not difficult to find that Ω is determined by α_p and z_0 through the coefficient η_2 in Eq. 6.10 and the integral of the derivative of the mode function $\underline{\phi}(z)$.

Fig. 6.12 (a) illustrates the variation of η_2 over different values of α_p, which shows that the coefficient η_2 has the maximum magnitude at around $\alpha_p \approx 15°$, indicating that the transducer synchronously works at d_{33}, d_{31} and d_{15} modes. Eq. 6.38 shows that the normalized power P has a proportional relation with the square of the electromechanical coefficient Ω, which is in direct proportion to η_2 and the integral of the derivative of the mode function. This gives a reasonable interpretation of the previous results that the normalized power reaches the maximum at $\alpha_p \approx 15°$. Furthermore, it is interesting to find that the values of η_2 at both $\alpha_p \approx 0°$ and $90°$ are also identical in values and opposite in signs. To understand the influence of the position parameter z_0 on the power, the integral $I_n = \int \underline{\phi}'(z)dz$ involved in the electromechanical coefficient Ω, for an example case $\alpha_p = 0°$ is given in Fig. 6.12 (b) over different values of z_0. It is shown that the absolute value of the integral slightly increases as the position parameter z_0 increases, which interprets the reason that the position of the transducer along the length direction has a small effect on the voltage and power outputs.

6.5 Chapter summary

This chapter presents theoretical modeling and experimental verification of a piezoelectric torsional vibration energy harvester attached on a shaft. The analytical expressions of the optimal resistance, normalized voltage, and power are obtained as functions of the transducer's position parameters. Parameter analysis is conducted to find the transducer's optimal

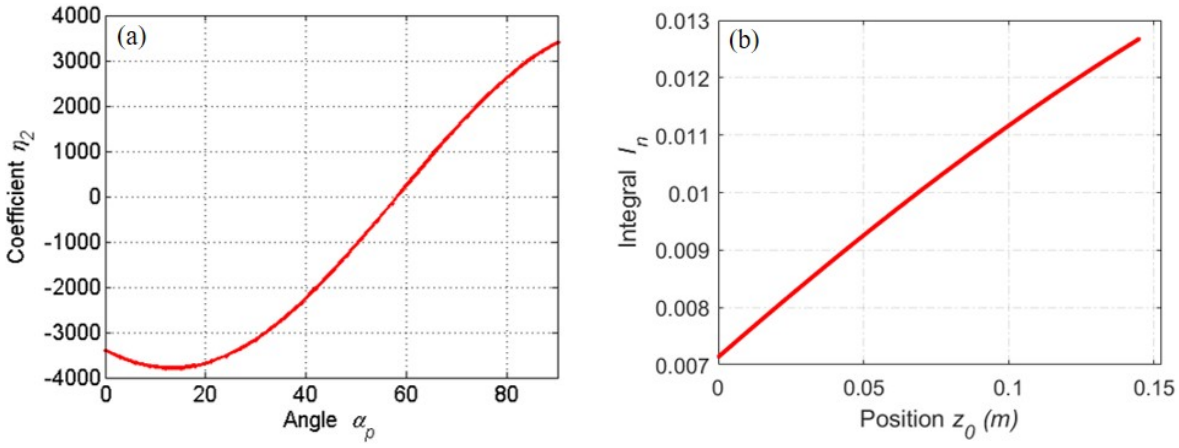

Figure 6.12: (a) Coefficient η_2 for varying α_p and (b) the integral $I_n = \int \underline{\phi}'(z)dz$ for different z_0.

position, which can generate the maximum power from torsional vibrations. The theoretical model can give reliable predictions of the voltage and power output of the piezoelectric transducers attached at different angles on the shaft. The position parameter z_0 of the transducer has little effect on the power output, while the pasting angle of the transducer α_p significantly influences the energy harvesting performance. The optimal position and angle of the transducer are found at the end of the shaft and $\alpha_p \approx 15°$, in which case, the transducer synchronously works in d_{33}, d_{31} and d_{15} modes. The established theoretical model is proven to be capable of estimating the voltage and power output. The explicit correlation between the power output and the transducer's position parameters is interpreted and discussed based on the approximate power expression.

Chapter 7

Conclusion and future directions

7.1 Conclusion

Three novel piezoelectric energy harvesters are proposed, designed, modeled, prototyped, and tested in this dissertation by exploring compliant force amplification mechanisms, bio-inspired bi-stable motion, and various piezoelectric modes to provide a sustainable power supply for different wireless monitoring systems. A footwear piezoelectric energy harvester consisting of multiple piezoelectric stacks in d_{33} mode and single-stage force amplifiers is developed, modeled, and validated to be capable of scavenging energy from human walking. The footwear piezoelectric energy harvester energy could provide a continuous power supply for wearable sensors integrated in wireless monitoring systems for living assistance, health status promotion, and rehabilitation. The single-stage force amplification frame, designed and optimized for large power output, redirects the vertical dynamic forces at a heel into the horizontal direction, meanwhile amplifies and transmits the forces to the inner piezoelectric stack transducer. An analytical model only considering the piezoelectric stacks and a symmetric finite element model considering both the piezoelectric stack and force amplifi-

cation frame are developed to simulate the electromechanical coupling behavior. A material equivalent model is developed to simplify the multilayer piezoelectric stack into bulk to facilitate the mesh in the FE modeling. The harvester generates 8 mW/shoe, 9 mW/shoe, and 14 mW/shoe at the walking speeds of 2.5 mph (4.0 km/h), 3.0 mph (4.8 km/h) and 3.5 mph (5.6 km/h), respectively. The parametric study performed on the experimentally validated FE model indicates that the force amplification frame's geometric dimensions have significant effects on the performance of the piezoelectric footwear energy harvester.

To further improve the power output of the piezoelectric footwear energy harvester, a two-stage force amplification mechanism is proposed to substitute the single-stage force amplifier so that the dynamic force at the heel is amplified twice and then applied to the innermost piezoelectric stacks. In-lab experiments and numerical simulations were conducted to evaluate the performance of the two-stage piezoelectric energy harvester over different load levels, frequencies, and human walking speeds. 23.86 mW and 10.96 mW average power outputs were experimentally achieved at 2 Hz and 1 Hz, respectively. A comparison study showed that the proposed two-stage piezoelectric energy harvester outperformed the existing piezoelectric shoe harvesters in power generation.

To harvest energy from broadband vibrations such as animal motions and fluid flowing, a bio-inspired bi-stable piezoelectric energy harvester is designed, prototyped, and tested for the potential applications of self-powered fish telemetry tags and bird tags. Inspired by the rapid shape transition of the Venus flytrap leaves, a cantilever beam is cut into two sub-beams, which are bent and twisted by an in-plane pre-displacement applied at the free ends to induce the potential energy and achieve the bi-stability. The harvester consists of a piezoelectric macro fiber composite (MFC) transducer, a tip mass, and two sub-beams with bending and twisting deformations created by pre-displacement constraints at the free ends using rigid tip-mass blocks. Different from bi-stable harvesters realized by nonlinear magnetic

forces or residual stresses in laminated composites, the bio-inspired bi-stable piezoelectric energy harvester stores the potential energy induced by the mutual self-constraint of the sub-beams and harvests the large energy released during the rapid shape transition. Detailed design steps and principles are introduced, and a prototype is fabricated to demonstrate and validate the concept. The experimentally measured nonlinear force-displacement curve of the harvester exhibits a discontinuous feature as the harvester jumps between the stable states. The dynamics of the proposed bio-inspired bi-stable piezoelectric energy harvester is investigated under sweeping frequency and harmonic excitations. The results show that the sub-beams of the harvester experience local vibrations, including broadband high-frequency oscillations during the snap-through. The energy harvesting performance of the harvester is evaluated at different excitation levels over the frequency range of 9.0-14.0 Hz. Broadband energy harvesting is attained at relatively high excitation levels. An average power output of 0.193 mW for a load resistance of 8.2 kΩ is harvested at the excitation frequency of 10 Hz and amplitude of 4.0 g.

A torsional vibration energy harvester is developed, analytically modeled, and validated for harvesting energy from a drilling shaft rotation to provide a continuous power supply for downhole sensors in oil drilling monitoring systems. The piezoelectric transducer position on the shaft surface is parameterized by two variables that are optimized to obtain the maximum power output. Analytical analysis shows that the piezoelectric transducer works in d_{15} mode (pure shear mode), coupled mode of d_{31} and d_{33}, and coupled mode of d_{33}, d_{31} and d_{15}, respectively, when attached at different angles. Approximate expressions of voltage and power are derived from the theoretical model, which give predictions in good agreement with analytical solutions. The implicit relationship between the power output and the two position parameters of the piezoelectric transducer is revealed and physically interpreted based on the approximate power expression. The results show that the optimal position

of the piezoelectric transducer locates at the end of the shaft and 15°, in which case, the transducer works in the coupled mode of d_{33}, d_{31} and d_{15} modes. Those findings offer a valuable reference for the practical design of torsional vibration energy harvesting systems.

7.2 Future directions

One problem in the energy harvesting from human walking is the frequency mismatch between human walking frequency and the footwear energy harvester. Human walking frequency is very low, around 1 Hz, but the natural frequency of the piezoelectric stacks used in the footwear energy harvester is up to thousands of Hz. Therefore, the harvester always operates at an off-resonance state and therefore has very low energy conversion efficiency. One potential direction to explore in the future is to develop proper frequency up-conversion strategies to bridge the gap between the human walking frequency and the natural frequency of the harvester.

The research on the bio-inspired bi-stable harvester mainly remains at experimental studies and concept validation currently, which is lack of theoretical basis and insight analysis desired for parameter design. Future efforts will move on to the theoretical analysis and numerical modeling to improve the design and energy harvesting performance. Another interesting direction is to expand the bio-inspired bi-stable structure to multiple stable harvesters by combing multiple bi-stable structures to extend the frequency bandwidth further. The proposed bio-inspired bi-stable harvester is easily manufactured and without the involvement of magnetic field compared with the bi-stable piezoelectric energy harvesters made of magnets or composite laminates; therefore, it is more convenient to be deployed in various ambient environments. For example, a downsized bio-inspired bi-stable harvester could be integrated into an externally deployed fish telemetry tag to scavenge energy from fish motion

and surrounding fluid flow. In such a case, more challenging scientific problems related to piezoelectric-fluid-bi-stable-structure coupling dynamics will be worthy of exploring in the future.

Bibliography

[1] Viet, N., and Wang, Q., 2018. "Ocean wave energy pitching harvester with a frequency tuning capability". *Energy,* ***162***, pp. 603–617.

[2] Zuo, L., Scully, B., Shestani, J., and Zhou, Y., 2010. "Design and characterization of an electromagnetic energy harvester for vehicle suspensions". *Smart Materials and Structures,* ***19***(4), p. 045003.

[3] Ylli, K., Hoffmann, D., Willmann, A., Becker, P., Folkmer, B., and Manoli, Y., 2015. "Energy harvesting from human motion: exploiting swing and shock excitations". *Smart Materials and Structures,* ***24***(2), p. 025029.

[4] Wang, W., Cao, J., Zhang, N., Lin, J., and Liao, W.-H., 2017. "Magnetic-spring based energy harvesting from human motions: Design, modeling and experiments". *Energy Conversion and Management,* ***132***, pp. 189–197.

[5] Pan, Y., Lin, T., Qian, F., Liu, C., Yu, J., Zuo, J., and Zuo, L., 2019. "Modeling and field-test of a compact electromagnetic energy harvester for railroad transportation". *Applied Energy,* ***247***, pp. 309–321.

[6] Moro, L., and Benasciutti, D., 2010. "Harvested power and sensitivity analysis of vibrating shoe-mounted piezoelectric cantilevers". *Smart Materials and Structures,* ***19***(11), p. 115011.

[7] Jiang, X.-Y., Zou, H.-X., and Zhang, W.-M., 2017. "Design and analysis of a multi-step piezoelectric energy harvester using buckled beam driven by magnetic excitation". *Energy Conversion and Management,* ***145***, pp. 129–137.

[8] Zhao, J., and You, Z., 2014. "A shoe-embedded piezoelectric energy harvester for wearable sensors". *Sensors,* ***14***(7), pp. 12497–12510.

[9] Lu, Y., Cottone, F., Boisseau, S., Marty, F., Galayko, D., and Basset, P., 2015. "A nonlinear mems electrostatic kinetic energy harvester for human-powered biomedical devices". *Applied Physics Letters,* ***107***(25), p. 253902.

[10] Mule, A. R., Dudem, B., and Yu, J. S., 2018. "High-performance and cost-effective triboelectric nanogenerators by sandpaper-assisted micropatterned polytetrafluoroethylene". *Energy,* ***165***, pp. 677–684.

[11] Wu, Y., Zhang, H., and Zuo, L., 2018. "Thermoelectric energy harvesting for the gas turbine sensing and monitoring system". *Energy conversion and management,* ***157***, pp. 215–223.

[12] Harb, A., 2011. "Energy harvesting: State-of-the-art". *Renewable Energy,* ***36***(10), pp. 2641–2654.

[13] Beeby, S. P., Tudor, M. J., and White, N., 2006. "Energy harvesting vibration sources for microsystems applications". *Measurement science and technology,* ***17***(12), p. R175.

[14] Zuo, L., and Tang, X., 2013. "Large-scale vibration energy harvesting". *Journal of intelligent material systems and structures,* ***24***(11), pp. 1405–1430.

[15] Siddique, A. R. M., Mahmud, S., and Van Heyst, B., 2015. "A comprehensive review on vibration based micro power generators using electromagnetic and piezoelectric transducer mechanisms". *Energy Conversion and Management,* ***106***, pp. 728–747.

[16] Shaikh, F. K., and Zeadally, S., 2016. "Energy harvesting in wireless sensor networks: A comprehensive review". *Renewable and Sustainable Energy Reviews,* ***55***, pp. 1041–1054.

[17] Wei, C., and Jing, X., 2017. "A comprehensive review on vibration energy harvesting: Modelling and realization". *Renewable and Sustainable Energy Reviews,* ***74***, pp. 1–18.

[18] Liang, J., and Liao, W.-H., 2010. "Energy flow in piezoelectric energy harvesting systems". *Smart Materials and Structures,* ***20***(1), p. 015005.

[19] Harne, R., 2013. "Development and testing of a dynamic absorber with corrugated piezoelectric spring for vibration control and energy harvesting applications". *Mechanical Systems and Signal Processing,* ***36***(2), pp. 604–617.

[20] Tang, X., and Zuo, L., 2012. "Simultaneous energy harvesting and vibration control of structures with tuned mass dampers". *Journal of Intelligent Material Systems and Structures,* ***23***(18), pp. 2117–2127.

[21] Qian, F., Luo, Y., Sun, H., Tai, W. C., and Zuo, L., 2019. "Optimal tuned inerter dampers for performance enhancement of vibration isolation". *Engineering Structures,* ***198***, p. 109464.

[22] Li, Z., Zuo, L., Luhrs, G., Lin, L., and Qin, Y.-x., 2012. "Electromagnetic energy-harvesting shock absorbers: design, modeling, and road tests". *IEEE Transactions on vehicular technology,* ***62***(3), pp. 1065–1074.

[23] Ali, S. F., and Adhikari, S., 2013. "Energy harvesting dynamic vibration absorbers". *Journal of Applied Mechanics,* ***80***(4).

[24] Lesieutre, G. A., Ottman, G. K., and Hofmann, H. F., 2004. "Damping as a result of

piezoelectric energy harvesting". *Journal of sound and vibration,* ***269***(3-5), pp. 991–1001.

[25] Li, X., Zhang, Y., Ding, H., and Chen, L., 2017. "Integration of a nonlinear energy sink and a piezoelectric energy harvester". *Applied Mathematics and Mechanics,* ***38***(7), pp. 1019–1030.

[26] Zhang, Y., Tang, L., and Liu, K., 2017. "Piezoelectric energy harvesting with a nonlinear energy sink". *Journal of Intelligent Material Systems and Structures,* ***28***(3), pp. 307–322.

[27] Qian, F., Zhou, W., Kaluvan, S., Zhang, H., and Zuo, L., 2018. "Theoretical modeling and experimental validation of a torsional piezoelectric vibration energy harvesting system". *Smart Materials and Structures,* ***27***(4), p. 045018.

[28] Chen, Y.-C., Cheng, C.-K., and Shen, S.-C., 2019. "Design and fabrication of a displacement sensor using screen printing technology and piezoelectric nanofibers in d33 mode". *Sensors and Materials,* ***31***(2), pp. 233–244.

[29] Liu, H., Zhong, J., Lee, C., Lee, S.-W., and Lin, L., 2018. "A comprehensive review on piezoelectric energy harvesting technology: Materials, mechanisms, and applications". *Applied Physics Reviews,* ***5***(4), p. 041306.

[30] Shu, Y., Lien, I., and Wu, W., 2007. "An improved analysis of the sshi interface in piezoelectric energy harvesting". *Smart Materials and Structures,* ***16***(6), p. 2253.

[31] Lien, I., Shu, Y., Wu, W., Shiu, S., and Lin, H., 2010. "Revisit of series-sshi with comparisons to other interfacing circuits in piezoelectric energy harvesting". *Smart Materials and Structures,* ***19***(12), p. 125009.

[32] Sue, C.-Y., and Tsai, N.-C., 2012. "Human powered mems-based energy harvest devices". *Applied Energy,* ***93***, pp. 390–403.

[33] Cai, M., Liao, W.-H., and Cao, J., 2018. "A smart harvester for capturing energy from human ankle dorsiflexion with reduced user effort". *Smart Materials and Structures,* ***28***(1), p. 015026.

[34] Chen, C., Chau, L. Y., and Liao, W.-H., 2017. "A knee-mounted biomechanical energy harvester with enhanced efficiency and safety". *Smart Materials and Structures,* ***26***(6), p. 065027.

[35] Zhao, L.-C., Zou, H.-X., Yan, G., Liu, F.-R., Tan, T., Wei, K.-X., and Zhang, W.-M., 2019. "Magnetic coupling and flextensional amplification mechanisms for high-robustness ambient wind energy harvesting". *Energy Conversion and Management,* ***201***, p. 112166.

[36] Pozzi, M., and Zhu, M., 2011. "Plucked piezoelectric bimorphs for knee-joint energy harvesting: modelling and experimental validation". *Smart Materials and Structures,* ***20***(5), p. 055007.

[37] Cao, J., Wang, W., Zhou, S., Inman, D. J., and Lin, J., 2015. "Nonlinear time-varying potential bistable energy harvesting from human motion". *Applied Physics Letters,* ***107***(14), p. 143904.

[38] Yang, Z., Wang, Y. Q., Zuo, L., and Zu, J., 2017. "Introducing arc-shaped piezoelectric elements into energy harvesters". *Energy conversion and management,* ***148***, pp. 260–266.

[39] Kuang, Y., Ruan, T., Chew, Z. J., and Zhu, M., 2017. "Energy harvesting during

human walking to power a wireless sensor node". *Sensors and Actuators A: Physical,* ***254***, pp. 69–77.

[40] Hou, T.-C., Yang, Y., Zhang, H., Chen, J., Chen, L.-J., and Wang, Z. L., 2013. "Triboelectric nanogenerator built inside shoe insole for harvesting walking energy". *Nano Energy,* ***2***(5), pp. 856–862.

[41] Kuang, Y., Yang, Z., and Zhu, M., 2016. "Design and characterisation of a piezoelectric knee-joint energy harvester with frequency up-conversion through magnetic plucking". *Smart Materials and Structures,* ***25***(8), p. 085029.

[42] Qian, F., Xu, T.-B., et al., 2018. "A distributed parameter model for the piezoelectric stack harvester subjected to general periodic and random excitations". *Engineering Structures,* ***173***, pp. 191–202.

[43] Yang, R., Qin, Y., Li, C., Zhu, G., and Wang, Z. L., 2009. "Converting biomechanical energy into electricity by a muscle-movement-driven nanogenerator". *Nano letters,* ***9***(3), pp. 1201–1205.

[44] Xin, Y., Tian, H., Guo, C., Li, X., Sun, H., Wang, P., Qian, C., Wang, S., and Wang, C., 2016. "A biomimetic tactile sensing system based on polyvinylidene fluoride film". *Review of Scientific Instruments,* ***87***(2), p. 025002.

[45] Qian, F., Xu, T.-B., and Zuo, L., 2018. "Design, optimization, modeling and testing of a piezoelectric footwear energy harvester". *Energy conversion and management,* ***171***, pp. 1352–1364.

[46] Kymissis, J., Kendall, C., Paradiso, J., and Gershenfeld, N., 1998. "Parasitic power harvesting in shoes". In Digest of Papers. Second International Symposium on Wearable Computers (Cat. No. 98EX215), IEEE, pp. 132–139.

[47] Shenck, N. S., and Paradiso, J. A., 2001. "Energy scavenging with shoe-mounted piezoelectrics". *IEEE micro,* ***21***(3), pp. 30–42.

[48] Mateu, L., and Moll, F., 2005. "Optimum piezoelectric bending beam structures for energy harvesting using shoe inserts". *Journal of Intelligent Material Systems and Structures,* ***16***(10), pp. 835–845.

[49] Fan, K., Liu, Z., Liu, H., Wang, L., Zhu, Y., and Yu, B., 2017. "Scavenging energy from human walking through a shoe-mounted piezoelectric harvester". *Applied Physics Letters,* ***110***(14), p. 143902.

[50] Kuang, Y., Daniels, A., and Zhu, M., 2017. "A sandwiched piezoelectric transducer with flex end-caps for energy harvesting in large force environments". *Journal of Physics D: Applied Physics,* ***50***(34), p. 345501.

[51] Cha, Y., and Seo, J., 2018. "Energy harvesting from a piezoelectric slipper during walking". *Journal of Intelligent Material Systems and Structures,* ***29***(7), pp. 1456–1463.

[52] González, J. L., Rubio, A., and Moll, F., 2002. "Human powered piezoelectric batteries to supply power to wearable electronic devices". *International journal of the Society of Materials Engineering for Resources,* ***10***(1), pp. 34–40.

[53] Chen, S.-N., Wang, G.-J., and Chien, M.-C., 2006. "Analytical modeling of piezoelectric vibration-induced micro power generator". *Mechatronics,* ***16***(7), pp. 379–387.

[54] Tang, L., and Yang, Y., 2012. "A multiple-degree-of-freedom piezoelectric energy harvesting model". *Journal of Intelligent Material Systems and Structures,* ***23***(14), pp. 1631–1647.

[55] Xu, T.-B., Siochi, E. J., Kang, J. H., Zuo, L., Zhou, W., Tang, X., and Jiang, X., 2013. "Energy harvesting using a pzt ceramic multilayer stack". *Smart Materials and Structures,* ***22***(6), p. 065015.

[56] Erturk, A., and Inman, D. J., 2009. "An experimentally validated bimorph cantilever model for piezoelectric energy harvesting from base excitations". *Smart materials and structures,* ***18***(2), p. 025009.

[57] Azizi, S., Ghodsi, A., Jafari, H., and Ghazavi, M. R., 2016. "A conceptual study on the dynamics of a piezoelectric mems (micro electro mechanical system) energy harvester". *Energy,* ***96***, pp. 495–506.

[58] Zhou, W., Penamalli, G. R., and Zuo, L., 2011. "An efficient vibration energy harvester with a multi-mode dynamic magnifier". *Smart Materials and Structures,* ***21***(1), p. 015014.

[59] Xie, X., Carpinteri, A., and Wang, Q., 2017. "A theoretical model for a piezoelectric energy harvester with a tapered shape". *Engineering Structures,* ***144***, pp. 19–25.

[60] Xie, X., Wang, Q., and Wu, N., 2014. "Energy harvesting from transverse ocean waves by a piezoelectric plate". *International Journal of Engineering Science,* ***81***, pp. 41–48.

[61] Jansen, J. D., and Van Den Steen, L., 1995. "Active damping of self-excited torsional vibrations in oil well drillstrings". *Journal of sound and vibration,* ***179***(4), pp. 647–668.

[62] Wei, S., Zhao, J., Han, Q., and Chu, F., 2015. "Dynamic response analysis on torsional vibrations of wind turbine geared transmission system with uncertainty". *Renewable Energy,* ***78***, pp. 60–67.

[63] Charles, P., Sinha, J. K., Gu, F., Lidstone, L., and Ball, A. D., 2009. "Detecting the crankshaft torsional vibration of diesel engines for combustion related diagnosis". *Journal of sound and vibration,* ***321***(3-5), pp. 1171–1185.

[64] Amirtharajah, R., and Chandrakasan, A. P., 1998. "Self-powered signal processing using vibration-based power generation". *IEEE journal of solid-state circuits,* ***33***(5), pp. 687–695.

[65] Han, B., Vassilaras, S., Papadias, C. B., Soman, R., Kyriakides, M. A., Onoufriou, T., Nielsen, R. H., and Prasad, R., 2013. "Harvesting energy from vibrations of the underlying structure". *Journal of Vibration and Control,* ***19***(15), pp. 2255–2269.

[66] Kulkarni, V., Ben-Mrad, R., Prasad, S. E., and Nemana, S., 2013. "A shear-mode energy harvesting device based on torsional stresses". *IEEE/ASME Transactions on Mechatronics,* ***19***(3), pp. 801–807.

[67] Musgrave, P., Zhou, W., and Zuo, L., 2015. "Piezoelectric energy harvesting from torsional vibration". In ASME 2015 International Design Engineering Technical Conferences and Computers and Information in Engineering Conference, American Society of Mechanical Engineers Digital Collection.

[68] Ren, B., Or, S. W., Zhang, Y., Zhang, Q., Li, X., Jiao, J., Wang, W., Liu, D., Zhao, X., and Luo, H., 2010. "Piezoelectric energy harvesting using shear mode 0.71 pb (mg 1/3 nb 2/3) o 3–0.29 pbtio 3 single crystal cantilever". *Applied Physics Letters,* ***96***(8), p. 083502.

[69] Abdelkefi, A., Najar, F., Nayfeh, A., and Ayed, S. B., 2011. "An energy harvester using piezoelectric cantilever beams undergoing coupled bending–torsion vibrations". *Smart Materials and Structures,* ***20***(11), p. 115007.

[70] Chen, Z.-g., Hu, Y.-t., and Yang, J.-s., 2007. "Piezoelectric generator based on torsional modes for power harvesting from angular vibrations". *Applied Mathematics and Mechanics,* ***28***(6), pp. 779–784.

[71] Kim, G., 2015. "Piezoelectric energy harvesting from torsional vibration in internal combustion engines". *International Journal of Automotive Technology,* ***16***(4), pp. 645–651.

[72] Zheng, X., Zhang, Z., Zhu, Y., Mei, J., Peng, S., Li, L., and Yu, Y., 2014. "Analysis of energy harvesting performance for $d\_\{15\}$ mode piezoelectric bimorph in series connection based on timoshenko beam model". *IEEE/ASME Transactions on Mechatronics,* ***20***(2), pp. 728–739.

[73] Zhu, Y., Yu, Y., Li, L., Jiang, T., Wang, X., and Zheng, X., 2016. "Modeling and characterization of multilayered d 15 mode piezoelectric energy harvesters in series and parallel connections". *Smart Materials and Structures,* ***25***(7), p. 075027.

[74] Li, Z., Zu, J., and Yang, Z., 2018. "Introducing hinge mechanisms to one compressive-mode piezoelectric energy harvester". *Journal of Renewable and Sustainable Energy,* ***10***(3), p. 034704.

[75] Fan, K., Chang, J., Chao, F., and Pedrycz, W., 2015. "Design and development of a multipurpose piezoelectric energy harvester". *Energy Conversion and Management,* ***96***, pp. 430–439.

[76] Wu, P., Chen, Y., Li, B., and Shu, Y., 2017. "Wideband energy harvesting based on mixed connection of piezoelectric oscillators". *Smart Materials and Structures,* ***26***(9), p. 094005.

[77] Daqaq, M. F., Masana, R., Erturk, A., and Dane Quinn, D., 2014. "On the role of

nonlinearities in vibratory energy harvesting: a critical review and discussion". *Applied Mechanics Reviews,* ***66***(4).

[78] Harne, R. L., and Wang, K., 2013. "A review of the recent research on vibration energy harvesting via bistable systems". *Smart materials and structures,* ***22***(2), p. 023001.

[79] Pellegrini, S. P., Tolou, N., Schenk, M., and Herder, J. L., 2013. "Bistable vibration energy harvesters: a review". *Journal of Intelligent Material Systems and Structures,* ***24***(11), pp. 1303–1312.

[80] Cottone, F., Gammaitoni, L., Vocca, H., Ferrari, M., and Ferrari, V., 2012. "Piezoelectric buckled beams for random vibration energy harvesting". *Smart materials and structures,* ***21***(3), p. 035021.

[81] Andò, B., Baglio, S., Bulsara, A., and Marletta, V., 2014. "A bistable buckled beam based approach for vibrational energy harvesting". *Sensors and Actuators A: Physical,* ***211***, pp. 153–161.

[82] Qian, F., Zhou, S., and Zuo, L., 2020. "Approximate solutions and their stability of a broadband piezoelectric energy harvester with a tunable potential function". *Communications in Nonlinear Science and Numerical Simulation,* ***80***, p. 104984.

[83] Harne, R., Thota, M., and Wang, K., 2013. "Bistable energy harvesting enhancement with an auxiliary linear oscillator". *Smart Materials and Structures,* ***22***(12), p. 125028.

[84] Ferrari, M., Ferrari, V., Guizzetti, M., Ando, B., Baglio, S., and Trigona, C., 2010. "Improved energy harvesting from wideband vibrations by nonlinear piezoelectric converters". *Sensors and Actuators A: Physical,* ***162***(2), pp. 425–431.

[85] Stanton, S. C., McGehee, C. C., and Mann, B. P., 2010. "Nonlinear dynamics for

broadband energy harvesting: Investigation of a bistable piezoelectric inertial generator". *Physica D: Nonlinear Phenomena,* ***239***(10), pp. 640–653.

[86] Zhou, S., Cao, J., Erturk, A., and Lin, J., 2013. "Enhanced broadband piezoelectric energy harvesting using rotatable magnets". *Applied physics letters,* ***102***(17), p. 173901.

[87] Cao, J., Zhou, S., Inman, D. J., and Lin, J., 2015. "Nonlinear dynamic characteristics of variable inclination magnetically coupled piezoelectric energy harvesters". *Journal of Vibration and Acoustics,* ***137***(2).

[88] Zou, H.-X., Zhang, W.-m., Li, W.-B., Wei, K.-X., Gao, Q.-H., Peng, Z.-K., and Meng, G., 2017. "Design and experimental investigation of a magnetically coupled vibration energy harvester using two inverted piezoelectric cantilever beams for rotational motion". *Energy Conversion and Management,* ***148***, pp. 1391–1398.

[89] Arrieta, A., Delpero, T., Bergamini, A., and Ermanni, P., 2013. "Broadband vibration energy harvesting based on cantilevered piezoelectric bi-stable composites". *Applied Physics Letters,* ***102***(17), p. 173904.

[90] Li, Y., Zhou, S., Yang, Z., Guo, T., and Mei, X., 2019. "High-performance low-frequency bistable vibration energy harvesting plate with tip mass blocks". *Energy,* ***180***, pp. 737–750.

[91] Syta, A., Bowen, C., Kim, H., Rysak, A., and Litak, G., 2015. "Experimental analysis of the dynamical response of energy harvesting devices based on bistable laminated plates". *Meccanica,* ***50***(8), pp. 1961–1970.

[92] Syta, A., Bowen, C. R., Kim, H. A., Rysak, A., and Litak, G., 2016. "Responses of

bistable piezoelectric-composite energy harvester by means of recurrences". *Mechanical Systems and Signal Processing,* ***76***, pp. 823–832.

[93] Pan, D., Li, Y., and Dai, F., 2017. "The influence of lay-up design on the performance of bi-stable piezoelectric energy harvester". *Composite Structures,* ***161***, pp. 227–236.

[94] Pan, D., Jiang, W., and Dai, F., 2019. "Dynamic analysis of bi-stable hybrid symmetric laminate". *Composite Structures,* ***225***, p. 111158.

[95] Tolliver, L., Xu, T.-B., and Jiang, X., 2013. "Finite element analysis of the piezoelectric stacked-hybats transducer". *Smart materials and structures,* ***22***(3), p. 035015.

[96] Skow, E., Cunefare, K., and Erturk, A., 2014. "Power performance improvements for high pressure ripple energy harvesting". *Smart materials and structures,* ***23***(10), p. 104011.

[97] Wang, J., Shi, Z., Xiang, H., and Song, G., 2015. "Modeling on energy harvesting from a railway system using piezoelectric transducers". *Smart Materials and Structures,* ***24***(10), p. 105017.

[98] Xiong, H., and Wang, L., 2016. "Piezoelectric energy harvester for public roadway: On-site installation and evaluation". *Applied Energy,* ***174***, pp. 101–107.

[99] Chen, Y., Zhang, H., Zhang, Y., Li, C., Yang, Q., Zheng, H., and Lü, C., 2016. "Mechanical energy harvesting from road pavements under vehicular load using embedded piezoelectric elements". *Journal of Applied Mechanics,* ***83***(8).

[100] Rocha, J. G., Goncalves, L. M., Rocha, P., Silva, M. P., and Lanceros-Mendez, S., 2009. "Energy harvesting from piezoelectric materials fully integrated in footwear". *IEEE transactions on industrial electronics,* ***57***(3), pp. 813–819.

[101] Dong, W., Chen, F., Yang, M., Du, Z.-j., Tang, J., and Zhang, D., 2017. "Development of a highly efficient bridge-type mechanism based on negative stiffness". *Smart Materials and Structures,* ***26***(9), p. 095053.

[102] Wang, L., Chen, S., Zhou, W., Xu, T.-B., and Zuo, L., 2017. "Piezoelectric vibration energy harvester with two-stage force amplification". *Journal of Intelligent Material Systems and Structures,* ***28***(9), pp. 1175–1187.

[103] Bindig, R., and Helke, G., 2000. "Application of piezoceramic multilayer actuators, experiences and solutions". In 7th International Conference on New Actuators, Bremen.

[104] Mitcheson, P. D., Yeatman, E. M., Rao, G. K., Holmes, A. S., and Green, T. C., 2008. "Energy harvesting from human and machine motion for wireless electronic devices". *Proceedings of the IEEE,* ***96***(9), pp. 1457–1486.

[105] Donelan, J. M., Li, Q., Naing, V., Hoffer, J. A., Weber, D., and Kuo, A. D., 2008. "Biomechanical energy harvesting: generating electricity during walking with minimal user effort". *Science,* ***319***(5864), pp. 807–810.

[106] Giddings, V. L., Beaupre, G. S., Whalen, R. T., and Carter, D. R., 2000. "Calcaneal loading during walking and running". *Medicine & Science in Sports & Exercise,* ***32***(3), pp. 627–634.

[107] ANSYS, M. A., 2016. "Advanced analysis guide, 9". *User-programmable features SAS, seventeenth ed., IP Inc.*

[108] Simon, D., 2008. "Biogeography-based optimization". *IEEE transactions on evolutionary computation,* ***12***(6), pp. 702–713.

[109] Feenstra, J., Granstrom, J., and Sodano, H., 2008. "Energy harvesting through a

backpack employing a mechanically amplified piezoelectric stack". *Mechanical Systems and Signal Processing,* ***22***(3), pp. 721–734.

[110] Pantelopoulos, A., and Bourbakis, N. G., 2009. "A survey on wearable sensor-based systems for health monitoring and prognosis". *IEEE Transactions on Systems, Man, and Cybernetics, Part C (Applications and Reviews),* ***40***(1), pp. 1–12.

[111] Zhang, S., and Li, F., 2012. "High performance ferroelectric relaxor-pbtio3 single crystals: Status and perspective". *Journal of Applied Physics,* ***111***(3), p. 2.

[112] Zhang, Y., Lu, T.-F., and Al-Sarawi, S., 2016. "Formulation of a simple distributed-parameter model of multilayer piezoelectric actuators". *Journal of Intelligent Material Systems and Structures,* ***27***(11), pp. 1485–1491.

[113] Zhang, Y., Tu, Z., Lu, T.-F., and Al-Sarawi, S., 2017. "A simplified transfer matrix of multi-layer piezoelectric stack". *Journal of Intelligent Material Systems and Structures,* ***28***(5), pp. 595–603.

[114] Yang, Y., and Tang, L., 2009. "Equivalent circuit modeling of piezoelectric energy harvesters". *Journal of intelligent material systems and structures,* ***20***(18), pp. 2223–2235.

[115] Upadrashta, D., and Yang, Y., 2015. "Finite element modeling of nonlinear piezoelectric energy harvesters with magnetic interaction". *Smart Materials and Structures,* ***24***(4), p. 045042.

[116] Upadrashta, D., and Yang, Y., 2018. "Trident-shaped multimodal piezoelectric energy harvester". *Journal of Aerospace Engineering,* ***31***(5), p. 04018070.

[117] Pan, D., and Dai, F., 2018. "Design and analysis of a broadband vibratory energy

harvester using bi-stable piezoelectric composite laminate". *Energy conversion and management,* ***169***, pp. 149–160.

[118] Starner, T., and Paradiso, J. A., 2004. "Human generated power for mobile electronics". *Low-power electronics design,* ***45***, pp. 1–35.

[119] Xie, X., and Wang, Q., 2015. "Energy harvesting from a vehicle suspension system". *Energy,* ***86***, pp. 385–392.

[120] Yang, Z., Zu, J., Luo, J., and Peng, Y., 2017. "Modeling and parametric study of a force-amplified compressive-mode piezoelectric energy harvester". *Journal of Intelligent Material Systems and Structures,* ***28***(3), pp. 357–366.

[121] Yang, Z., and Zu, J., 2014. "High-efficiency compressive-mode energy harvester enhanced by a multi-stage force amplification mechanism". *Energy conversion and management,* ***88***, pp. 829–833.

[122] Xu, T.-B., Kang, J. H., Siochi, E. J., Zuo, L., Zhou, W., and Jiang, X., 2015. "Ultra-high power density piezoelectric energy harvesters".

[123] Wen, S., Xu, Q., and Zi, B., 2018. "Design of a new piezoelectric energy harvester based on compound two-stage force amplification frame". *IEEE Sensors Journal,* ***18***(10), pp. 3989–4000.

[124] Wu, Z., and Xu, Q., 2019. "Design and testing of a novel bidirectional energy harvester with single piezoelectric stack". *Mechanical Systems and Signal Processing,* ***122***, pp. 139–151.

[125] Jasim, A., Yesner, G., Wang, H., Safari, A., Maher, A., and Basily, B., 2018. "Laboratory testing and numerical simulation of piezoelectric energy harvester for roadway applications". *Applied Energy,* ***224***, pp. 438–447.

[126] Luo, L., Liu, D., Zhu, M., Liu, Y., and Ye, J., 2018. "Maximum energy conversion from human motion using piezoelectric flex transducer: A multi-level surrogate modeling strategy". *Journal of Intelligent Material Systems and Structures,* ***29***(15), pp. 3097–3107.

[127] Luo, L., Liu, D., Zhu, M., and Ye, J., 2017. "Metamodel-assisted design optimization of piezoelectric flex transducer for maximal bio-kinetic energy conversion". *Journal of Intelligent Material Systems and Structures,* ***28***(18), pp. 2528–2538.

[128] Turkmen, A. C., and Celik, C., 2018. "Energy harvesting with the piezoelectric material integrated shoe". *Energy,* ***150***, pp. 556–564.

[129] Harman, E., Han, K.-H., and Frykman, P., 2001. Load-speed interaction effects on the biomechanics of backpack load carriage. Tech. rep., ARMY RESEARCH INST OF ENVIRONMENTAL MEDICINE NATICK MA.

[130] Kim, G.-W., and Kim, J., 2012. "Compliant bistable mechanism for low frequency vibration energy harvester inspired by auditory hair bundle structures". *Smart Materials and Structures,* ***22***(1), p. 014005.

[131] Wang, W., He, X., Wang, X., Wang, M., and Xue, K., 2018. "A bioinspired structure modification of piezoelectric wind energy harvester based on the prototype of leaf veins". *Sensors and Actuators A: Physical,* ***279***, pp. 467–473.

[132] Wang, W., Wang, X., He, X., Wang, M., Shu, H., and Xue, K., 2019. "Comparisons of bioinspired piezoelectric wind energy harvesters with different layout of stiffeners based on leaf venation prototypes". *Sensors and Actuators A: Physical,* ***298***, p. 111570.

[133] Fu, H., Sharif-Khodaei, Z., and Aliabadi, F., 2019. "A bio-inspired host-parasite struc-

ture for broadband vibration energy harvesting from low-frequency random sources". *Applied Physics Letters,* ***114***(14), p. 143901.

[134] Zhang, Y., Jeong, C. K., Yang, T., Sun, H., Chen, L.-Q., Zhang, S., Chen, W., and Wang, Q., 2018. "Bioinspired elastic piezoelectric composites for high-performance mechanical energy harvesting". *Journal of Materials Chemistry A,* ***6***(30), pp. 14546–14552.

[135] Kim, S.-W., Koh, J.-S., Lee, J.-G., Ryu, J., Cho, M., and Cho, K.-J., 2014. "Flytrap-inspired robot using structurally integrated actuation based on bistability and a developable surface". *Bioinspiration & biomimetics,* ***9***(3), p. 036004.

[136] Zhang, Z., Chen, D., Wu, H., Bao, Y., and Chai, G., 2016. "Non-contact magnetic driving bioinspired venus flytrap robot based on bistable anti-symmetric cfrp structure". *Composite Structures,* ***135***, pp. 17–22.

[137] Kim, P., Son, D., and Seok, J., 2016. "Triple-well potential with a uniform depth: Advantageous aspects in designing a multi-stable energy harvester". *Applied Physics Letters,* ***108***(24), p. 243902.

[138] Neville, R. M., Groh, R. M., Pirrera, A., and Schenk, M., 2018. "Shape control for experimental continuation". *Physical review letters,* ***120***(25), p. 254101.

[139] Wang, W., Cao, J., Bowen, C. R., Inman, D. J., and Lin, J., 2018. "Performance enhancement of nonlinear asymmetric bistable energy harvesting from harmonic, random and human motion excitations". *Applied Physics Letters,* ***112***(21), p. 213903.

[140] He, Q., and Daqaq, M. F., 2014. "Influence of potential function asymmetries on the performance of nonlinear energy harvesters under white noise". *Journal of Sound and Vibration,* ***333***(15), pp. 3479–3489.

[141] Panyam, M., Daqaq, M. F., and Emam, S. A., 2018. "Exploiting the subharmonic parametric resonances of a buckled beam for vibratory energy harvesting". *Meccanica,* ***53***(14), pp. 3545–3564.

[142] Emam, S. A., Hobeck, J., and Inman, D. J., 2019. "Experimental investigation into the nonlinear dynamics of a bistable laminate". *Nonlinear Dynamics,* ***95***(4), pp. 3019–3039.

[143] Wang, X., and Lin, L., 2013. "Dimensionless optimization of piezoelectric vibration energy harvesters with different interface circuits". *Smart materials and structures,* ***22***(8), p. 085011.

[144] Navarro-López, E. M., and Suárez, R., 2004. "Modelling and analysis of stick-slip behaviour in a drillstring under dry friction". In Congress of the Mexican Association of Automatic Control, pp. 330–335.

[145] Khulief, Y., Al-Sulaiman, F., and Bashmal, S., 2007. "Vibration analysis of drillstrings with self-excited stick–slip oscillations". *Journal of Sound and Vibration,* ***299***(3), pp. 540–558.

[146] Lardner, T. J., and Archer, R. R., 1994. *Mechanics of solids.*

[147] Liao, Y., and Sodano, H. A., 2008. "Model of a single mode energy harvester and properties for optimal power generation". *Smart Materials and Structures,* ***17***(6), p. 065026.

[148] Wang, F., Wang, Z., Soroush, M., and Abedini, A., 2016. "Energy harvesting efficiency optimization via varying the radius of curvature of a piezoelectric thunder". *Smart Materials and Structures,* ***25***(9), p. 095044.

[149] Song, H. J., Choi, Y.-T., Wereley, N. M., and Purekar, A. S., 2010. "Energy harvesting devices using macro-fiber composite materials". *Journal of Intelligent Material Systems and Structures,* ***21***(6), pp. 647–658.

[150] TIMOSHENKO, S., 1937. Vibration problems in engineering second edition.